ulm university universität
uulm

Impulse-Radio Ultra-wideband Circuits for Communication and Radar Sensing

DISSERTATION

zur Erlangung des akademischen Grades eines

DOKTOR-INGENIEURS (Dr.-Ing.)

der Fakultät für Ingenieurwissenschaften
und Informatik der Universität Ulm

von

Dayang Lin

aus Tengzhou, China

Betreuer:	Prof. Dr.-Ing Hermann Schumacher
	Prof. Dr.-Ing Ingmar Kallfass
Amtierender Dekan:	Prof. Dr. Tina Seufert

Ulm, 19.12.2014

Acknowledgement

This thesis is a result of my scientific research in the Institute of Electron Devices and Circuits at Ulm University, Germany. It is partially supported by the German research foundation (DFG) by the means of the priority program "Ultra-Wideband Radio Technologies for Communications, Localization and Sensor Applications (UKoLoS)". In this priority program, my institute collaborated with the Institute of Microwave Techniques and the Institute of Information Technology at Ulm University.

First of all, I express my most sincere gratitude to my supervisor, Prof. Dr.-Ing. Hermann Schumacher for providing me such a great research opportunity in an excellent environment. I would like to deeply thank him for his continuous support, guidance and encouragement in every aspect throughout my time in his group. This dissertation would not have been possible without his great help.

Besides, I would like to thank Dr. Andreas Trasser for sharing his powerful experience and providing me lots of valuable discussions. I am deeply grateful to the "UWB fellow" Dr.-Ing Bernd Schleicher, who has shared his UWB knowledge with me and given great support. I would also like to express my thanks to Dr.-Ing Mario Leib for allowing me to use his UWB antenna and passive baluns. I am indebted to Michael Mirbach for fruitful discussions and performing several radar measurements. I would like to thank Thanawat Thiasiriphet, Prof. Dr.-Ing. Wolfgang Menzel and Prof. Dr.-Ing. Jürgen Lindner for their excellent collaboration throughout the project. I would like to thank my colleagues Heba Abdeen, Ahmed Elsokary, Peter Lohmiller, Andreas Strodl, Shuai Yuan, Marco Balducci, Filipe Tabarani, Sven Hettich, Giuseppe Oliveri, Xiaolei Gai, Ms. Ursula Winter, Dr. Vaclav Valenta (in office room order) for their valuable discussions and proof reading of the thesis. I am indebted to previous colleagues Dr. Gang Liu, Till Feger, Dr. Ahmet Cagri Ulusoy, Guangwen Qu, Dr. Tatyana Purtova, Dr. Michael Hosch, Dr. Sebastien Chartier, Ferdinand Sigloch, Yinmei Su, Philipp Leber, Dominik Schrade-Köhn for their support and help.

Last but not least, I would like to thank my parents, who are always encouraging and supporting me.

Contents

1 Introduction **1**

1.1 Motivation 1

1.2 Technology 2

1.3 Thesis Organisation 3

2 Fundamentals of UWB **4**

2.1 UWB Regulations 4

2.1.1 UWB Worldwide Spectral Masks 4

2.1.2 Multi-band (MB) vs. Impulse-radio (IR) 7

2.2 IR-UWB Opportunities 9

3 IR-UWB Transmitter Design **11**

3.1 Impulse Generation Methods 11

3.2 Impulse Modulation Schemes 13

3.3 Differential Impulse Generator for the FCC Mask 14

3.3.1 Quenched-oscillation Principle 14

3.3.2 Circuit Design 18

3.3.3 Measurement Results 21

3.4 Differential Tunable Impulse Generator 24

3.4.1 Circuit Implementation 25

3.4.2 Measured Results 27

3.5 Differential Impulse Generator with BPM Function 30

3.5.1 Circuit Implementation 30

3.5.2 Measured Results 32

3.6 In-body UWB Beacon Transmitter 35

3.6.1 Transmitter Topology . . . 36
3.6.2 Impulse Generation and Monoflop Circuit . . . 36
3.6.3 Differential UWB Power Amplifier . . . 38
3.6.4 Transmitter Characterization . . . 41

4 Differential IR-UWB Receiver Design 46
4.1 Basic Receiver Concepts . . . 46
4.1.1 Correlation Detection . . . 46
4.1.2 Energy Detection . . . 47
4.2 Fully Differential Low Noise Amplifier . . . 48
4.2.1 Circuit Design . . . 48
4.2.2 Measured Results . . . 52
4.3 Correlation Detection Receiver . . . 54
4.3.1 Correlator based on analog correlation . . . 54
4.3.2 Fully Monolithic Correlation Receiver . . . 57
4.3.3 Correlation Reception of Impulse Sequence with BPM . . . 63
4.4 Energy Detection Receiver . . . 64
4.4.1 Energy Detection Circuit . . . 64
4.4.2 Fully Monolithic Energy Detection Receiver . . . 66
4.4.3 System Validation: Communications . . . 68

5 IR-UWB Radar system with a Differential Frontend 71
5.1 System Concept . . . 71
5.2 UWB Radar System . . . 73
5.2.1 Radar Implementation . . . 74
5.2.2 Tracking the Movement of a Metal Plate . . . 76
5.2.3 Breath Rate Detection . . . 77
5.2.4 3D Localization . . . 77
5.2.4.1 Target Boundary Estimation . . . 79
5.2.4.2 3D Localization Experiment . . . 83

6 Monostatic Radar Frontend 86
6.1 The Logic Circuit . . . 87
6.2 The Differential LNA with Sleep Mode . . . 89
6.3 The Impulse Generator and the Buffer Stage . . . 92
6.4 System Measurement . . . 93

7 Conclusion **94**

A Circuit parameters **104**

A.1 Differential Impulse Generator for the FCC Mask 104

A.2 Differential Tunable Impulse Generator 105

A.3 Differential Impulse Generator with BPM Function 105

A.4 UWB Beacon Transmitter 106

A.5 Differential LNA 107

A.6 Multiplier-based Correlator 107

A.7 Energy Detection Circuit 108

A.8 Impulse Generator/LNA Module 109

B List of Acronyms and Symbols **110**

C Publications **113**

List of Figures

2.1 The UWB spectral masks allocated by (a) FCC in USA and (b) ECC in Europe and MIC in Japan. For the ECC and Japanese masks, only the mitigation-free bands are shown. 5

3.1 Fifth derivative of the Gaussian bell shape with σ=51 ps in (a) time and (b) frequency domain. 12

3.2 Gaussian-gated oscillation signal in (a) time and (b) frequency domain. The envelope of the impulse is a Gaussian bell shape with σ = 100 ps. . 13

3.3 Equivalent circuit of a cross-coupled LC oscillator, the cross-coupled pair is modelled as a negative impedance -R_C. 15

3.4 Transient waveform of the quenched oscillator. 16

3.5 Block diagram of the differential UWB impulse generator targeting for the FCC indoor mask. 18

3.6 Complete circuit schematic of the proposed differential impulse generator. Circuit details can be found in Appendix A.1. 19

3.7 Transistor level simulations: the collector potential of T_3 and the collector current of T_4. 19

3.8 Simulated waveforms of (a) the input clock signal with a frequency of 200 MHz and (b) the generated impulse sequence with a repetition rate equal to the input clock frequency. 21

3.9 Microphotograph of the realized impulse generator IC. Chip size is 0.3 mm^2. 21

3.10 Measured and simulated impulse waveforms. Here the waveforms are normalized for a good comparison. 22

3.11 Measured results of the 100 MHz impulse train in (a) time and (b) frequency domain. 22

3.12 Measured output UWB impulse waveforms at (a) 200 MHz and (b) 1.3 GHz input frequencies. 23

3.13 Measured energy consumption per pulse versus output impulse repetition rate. It decreases with increasing repetition rate. 23

3.14 Photograph of the front view of the complete transmitter. 24
3.15 Normalized received amplitudes in the (a) E-plane and (b) H-plane. . . 25
3.16 Block diagram of the differential tunable UWB impulse generator. . . . 25
3.17 Complete circuit schematic of the impulse generator tunable to FCC, ECC and Japanese masks. Detailed circuit parameters are presented in Appendix A.2. 26
3.18 The relationship between the current spike width and the output oscillation signal. 26
3.19 Microphotogragh of the realized impulse generator IC. This compact design has an area of 0.32 mm^2. 27
3.20 Measured impulse train in (a) time and (b) frequency domain. The output spectrum complies well with the FCC indoor mask. 28
3.21 Measured impulse train with a repetition rate of 100 MHz rate in (a) time and (b) frequency domain under the ECC mode. 28
3.22 Measured impulse train with a repetition rate of 100 MHz rate in (a) time and (b) frequency domain with targeting the Japanese mask. . . . 29
3.23 (a) Picture of the packaged circuit and (b) comparison of the packaged and on-wafer measured impulse waveforms. 30
3.24 Block diagram of the differential UWB impulse generator with BPM function. 31
3.25 Complete circuit schematic of the differential impulse generator with BPM function. Detailed circuit parameters can be found in Appendix A.3. 31
3.26 Microphotogragh of the realized impulse generator IC. This compact design has an overall area of 0.56 x 0.53 mm^2 including bond pads. . . 32
3.27 Comparison of the measured and simulated impulse waveforms with the data port shorted to ground. 33
3.28 Measured impulses with different applied data signal in time domain. The results show a perfect biphase modulation. 33
3.29 Measured impulses with different applied data signal in frequency domain. The output spectra of the 200 MHz impulse trains in both situations comply well with the FCC indoor mask. 34
3.30 (a) Measured 1.2 GHz impulse trains with different applied voltages at the data port and (b) impulse sequence of an applied modulation signal through data port. 35
3.31 (a) Package picture and (b) comparison between packaged and on-wafer measured impulse waveforms and (c) the complete transmitter. 35

3.32 Complete block diagram of the proposed differential UWB transmitter employed as an active beacon. 36
3.33 Circuit schematic of the impulse generation circuit and the monoflop. Circuit details are given in the Appendix A.4. 37
3.34 Transistor level simulation: the collector potential of T_3, I_1, I_2. 37
3.35 Complete Schematic diagram of the fully differential UWB PA. Detailed circuit parameters are presented in Appendix A.4. 38
3.36 Comparison of the measured and simulated S-parameter magnitudes. 39
3.37 The measured OP_{1dB} of the differential PA versus frequencies in the FCC allocated range. 40
3.38 Chip micro-photograph of the differential UWB transmitter. 40
3.39 Measurement results of (a) the time-domain impulse sequence with a repetition rate of 200 MHz and (b) the corresponding spectrum information. 41
3.40 (a) Picture of the antenna structure, (b) photograph of the complete UWB transmitter with the IC sealed by water-resistive glue, (c) photograph of the antenna substrate and (d) microphotograph of the transmitter IC placed chip-on-board on the antenna substrate. 42
3.41 The relative permittivity (a) and the attenuation constants (b) of the various human tissues. All of them show a linear frequency behaviour. 43
3.42 The relative permittivity (a) and the attenuation constant (b) of the tissue-mimicking liquid HSL 5800. It is a suitable replacement medium for the human skin in the test environment. 43
3.43 Measurement set-up when characterizing the UWB beacon transmitter. Both the transmitter and the receiver antenna are immersed into the liquid. 44
3.44 The received impulse waveform with the receive antenna placed with a distance of 3 cm from the transmitter. 44
3.45 The rotation details of the UWB transmitter for radiation pattern measurement. 45
3.46 Relative amplitude of the received impulse when rotating the transmitter in (a) E-plane and (b) H-plane. 45

4.1 Block diagram of a typical correlation detection receiver. 47
4.2 Block diagram of a non-coherent energy detection receiver. 48
4.3 Schematic of the proposed fully differential LNA, it is based on a cascoded emitter-coupled pair with shunt-shunt feedback. The buffer stage is employed for inter-stage matching. 49

4.4 Simulated results of (a) F_{min} and (b) r_n, without and with feedback. . . 51

4.5 Comparison of (a) $\Gamma_{S,opt}$ and (b) differential noise figures of the LNA without and with feedback. 51

4.6 Microphotograph of the differential UWB LNA. It has an extremely small area of 0.14 mm^2. 52

4.7 Comparison of the measured and simulated S-parameter magnitudes of the differential LNA. 53

4.8 Measured and simulated results of (a) the group delay and (b) the single-ended gain of the fabricated UWB LNA. 53

4.9 (a) The measured single-ended and extracted differential noise figures in comparison with the simulated ones and (b) the measured LNA gain depending on input power at 7 GHz. 54

4.10 Complete schematic of the UWB correlator with a real-time multiplier, low-pass filters and a differential buffer. Detailed circuit parameters are presented in Appendix A.6. 55

4.11 Simulation configurations for characterizing the correlation circuit with (a) sinusoidal signals as inputs and (b) UWB impulses as inputs. 56

4.12 Simulation results of (a) the conversion gain when down-conversion to a fixed IF of 100 MHz with different input power levels at template port and (b) IP_{1dB} versus frequencies. 56

4.13 Simulated output transients of (a) the Gilbert cell and (b) the correlator, at feeding two time-aligned impulse sequences with a repetition rate of 200 MHz to the input ports of the correlator. 57

4.14 (a) Simulated normalized correlation of two UWB impulses generated by the impulse generation circuit shown in Fig. 3.6 and (b) details in the vicinity of the correlation maximum. 57

4.15 Complete block digram of the monolithic correlation receiver frontend. 58

4.16 Chip micrograph of the differential monolithic correlation receiver frontend. The fully integrated frontend circuit has a small area of 0.51 mm^2. 58

4.17 Measurement set-up for characterizing the fabricated correlation receiver frontend. The UWB impulse generator shown in Fig. 3.9 was used to generate input impulses for the receiver. 59

4.18 (a) Comparison of normalized measured and simulated receiver output transients with time-alignment of received and template impulses and (b) on-wafer measured correlation in comparison with a simulated one. 59

4.19 Measured correlator output DC voltages versus input power levels. . . 60

4.20 Photograph of the receiver. 60

4.21 Measurement set-up for characterizing the correlation performance of the fabricated correlation receiver. The UWB transmitter and the receiver were placed at a distance of 20 cm. 61

4.22 Schematic of the active low-pass filter based on two operational amplifiers. In this design, R_1 = 11.3 KΩ, R_2 = 113 KΩ and C = 56 pF. . . . 61

4.23 Measured normalized cross-correlation of received impulses with template impulses. 62

4.24 Measurement result obtained on a moving metal target with a movement amplitude of 1 mm at a distance of 20 cm from the realized UWB system. 63

4.25 Measured results of (a) the data signal and (b) the demodulated signal from the receiver with the transmitter and the receiver being placed with a distance of 20 cm. 64

4.26 Block diagram of the proposed energy detection receiver. 64

4.27 Complete circuit schematic of the energy detection receiver. Detailed circuit parameters are given in Appendix A.7. 65

4.28 Simulated results of (a) the normalized time-domain output of the squaring circuit and the input UWB impulse and (b) the output power of the energy detection circuit at DC versus input power at 7 GHz. . . 65

4.29 Chip micrograph of the differential energy detection receiver IC. This design has an overall area of 0.26 mm^2. 66

4.30 Experiment set-up for characterizing the energy detection receiver IC in time domain. 66

4.31 Measured time-domain (a) input UWB impulse sequence and (b) output from the energy detection receiver IC. 67

4.32 The measured differential output DC voltages versus applied input power. The MDS of the energy detection receiver is worse than that of the correlation receiver. 67

4.33 Photo of the packaged energy detection based receiver. 68

4.34 OOK transmission experiment at 50 Mbit/s over a distance of 20 cm. (a) shows the signal at the input to the transmitter and (b) shows the detected signal at the output of the receiver. 68

4.35 The measured results of (a) the input data sequence to the transmitter and (b) the output signal of the receiver. 69

4.36 Photograph of the IR-UWB system demonstrator for FM communication. 70

5.1 Block diagram of the differential UWB radar system, the measuring target is placed in front of the radar. 72

5.2 The relationship between the cross-correlation function and the Δf signal. 73

5.3 The photograph of the compact differential UWB radar system. The ICs are placed chip-on-board on the antenna substrate for a compact design. 74

5.4 (a) The sketch and (b) the measured radiation pattern of the realized UWB antenna. 75

5.5 Front-side view of (a) the transmitter and (b) the complete receiver with RF frontend IC and the baseband circuitry. Both the impulse generator and the receiver IC are mounted on the antenna substrates and wire-bonded to external micro-strip transmission lines. 75

5.6 Photograph of the UWB radar measurement platform for tracking the movement of a metal plate. 76

5.7 Measured results of a moving metal plate in front of the UWB radar with a mean distance of 15 cm in (a) time and (b) frequency domain. . 76

5.8 Measured results in (a) time and (b) frequency domain. The metal plate is placed at a mean distance of 30 cm from the UWB radar sensor with a movement deviation of 2 mm. 77

5.9 Measured results of vital signs of a male test person standing in front of the UWB radar sensor in (a) time and (b) frequency domain. 78

5.10 Cross section of one measured ellipsoid with the transmit antenna and receive antenna placed with a distance of s. 80

5.11 (a) Photograph of the liquid container and (b) the measured cloud of estimated surface points. 81

5.12 Photograph of the measurement set-up for detecting the surface of a male torso. 82

5.13 (a) Front and (b) right-side view of estimated surface points using the proposed trilateration-based imaging algorithm for the surface measurement of the human torso dummy. 82

5.14 Photograph of the 3D localization measurement set-up with a beacon transmitter placed in a rectangular liquid container. 83

5.15 Estimated surface points using the trilateration-based imaging algorithm. A smooth 2D surface shape can be interpolated. 84

5.16 (a) Received output correlation signal from the receiver of the radar sensor and (b) the constructed wavefronts using the information of measured ToAs and the estimated surface model. 84

5.17 Measured results in the (a) top and (b) side view. The comparison of the estimated position to the manually measured coordinates shows a good agreement. 85

6.1 Block diagram of the proposed monostatic UWB radar. The merged impulse generator/LNA module is introduced to avoid the need of a complex UWB transmit/receive switch. 87
6.2 The block diagram of the external logic circuit. The inverters and the XOR gate are commercially available. 87
6.3 The timing diagram of the logic circuit. 88
6.4 Measured result of the output voltage pulse from the logic circuit. It is employed to briefly switch off the LNA 88
6.5 Complete schematic of the UWB LNA with sleep mode. Detailed circuit parameters can be found in Appendix A.8. 89
6.6 Simulated results of the bandgap reference output voltage as functions of (a) V_{ctrl} and (b) temperature. 90
6.7 Chip photo of the realized monostatic radar frontend. 90
6.8 Comparison of the measured and simulated (a) input matching and (b) output matching of the differential LNA with sleep mode. 91
6.9 The results of (a) gain and (b) noise figure of the differential LNA, with applying a constant 3 V voltage supply as the input of the bandgap reference. 91
6.10 The circuit schematic of the impulse generator and the buffer stage. The buffer stage is inserted to reduce the influence on the differential LNA in the receiving path. 92
6.11 Measurement results of the generated 80 MHz UWB impulse train in (a) time and (b) frequency domain. 92
6.12 (a) Measurement set-up and (b) the recorded waveform at the output of the LNA. 93

A.1 Full schematic of the differential impulse generator for the FCC mask. T_1, T_2,: 0.5 x 5 μm^2, T_3: 0.5 x 20 μm^2, T_4: 0.5 x 6 μm^2, T_5: 0.5 x 25 μm^2, T_6: 0.5 x 10 μm^2. 104
A.2 Full schematic of the differential tunable impulse generator. T_1, T_2,: 0.5 x 5 μm^2, T_3: 0.5 x 20 μm^2, T_4: 0.5 x 5 μm^2, T_5: 0.5 x 10 μm^2, T_6: 0.5 x 30 μm^2. 105
A.3 Full schematic of the differential impulse generator with BPM function. T_1, T_2,: 0.5 x 5 μm^2, T_3: 0.5 x 20 μm^2, T_4: 0.5 x 7 μm^2, T_5 - T_7, T_8: 0.5 x 15 μm^2, T_9 - T_{11}: 0.5 x 5 μm^2. 105
A.4 (a) Full schematic of the impulse generation and monoflop circuit. T_1, T_2,: 0.5 x 5 μm^2, T_3: 0.5 x 30 μm^2, T_4: 0.5 x 5 μm^2, T_5,: 0.5 x 10 μm^2, T_6: 0.5 x 20 μm^2, T_7, T_8: 0.5 x 5 μm^2, T_9, T_{10}: 0.5 x 30 x 2 μm^2, non-SIC and (b) the differential UWB power amplifier. T_1 - T_4: 0.5 x 30 μm^2, T_5, T_6: 0.5 x 30 μm^2, T_7, T_8: 0.5 x 5 μm^2.. 106

A.5 Full schematic of the differential UWB LNA. T_1 - T_4: 0.5 x 25 μm^2, T_5, T_6: 0.5 x 6 μm^2, T_7, T_8: 0.5 x 5 μm^2. 107

A.6 Full schematic of the correlator circuit. T_1 - T_8: 0.5 x 10 μm^2, T_9, T_{10}: 0.5 x 5 μm^2. 107

A.7 Full schematic of the energy detection circuit. T_1, T_2,: 0.5 x 6 μm^2, T_3 - T_{10}: 0.5 x 10 μm^2, T_{11}, T_{12}: 0.5 x 5 μm^2. 108

A.8 (a) Full schematic of the differential LNA with sleep mode. T_1 - T_4: 0.5 x 30 μm^2, T_5, T_6: 0.5 x 6 μm^2, T_7, T_{13}: 0.5 x 5 μm^2, T_{14}: 0.5 x 25 x 2 μm^2 non-SIC, T_{15}: 0.5 x 30 x 2 μm^2 non-SIC, and (b) the impulse generator together with a buffer stage. T_1, T_2,: 0.5 x 5 μm^2, T_3: 0.5 x 20 μm^2, T_4: 0.5 x 6 μm^2, T_5: 0.5 x 20 μm^2, T_6: 0.5 x 10 μm^2. T_7, T_8: 0.5 x 10 μm^2, T_9: 0.5 x 5 μm^2, T_{10}, T_{11}: 0.5 x 15 μm^2 109

List of Tables

2.1 Maximum allowed EIRP densities of the FCC UWB mask. 6

2.2 Maximum allowed EIRP densities of (left) the European ECC spectral mask and (right) the Japanese UWB mask. 6

2.3 Detailed band group information of the MB-OFDM UWB system. The complete FCC allocated band is divided into 14 sub-bands. 7

3.1 Performance summary of the tunable impulse generator. 29

3.2 Performances of impulse generator with different applied voltages at the data port. 34

Chapter 1

Introduction

1.1 Motivation

Ultra-wideband (UWB) technology has attracted considerable attention over the past several decades because of its potential to provide high-speed communication, sensing and precise localization. The term "UWB" was officially adopted in 1989 by the U.S. Department of Defense. However, UWB radio has a long history. The original concept of UWB appeared in the days of Hertz and Marconi. In the late 1800s, Marconi designed spark gap radio transmitters to send Morse-code pulse streams having a wide bandwidth. At that time, it was not necessary to consider the issues of band limitation and spectral efficiency because radio frequency regulations did not exist. Employing short pulses with a large bandwidth was the easiest way to transmit information. The development of modern wireless UWB dates back to the late 1960s with the pioneering contribution of Harmuth [1]. From the 1960s to the 1990s, modern UWB technology was primarily restricted to military purposes and focused on impulse-radar applications for accurate localization and clandestine communications [2].

Recently, UWB technology has received renewed interest in high-speed communication and precise radar applications since the Federal Communications Commission (FCC) issued its First Report and Order to allocate unlicensed UWB applications in 2002 [3]. The regulatory mask allocated a large frequency range (3.1 - 10.6 GHz) with low maximum power spectral densities (PSD) below -41.3 dBm/MHz. Although there are already several established-narrow band services within the FCC allocated band, the extremely low radiated PSD ensures that the interference potential of UWB to these existing narrowband radio systems is negligible. This property turns UWB into a new use of the radio spectrum resources and significantly increases the spectrum efficiency. On the downside, low PSD and simultaneously strong interferers do present challenges in implementing UWB receiver systems.

The UWB regulation defined by the FCC potentially opens new doors for many wireless applications. E.g., the extremely large bandwidth makes UWB a perfect candi-

date for short range high speed data transmission. Meanwhile, this wide transmission bandwidth offers excellent robustness to multipath fading [4]. Furthermore, the UWB technology is considered as one of the most interesting real-time localization and sensing techniques due to its high resolution capability. Other interesting fields for UWB technology are medical applications. The low PSD ensure that the UWB signal is harmless to the human body and non-interfering with other medical equipments.

In recent years, other administrations, e.g., in Europe, Japan and China, have issued their own and more restrictive frequency allocations, which however are within the FCC mask.

This thesis explores the applications of UWB technology in communication and medical sensing. UWB frontend ICs shall be designed to realize these functions. Regarding the circuit topology, a fully differential configuration will be considered in this thesis, because fully differential UWB antennas avoid the notorious problem of feed line radiation [5]. The differential frontend circuits not only offer an excellent match to symmetric antennas, but also ease packaging. Here differential UWB transmitters will be investigated to generate short time-domain impulses and make optimum use of the spectral mask. A novel and highly efficient impulse generator concept will be considered to achieve low power consumption, which makes the UWB transmitters suitable for medical implants. Furthermore, a tunable UWB transmitter shall be designed to observe the limitations of different regulatory spectrum masks. At the receiver side, two fully differential receiver structures will be implemented for high-speed communications and precise sensing. Low power consumption could be achieved through the elimination of active UWB baluns. In terms of system integration, a differential bistatic UWB radar sensor will be constructed. It can be used for contact-less vital sign, e.g. human respiration, detection. Moreover, this differential UWB radar can be employed for medical imaging and subsurface localization, e.g., the localization of interventional devices, such as catheters placed inside the human body.

1.2 Technology

Since this work mainly focuses on the implementation of UWB front-end ICs, it is worth to briefly mention the manufacturing technology. All active circuits are realized in Telefunken Semiconductors GmbH SiGe2RF 0.8 μm HBT technology [6]. Two kinds of npn transistors, with high f_T (f_T = 80 GHz, BV_{CEO} = 2.4 V) and with high breakdown voltage (f_T = 50 GHz, BV_{CEO} = 4.3 V) are simultaneously available. The technology has 0.8 μm feature size and a minimum effective emitter size for vertical HBT transistors of 0.5 x 1.1 μm^2. The process incorporates three metallization layers, four different types of resistors and dielectric MIM capacitors. All the devices were fabricated on a low resistivity 20Ω cm substrate. Since the FCC allocated UWB range is from 3.1-10.6 GHz, this process offers more than adequate performance for

UWB applications. Meanwhile, the process cost is very reasonable, even for a small production volume.

1.3 Thesis Organisation

This work concentrates on the design, implementation and characterization of IR-UWB transmitter and receiver ICs. The transmitter circuits based on a quenched-oscillator approach generate sub-nanosecond impulses with a spectrum well fitting the regulatory spectral mask. Moreover, the quenched-oscillator concept introduces tunability and biphase modulation capabilities to the UWB waveforms. In terms of receiver implementations, two different topologies, i.e., correlation detection and energy detection, are realized.

The thesis is organized as follows: Chapter 2 provides a short overview of background information on UWB technology, specially detailing different UWB spectral regulations, two UWB approaches and various UWB applications.

In chapter 3, the discussion of UWB transmitter design is given. This chapter starts with a brief overview of the UWB impulse generation methods and modulation schemes, followed by the circuit implementations and measured results. Impulse generator ICs following the quenched oscillation method are designed and characterized.

Two different types of fully differential receivers are described in chapter 4. The correlation receiver includes a differential low noise amplifier (LNA), a UWB correlator and a template impulse generator. While, the energy detection receiver comprises a differential LNA and an energy detection circuit. System validations for both systems are shown.

Chapter 5 presents a differential bistatic UWB radar sensor utilizing the correlation receiver. It can be used for the metal measurement tracking and human breath rate detection. Based on a trilateration-based algorithm, the abilities of the radar sensor for medical imaging and subsurface localization are demonstrated.

Chapter 6 proposes a monostatic radar system. Frontend IC for monostatic radar is implemented, fabricated and characterized.

Finally, the conclusion is summarized in chapter 7.

Chapter 2

Fundamentals of UWB

This chapter presents the fundamental theory of UWB technology. It focuses on describing different UWB spectral regulations and approaches. Specifically, the impulse-radio approach is compared with the multi-band method. Additionally, a wide range of UWB applications, both in communication and radar sensors, are analysed.

2.1 UWB Regulations

The emission of UWB signal is intended to fit into regulatory spectrum masks which define the spectral and power limits. In general, frequency ranges are preferred where no interference mitigation is mandated. However, the frequency bands are different from country to country, e.g., the original FCC mask for the USA is from 3.1-10.6 GHz; the mask defined by ECC (Electronic Communications Committee) is from 6-8.5 GHz in Europe; the Japanese mask is 7.25-10.25 GHz. This section describes several UWB regulatory masks in different countries.

2.1.1 UWB Worldwide Spectral Masks

The most influential milestone in modern UWB development is the FCC regulation set in 2002 in the USA [3]. It is the first commercial regulation allowing the emission of UWB signals and classifies UWB operating restrictions into three categories:

1. Communication and measurement systems.

2. Imaging systems, such as medical imaging, ground penetrating radar and through-wall imaging.

3. Vehicular radar systems.

According to the FCC's definition, any signal having an absolute 10-dB bandwidth larger than 500 MHz or a fractional bandwidth larger than 0.2 can be called a UWB signal. The fractional bandwidth B_f is defined as

$$B_f = 2(f_H - f_L)/(f_H + f_L) \tag{2.1}$$

where f_H and f_L are the upper and lower frequency boundaries measured at -10 dB below the peak emission points, respectively. The FCC defined a frequency mask to regulate the unlicensed transmission of UWB signals. The frequency band of 3.1-10.6 GHz is approved for indoor and outdoor UWB operations [3]. The maximum allowed effective isotropic radiated power (EIRP) is limited to -41.3 dBm/MHz, and the maximum peak PSD is defined as 0 dBm/50 MHz. The extremely low PSD renders UWB signal as noise for other radio communication systems. Therefore UWB is an overlay technology, coexisting with the previous spectrum users with negligible interference. The frequency and power constraints are depicted in Fig. 2.1. Stricter

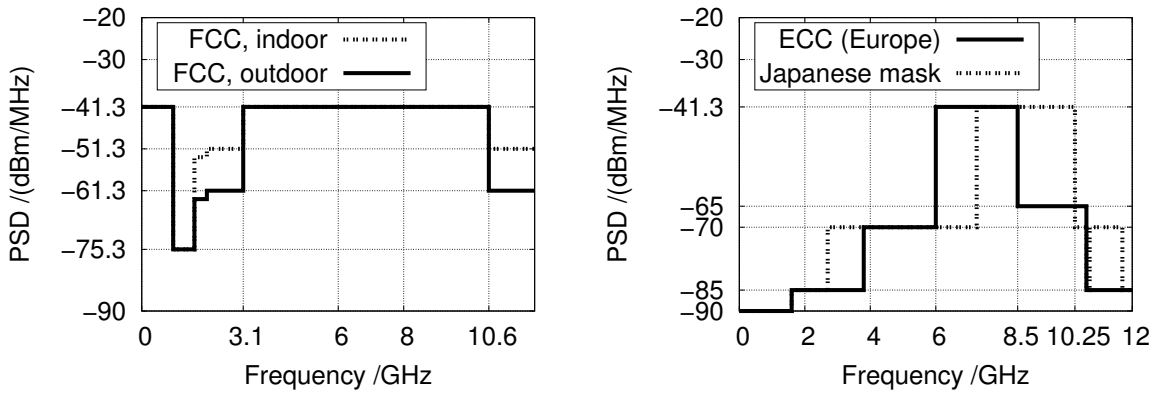

Fig. 2.1: The UWB spectral masks allocated by (a) FCC in USA and (b) ECC in Europe and MIC in Japan. For the ECC and Japanese masks, only the mitigation-free bands are shown.

PSD limits have been placed around 2 GHz to ensure a peaceful coexistence of UWB with other critical applications, such as the Global Positioning System (GPS) service operating at 1.6 GHz and Global System for Mobile Communications (GSM) devices at 1.9 GHz. Furthermore, the restrictions on outdoor devices are more stringent than that on indoor devices. Tab. 2.1 illustrates detailed values of the FCC allocated UWB masks for indoor and outdoor applications.

In Europe, the UWB standardization defined by ECC was released later than the FCC regulation in the USA. Different from the FCC's definition, ECC defined that the minimum bandwidth for UWB signal is 50 MHz. In 2007, the ECC allocated the frequency band of 6-8.5 GHz with a maximum mean EIRP spectral density of -41.3 dBm/MHz without the requirement for additional mitigation [7]. The frequency band from 3.1-4.8 GHz is allowed only with mitigation techniques, such as low duty

Frequency range GHz	Maximum EIRP dBm/MHz Indoor applications	Maximum EIRP dBm/MHz outdoor applications
< 0.96	-41.3	-41.3
0.96 - 1.61	-75.3	-75.3
1.61 - 1.99	-53.3	-63.3
1.99 - 3.1	-51.3	-61.3
3.1 - 10.6	-41.3	-41.3
> 10.6	-51.3	-61.3

Tab. 2.1: Maximum allowed EIRP densities of the FCC UWB mask.

cycle (LDC) and detect and avoid (DAA). The spectral mask including the mitigation-free band can be seen in Fig. 2.1(b).

The UWB regulation in Japan is similar to the ECC mask. In 2006, the Ministry of Internal Affairs and Communications (MIC) approved the Japanese UWB spectral mask for indoor applications [8]. It allows the use of the frequency band from 3.4-4.8 GHz using DAA and the band from 7.25-10.25 GHz without mitigation. The mean EIRP spectral density is limited to -41.3 dBm/MHz in both bands. Fig. 2.1(b) shows the mitigation-free UWB band and emission power constraints. The detailed values of the ECC and Japanese UWB masks are given in Tab. 2.2.

Frequency range GHz	Maximum EIRP dBm/MHz
< 1.6	-90
1.6 - 3.8	-85
3.8 - 4.2	-70
4.2 - 4.8	-70 (-41.3 *)
4.8 - 6.0	-70
6.0 - 8.5	-41.3
8.5 - 10.6	-65
> 10.6	-85

Frequency range GHz	Maximum EIRP dBm/MHz
< 1.6	-90
1.6 - 2.7	-85
2.7 - 3.4	-70
3.4 - 4.8	-70 (-41.3 *)
4.8 - 7.25	-70
7.25 - 10.25	-41.3
10.25 - 10.6	-70
10.6 - 10.7	-85
10.7 - 11.7	-70
11.7 - 12.75	-85
> 12.75	-70

* For devices using mitigation techniques.

Tab. 2.2: Maximum allowed EIRP densities of (left) the European ECC spectral mask and (right) the Japanese UWB mask.

As can be seen, the frequency allocations of the ECC and Japanese masks are within the FCC band. Therefore, targeting the FCC mask is a good choice for general UWB components, such as low-noise amplifiers, multipliers and squaring circuits. However, the impulse generations at the transmitter side need to observe the limitations of different regulatory spectrum masks.

2.1.2 Multi-band (MB) vs. Impulse-radio (IR)

In order to exploit UWB opportunities in compliance with the spectral and power requirements defined by the regulatory UWB masks, two operating approaches have been widely investigated: impulse-radio UWB (IR-UWB) and multi-band UWB, for example, multi-band orthogonal frequency division multiplexing UWB (MB-OFDM UWB).

MB-OFDM UWB approach

The MB-OFDM Alliance (MBOA) standard and the ECMA-368 standard promoted by the WiMedia Allianc specified the MB-OFDM UWB approach based on the FCC spectral mask [9,10]. An MB-OFDM UWB system divides the complete FCC allocated band (3.1-10.6 GHz) into fourteen sub-bands with a bandwidth of 528 MHz, complying with the FCC's definition of UWB transmission. This approach avoids potential interference with existing narrowband communication systems, such as WLAN systems. An OFDM modulation scheme is applied on each band to transmit data with communication rate up to 480 Mb/s. The band scheme of the MB-OFDM UWB system can be seen in Tab. 2.3. The complete UWB spectrum is divided into five band groups (BGs), where four BGs have three sub-bands each and one BG has two sub-bands. Each sub-band has 128 sub-channels with a bandwidth of 4.125 MHz. A time-frequency code (TFC) is utilized to interleave the information bits over each BG.

Band group	BG 1			BG 2			BG 3
Band No.	1	2	3	4	5	6	7
Lower Freq. (MHz)	3168	3696	4224	4752	5280	5808	6336
Upper Freq. (MHz)	3696	4224	4752	5280	5808	6336	6864
Band group	BG 3		BG 4			BG 5	
Band No.	8	9	10	11	12	13	14
Lower Freq. (MHz)	6864	7392	7920	8448	8976	9504	10032
Upper Freq. (MHz)	7392	7920	8448	8976	9504	10032	10560

Tab. 2.3: Detailed band group information of the MB-OFDM UWB system. The complete FCC allocated band is divided into 14 sub-bands.

According to ECMA-368, MB-OFDM UWB is considered for short range and high speed communications. Various circuit implementations have been reported so far, for example, [11] describes a direct-conversion UWB CMOS transceiver operating on bands 1-3 by employing three resonant circuits and three phase-locked loops. A fully integrated RF transceiver and digital PHY on a single chip with a physical layer data rate up to 480 Mb/s are presented in [12]. Both of the aforementioned MB-OFDM UWB systems operate on the BG 1, which introduces good coexistence with other radio service, such as IEEE 802.11a. However, an MB-OFDM UWB system always requires significant implementation complexity resulting in high power consumption.

IR-UWB approach

The IR-UWB method employs the original carrier-less concept of UWB. It works by transmitting sub-nanosecond time-domain impulses instead of continuous waves. The spectrum of the impulses occupies several GHz bandwidth which is intended to comply with the allocated spectrum mask. Compared to the MB-OFDM UWB scheme, IR-UWB presents great advantages in terms of circuit simplicity. The carrier-less nature allows a low-complexity transceiver topology. The property of impulse transmission can enable a low duty cycle operation, i.e., the energy of the radio signals is only present in a short time window (T_{on}) and no energy is present during the other time of a period (T_{off}). The low duty cycle potentially introduces a low power consumption for the IR-UWB system, because many circuit blocks of the IR-UWB system can be switched off during T_{off}. Furthermore, the short impulse duration enables a high transmission data rate in communications. Depending on the impulse repetition rate, a high communication speed up to several hundred Mbit/s could be potentially achieved. In terms of radar sensor applications, the impulse nature allows an excellent range resolution [13]. Moreover, IR-UWB approach introduces an extremely higher multi-path resolution compared to the conventional narrowband communication systems [4].

Any impulse waveform with a spectrum fitting the spectral masks can be used for IR-UWB transmission. This introduces a large design freedom at the transmitter side. However, utilizing the whole bandwidth still requires great hardware implementation challenges. Especially, the UWB spectral masks are different from country to country. A pulse source adaptable to all these bands is advantageous. In terms of impulse modulation schemes, on-off keying (OOK), pulse position modulation (PPM) and biphase modulation (BPM) formats are widely employed. Chapter 3 presents these different schemes in detail.

At the receiving side, IR-UWB receivers can take the form of simple energy detection for OOK communication without requiring precise synchronization, or correlation reception comparing the received waveforms with template impulses. The correlation receivers are more robust to interference, but at the cost of requiring accurate timing synchronization. However, this synchronization problem becomes easier in radar and sensing applications, because transmitter and receiver are always co-located and tightly synchronized. So, the form of correlation detection is suitable for precise radar applications. Detailed discussion on the two different receiver structures can be found in chapter 4. It is important to point out that the large instantaneous bandwidth accounts for significant design challenges of the receiver frontend ICs.

This thesis focuses on the implementations of impulse generators and different receiver structures based on the IR-UWB approach and exploits system designs for high-speed communication and precise sensing applications. Therefore, the scope of the following sections is narrowed to the IR-UWB approach.

2.2 IR-UWB Opportunities

The short time-domain impulses makes IR-UWB extremely attractive for a wide range of applications, such as low-distance high-speed communications, accurate localizations and radar sensing applications. In the section, different IR-UWB applications are reviewed and discussed.

Communications

IR-UWB communications are considered for a number of applications. One example employing IR-UWB systems for high-speed inter-chip communications based on inductive coupling is described in [14]. The proposed design employs Gaussian monocycle impulses with an OOK modulation scheme to transmit information. A UWB LNA is placed in the receiver to amplify the received impulses. Post layout simulations indicate that the simple IR-UWB transmitter operates up to a 5 Gbit/s data rate and draws a low power consumption of 9 mW. However, the communication distance is limited to few tens of millimeters. Another example shown in [15] proposes the IR-UWB technology for wireless personal area network (WPAN) applications. The presented IR-UWB transmitter generates pulse position modulated pulses, and the receiver is based on correlation reception. The implemented CMOS transceiver operates in the FCC frequency band and achieves a communication speed up to 200 Mbps/s. Furthermore, the low emitted power level makes the IR-UWB approach also an interesting candidate for medical applications because it does not cause harm to patients. [16] presents an IR-UWB communications system for medical implants. It utilizes the ultra-short UWB impulses to transmit capsule endoscope fast data. Another popular communication application of the IR-UWB technology is in wireless sensor networks (WSN) due to its nature of low power consumption and simple transceiver architectures [17–19].

Localization

The IR-UWB technology enables very accurate localization applications due to its very wide bandwidth. Popular methods include time-of-arrival (ToA) estimation and the time-difference-of-arrival (TDoA) approach. [20] proposes a radio-frequency identification (RFID) tag with precise hyperbolic localization based on IR-UWB. The transmit-only tag generates UWB pulses with a duration of 1.5 ns, which are captured by energy detection receivers. The realized system is based on ToA estimation and achieves a positioning accuracy of 10 cm with a potential reading range of 100 meters. Another IR-UWB system shown in [21] is implemented for positioning both static and dynamic targets in an indoor environment. Picosecond UWB pulses are generated by discrete components in this design, while, the receiver structure combines the correlation-based and the energy-detection based UWB receiver topologies. Using the TDoA approach, the realized system achieves a 3D accuracy in the millimeter range. More examples of IR-UWB localizations can be found in [22–24].

Radar and sensing

The nature of impulse transmission makes IR-UWB extremely suitable for radar and sensing applications. Popular IR-UWB sensor applications include intra-vehicle sensing [25] and monitoring of highways and various civil infrastructures [26]. In terms of applications in medical environments, IR-UWB technology can be used for vital signs monitoring and medical imaging. E.g., [27] has realized a single-ended UWB radar sensor for breath rate detection. Utilizing subnanosecond impulses, the system can measure the breath rate contact-free and achieve an accuracy in the millimeter range. Another example of medical application can be seen in [28], which proposes a 3D UWB tomographic algorithm and achieves brain hemorrhagic stroke detection.

Chapter 3

IR-UWB Transmitter Design

This chapter presents UWB impulse generators based on a quenched-oscillation concept. After providing a technical overview of various impulse generation approaches and modulation schemes, the design of a differential impulse generator targeting the FCC indoor mask is explained. Through slight modifications of this circuit, two more impulse generators are realized: one achieves a biphase modulation function and the other one provides the tunability to the ECC, FCC and Japanese spectral masks. At last, a UWB active beacon transmitter with high output voltage swing is presented.

3.1 Impulse Generation Methods

The core challenge in IR-UWB systems is to generate short time-domain impulses, making efficient use of the regulatory spectral masks. A variety of advantageous impulse shapes have been discussed [29–37]. Waveforms based on derivatives of the Gaussian bell shape are frequently used. The time domain representation of the general Gaussian bell shape can be written as

$$f(t) = \frac{A}{\sqrt{2\pi}\sigma}\exp\left(-\frac{t^2}{2\sigma^2}\right) \tag{3.1}$$

where A corresponds to the amplitude of the signal and σ is the standard deviation which defines the width of the Gaussian bell shape. According to [38], the fifth derivative of a Gaussian bell shape with σ=51 ps can fit the FCC indoor mask well. The fifth derivative of a Gaussian bell shape can be calculated as

$$f^{(5)}(t) = \frac{A}{\sqrt{2\pi}\sigma^{11}}(15t\sigma^4 - 10t^3\sigma^2 + t^5)\exp\left(-\frac{t^2}{2\sigma^2}\right) \tag{3.2}$$

Fig. 3.1 (a) plots the time-domain waveform of the fifth Gaussian derivative with σ=51 ps. The corresponding normalized spectral envelope can be seen in Fig. 3.1 (b).

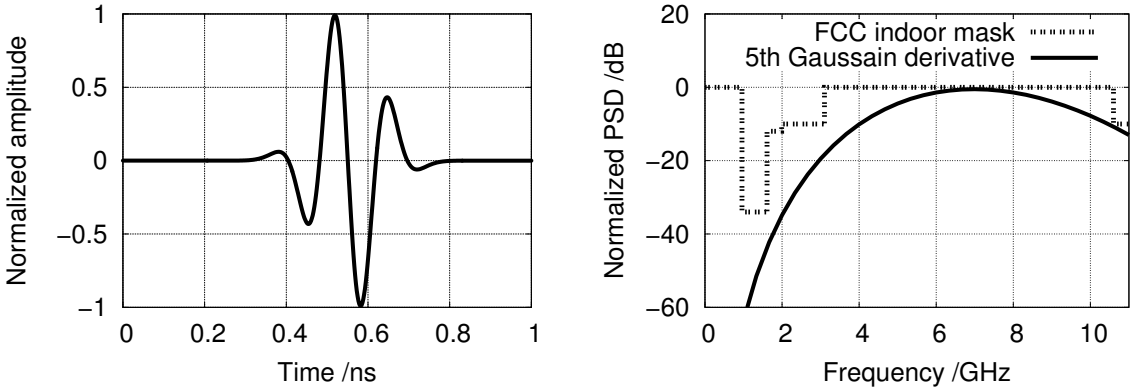

Fig. 3.1: Fifth derivative of the Gaussian bell shape with σ=51 ps in (a) time and (b) frequency domain.

It shows an excellent compliance with the FCC indoor mask. A number of circuit implementations for generating this waveform have been reported, e.g., [29] employs a damped relaxation oscillation, [30] uses piecewise approximation of the mask-conforming waveform based on four digital delay cells, [31] adopts an FIR pulse generator for pulse shaping.

An alternative way is to employ a Gaussian bell shape as an envelope of a sinusoidal signal. The corresponding impulse waveform can be expressed as

$$g(t) = \frac{A}{\sqrt{2\pi}\sigma}\exp\left(-\frac{t^2}{2\sigma^2}\right)\sin(2\pi f_0 t) \tag{3.3}$$

where A is the amplitude, σ is the standard deviation, determining the impulse width and f_0 corresponds to the oscillation frequency. The two parameters σ and f_0 can be adjusted to fit the regional spectral masks. By setting σ = 100 ps and f_0 = 6 GHz, the impulse has a spectrum fitting the FCC indoor mask. The time-domain waveform of this impulse signal is illustrated in Fig. 3.2 (a). As can be seen, the impulse waveform is similar to the fifth Gaussian derivative with σ=51 ps. The spectrum information is depicted in Fig. 3.2 (b), it has a good compliance with the FCC indoor mask. In terms of circuit implementation, this impulse waveform can be easily generated by rapidly turning an LC oscillator on and off [32–34]. This quenched-oscillation technique is favored because it allows for great circuit simplicity and low power consumption.

Another attractive impulse generation technique is the up-conversion of base-band waveforms to the allocated UWB frequency band by mixing with a local oscillator [35, 36]. This method offers precise control over the spectrum of the generated impulses, however, it suffers from a high power consumption. Another example, as described in [37], uses a pulse generation method based on a distributed waveform generator which enables low power consumption and reconfigurable spectra bandwidth.

This thesis follows the quenched-oscillation concept. The developed low-power and

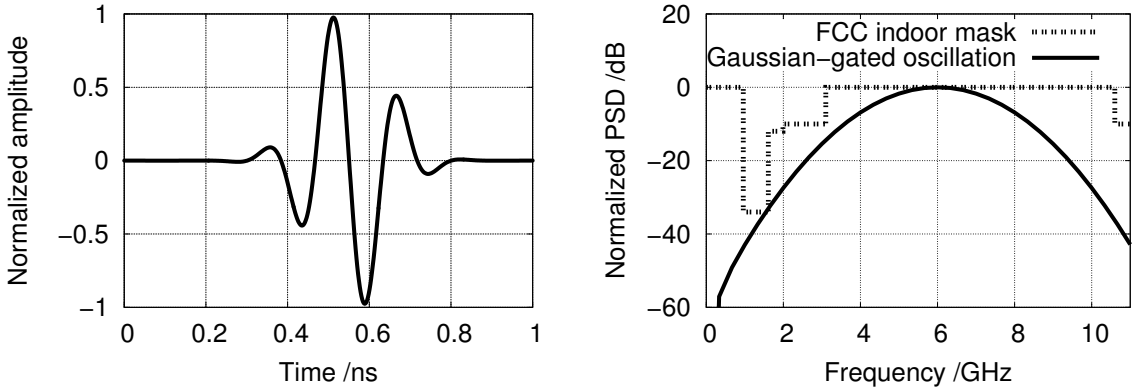

(a) (b)

Fig. 3.2: Gaussian-gated oscillation signal in (a) time and (b) frequency domain. The envelope of the impulse is a Gaussian bell shape with σ = 100 ps.

low-complexity impulse generators use current spikes generated on-chip to briefly turn on a cross-coupled LC oscillator [39]. Tunability and biphase modulation are achieved through the inherent convenience of the LC oscillator [40, 41]. Due to a novel current spike generation circuit, low power consumption and high speed can be simultaneously achieved. The designed impulse generators in this thesis have a maximum repetition rate well into the GHz range.

3.2 Impulse Modulation Schemes

There have been numerous impulse-based modulation schemes investigated in the literature so far, such as OOK, PPM, BPM, frequency modulation (FM) and pulse amplitude modulation (PAM). Among them, OOK, BPM and FM schemes are frequently employed.

OOK

OOK is a simple modulation technique where the information of the data bit is encoded by the presence or absence of an impulse. The mathematical representation of an OOK modulated UWB impulse sequence can be written as

$$s_{OOK}(t) = \sum_{k=-\infty}^{\infty} d_k f(t - kT_p), d_k = 0, 1 \tag{3.4}$$

where d_k is the data bit, f(t) is the impulse shape function and described in Eq. 3.3 and T_p is the frame period. The physical implementation of the OOK scheme is simple. Moreover, this scheme allows the transmitter to be powered off while transmitting a bit 0, significantly reducing power consumption [42].

BPM

The BPM scheme transmits data by changing the polarity of the UWB impulse. The representation of an impulse sequence under BPM is similar to that with OOK modulation, it can be expressed as

$$s_{BPM}(t) = \sum_{k=-\infty}^{\infty} d_k f(t - kT_p), d_k = -1, 1 \tag{3.5}$$

BPM constitutes antipodal signalling and has the greatest distance between symbols compared to the other schemes, thus it performs best in terms of BER in additive white Gaussian noise (AWGN) environments [43]. On the downside, this scheme causes complexity in the transmitter implementation [42].

FM

This modulation scheme employs a frequency-modulated clock signal to control the repetition rate of the generated UWB impulses. The transmitted impulse train has a position-varying property, which is determined by the information signal. So, the FM-UWB scheme is a simple solution and suitable for low data rate communications.

3.3 Differential Impulse Generator for the FCC Mask

As previously explained, the quenched-oscillation concept is appropriate for UWB impulse generation. In the following, a UWB impulse generator following this approach is presented.

3.3.1 Quenched-oscillation Principle

The quenched-oscillation concept can be illustrated by analysing the start-up and turn-off operations of a cross-coupled LC oscillator. Fig. 3.3 shows a simplified equivalent circuit of the oscillator. The two identical inductors L, a capacitor C and a parallel resistor R_P form the resonator core. R_L is the load resistor, while -R_C corresponds to the non-linear negative impedance generated by the cross-coupled pair.

For the sake of simplicity, we assume that the transfer function of -R_C can be expressed by a third-order linear function with the even-order products cancelled [44]. The relationship between the current i_S through -R_C and v_{out} can be written as

$$i_S = -g_m v_{out} + a v_{out}^3 \tag{3.6}$$

where g_m is the small-signal equivalent transconductance and a is the third-order coefficient. From Fig. 3.3, according to Kirchhoff's current law, the following current equation can be derived

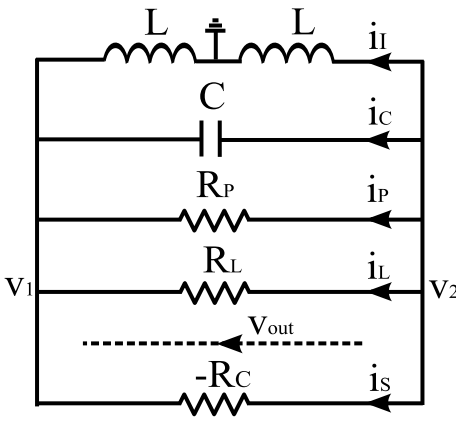

Fig. 3.3: Equivalent circuit of a cross-coupled LC oscillator, the cross-coupled pair is modelled as a negative impedance -R_C.

$$i_I + i_C + i_P + i_L + i_S = 0 \tag{3.7}$$

By differentiating Eq. 3.7 with respect to time and by knowing

$$di_I/dt = v_{out}/2L \tag{3.8}$$
$$di_C/dt = C \cdot d^2v_{out}/dt \tag{3.9}$$
$$di_P/dt = 1/R_P \cdot dv_{out}/dt \tag{3.10}$$
$$di_L/dt = 1/R_L \cdot dv_{out}/dt \tag{3.11}$$
$$di_S/dt = -g_m \cdot dv_{out}/dt + 3av_{out}^2 \cdot dv_{out}/dt, \tag{3.12}$$

the differential equation of the output voltage v_{out} will be obtained

$$C\frac{d^2v_{out}}{dt^2} + (3av_{out}^2 - g_m + \frac{1}{R_L} + \frac{1}{R_P})\frac{dv_{out}}{dt} + \frac{v_{out}}{2L} = 0 \tag{3.13}$$

Here we define $\omega_0 = 1/\sqrt{2LC}$ and $G_T = 1/R_L + 1/R_P$. Eq. 3.13 can be normalized as

$$\frac{d^2v_{out}}{dt^2} + \frac{1}{C\omega_0^2}(3av_{out}^2 + G_T - g_m)\frac{dv_{out}}{dt} + \omega_0^2 v_{out} = 0 \tag{3.14}$$

According to [44] and [45], Eq. 3.14 can be solved analytically. The complete solution of v_{out} can be expressed as

$$v_{out} = \frac{v_p}{\sqrt{1 + [(\frac{v_p}{v_{out}(0)})^2 - 1] \cdot e^{-(\frac{g_m}{G_T} - 1)\omega_0 t/Q_P}}} cos(\omega_0 t + \phi_0) \tag{3.15}$$
$$= A_1(t)cos(\omega_0 t + \phi_0) \tag{3.16}$$

with

$$v_p = \sqrt{\frac{4(g_m - G_T)}{3a}} \tag{3.17}$$

$$Q_p = \frac{1}{G_T} \cdot \sqrt{\frac{C}{2L}} \tag{3.18}$$

where v_p corresponds to the steady-state peak voltage, Q_P is the quality factor of the resonator core, $v_{out}(0)$ is the initial voltage condition and can originate from the thermal noise, ϕ_0 is the start-up phase depending on the initial conditions which are defined as the moment the LC oscillator is turned on. Eq. 3.15 describes the output voltage swing versus time immediately after the oscillator is turned on. It shows that the envelope of the oscillation is time-dependent. The waveform immediately after the oscillator is turned on can be seen in Fig. 3.4.

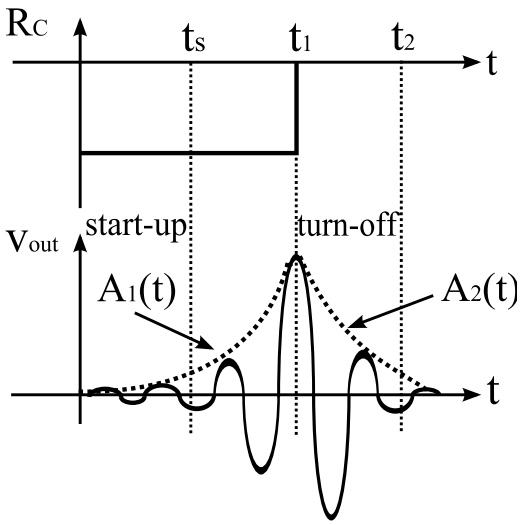

Fig. 3.4: Transient waveform of the quenched oscillator.

Start-up time

We define the start-up time t_s as the time needed for the envelope signal A(t) of the oscillation to reach 10 percent of v_p. From Eq. 3.15, t_s can be calculated as

$$t_s = \frac{\{ln[(\frac{v_p}{v_{out}(0)})^2 - 1] - 4.6\} \cdot Q_P}{(\frac{g_m}{G_T} - 1)\omega_0} \tag{3.19}$$

Clearly, t_s is inversely proportional to the initial voltage condition $v_{out}(0)$. Additionally, the open loop gain g_m/G_T and the quality factor Q_P of the resonator also play an important role on the start-up performance. In a conventional LC oscillator, $v_{out}(0)$ is primarily determined by a momentary thermal noise voltage with an amplitude in the μV range, which causes a relatively slow start-up. However, a fast start-up is necessary for a low-power UWB transmitter because it can shorten the turn-on time

for a given output impulse envelope. Based on Eq. 3.19, this can be achieved by either a high open loop gain or setting $v_{out}(0)$ to a much higher value compared to noise, e.g., in the mV range. However, a high loop gain always requires high power consumption. The latter approach can be realized by a suitable DC bias, which is simple and consumes negligible extra power.

Start-up phase condition

As shown in Eq. 3.15, the initial phase ϕ_0 depends on the initial voltage condition, i.e. , $v_{out}(0)$. At t=0, Eq. 3.15 can be written as

$$v_{out}(0) = |v_{out}(0)| \cdot cos(\phi_0) \tag{3.20}$$

So, the solution of ϕ_0 equals 0 when $v_{out}(0)$ is positive, while ϕ_0 is π when $v_{out}(0)$ is negative. The oscillation start-up phases have 180 degree difference under different signs of the initial voltage $v_{out}(0)$, this in turn introduces the biphase modulation function. As a conclusion, a properly controllable DC bias asymmetry of the oscillator core simultaneously enables a fast oscillation start-up and biphase modulation.

Turn-off time

For generating sub-nanosecond UWB impulses, the LC oscillator is turned on only briefly, even though the amplitude of the oscillation envelope is smaller than v_p. The circuit implementation for generating the on-chip control signal to switch on and off the oscillator will be discussed in the following section. As soon as the tail current of the cross-coupled pair become too small to introduce sufficient negative impedance, the oscillation subsides. During this turn-off transient, the oscillator creates a damped oscillation. According to [46], the output waveform during the turn-off period can be written as

$$v_{out} = v_m e^{-\lambda t} cos(\omega_0 t + \phi_1) \tag{3.21}$$
$$= A_2(t) cos(\omega_0 t + \phi_1) \tag{3.22}$$

where v_m is the initial amplitude at the moment the oscillator is turned off, λ is the exponential decay coefficient and equals $2G_T/C$, ϕ_1 is the initial phase. Here, we define that the turn-off time t_f is the time needed for the envelope amplitude to fall down to $0.1 \cdot v_m$. Calculated from Eq. 3.21, t_f is given by

$$t_f = \frac{ln(10)}{\lambda} \approx \frac{2.3C}{G_T} \tag{3.23}$$

A fast turn-off performance is also critical for short UWB impulse generation. From Eq. 3.23, a small turn-off time can be realized by a small value of R_P. However, this small resistance reduces the open loop gain, which in turn increases the start-up time.

As discussed before, $v_{out}(0)$ is set to be in the mV range to introduce a fast start-up, and it can largely compensate the negative influence of this small resistance R_P. So a short impulse can be generated by briefly turning on the LC oscillator, as shown in Fig. 3.4.

3.3.2 Circuit Design

The impulse generation concept discussed in section 3.3.1 requires a control signal to briefly switch on the oscillator. In this design, the control signal is generated by a Schmitt trigger together with a current spike circuit. So, the complete impulse generator circuit targeting the FCC mask comprises three function blocks: a Schmitt trigger, a current spike circuit and an LC oscillator, as shown in Fig. 3.5.

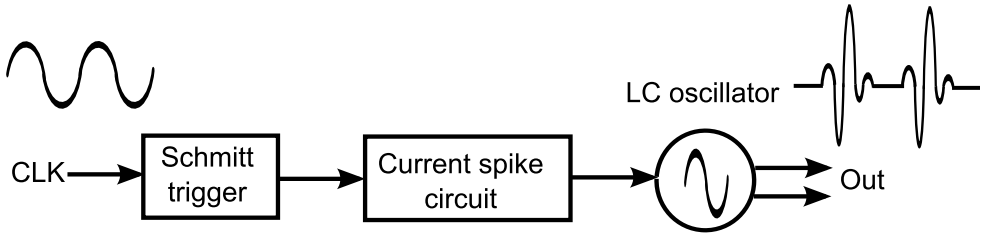

Fig. 3.5: Block diagram of the differential UWB impulse generator targeting for the FCC indoor mask.

The Schmitt trigger and the current spike circuit generate a current pulse train with a repetition rate equal to the input clock frequency. These current spikes generate sub-nanosecond UWB impulses with a repetition rate equal to the input clock frequency. The complete circuit schematic of this impulse generator can be seen in Fig. 3.6. The functionality of the individual block will be analysed in the following part.

Schmitt trigger

As shown in Fig. 3.6, the Schmitt trigger is implemented by a comparator incorporating positive feedback. In this design, the transistor T_1 is biased in its off state, while the output voltage of the Schmitt trigger is low because T_2 is conducting. As soon as a positive input clock signal triggers T_1 to be on, the voltage potential at the collector of T_2 immediately increases to high and close to V_{CC} owing to the positive feedback through R_f, with T_2 off. The threshold input voltage for switching between the two states can be very low through careful biasing of T_1. Therefore the impulse generator can operate with very low input power levels. The output voltage of the Schmitt trigger becomes low again immediately after the positive input signal disappears. A square-wave signal with an extremely short transition time in picoseconds is generated by the Schmitt trigger, which eliminates the time-domain influence of the input clock signal.

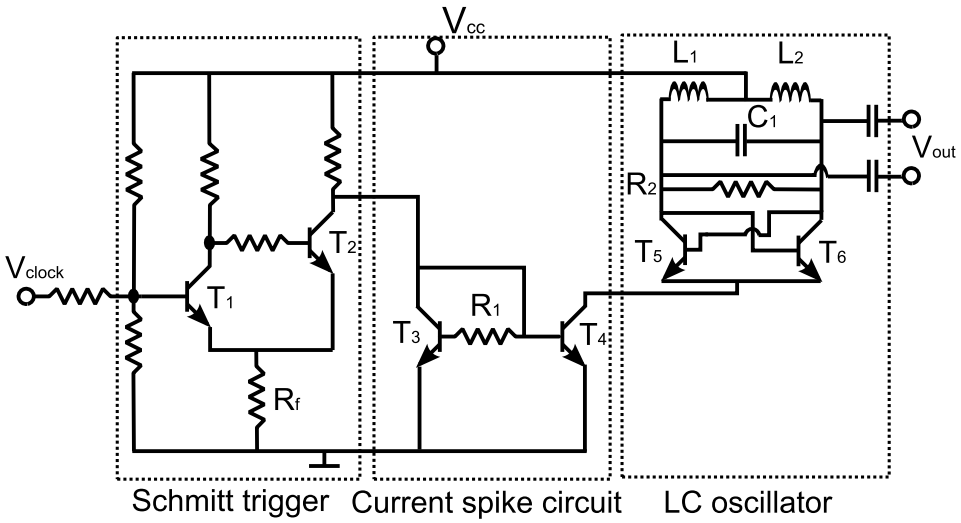

Fig. 3.6: Complete circuit schematic of the proposed differential impulse generator. Circuit details can be found in Appendix A.1.

Current spike circuit

A current spike is generated at every rising edge of the square wave as the output of the Schmitt trigger is connected to the current spike circuit. When the Schmitt trigger provides a high voltage potential at the collector of T_2, the current mirror of T_3 and T_4 will bring that high potential down to the built-in base-emitter potential of T_4. So the voltage potential at the collector of transistor T_3 has a spike performance before it becomes stable, and this corresponds to a current spike at the collector of T_4, as illustrated in Fig. 3.7.

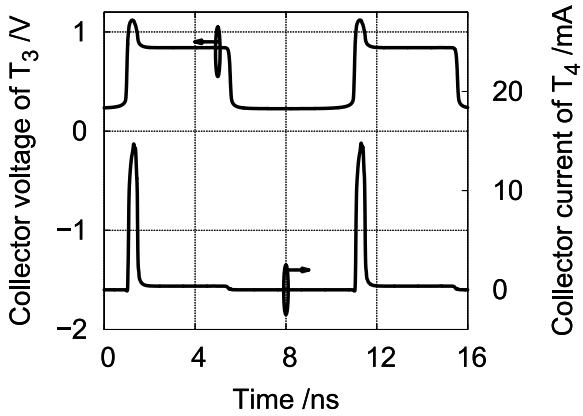

Fig. 3.7: Transistor level simulations: the collector potential of T_3 and the collector current of T_4.

The width of the current spike will be mainly determined by the time constant of the charging circuit formed by R_1 and the base-emitter capacitance C_{BE3} of T_3. This time constant τ of the charging circuit can be written as

$$\tau = R_1 C_{BE3} \tag{3.24}$$

Therefore, the current spike width can be precisely controlled by the resistance value R_1 and the size of T_3. The full width at half maximum (FWHM) of the spike envelope is a more precisely measurable figure, and it shows a simulated result of 0.4 ns in this design. During the rest of a period, the collector current of T_4 is too low to turn the following cross-coupled oscillator on because T_3 is chosen much larger than T_4. Furthermore, the amplitude of the current spikes can be easily adjusted by changing the size of T_4. The repetition rate of the current spike train is equal to the input CLK frequency and is limited by the spike width. This novel spike generation scheme is capable of output repetition rates well into the GHz range. The Schmitt trigger and the current spike circuit draw 2.4 mA current under the 1.5 V supply, which is nearly independent of the input clock frequency.

LC oscillator

As depicted in Fig. 3.6, a cross-coupled pair formed by T_5 and T_6 provides negative impedance for the oscillator core. The resonator of this oscillator includes two inductors, one capacitor and a parallel resistor. The LC oscillator is turned on by the current spikes generated on-chip once the collector currents of the cross-coupled pair are high enough to create a negative real part of the impedance at the collector terminals. Here, the sizes of T_5 and T_6 are different, creating the unambiguous initial voltage condition $v_{out}(0)$ in the mV range. According to the investigation in Sec. 3.3.1, this setting shortens the start-up time and also ensures that the oscillation starts up always with the same phase, which makes the generated impulses suitable for both correlation and energy detection schemes. The fast start-up is required to minimize the required pulse width of the current spikes for a given duration of the generated UWB impulse, this in turn reduces the power consumption. The functionality of R_2 is to quench the oscillator off quickly immediately after the current spike has disappeared, which is necessary for short time-domain impulses, as discussed in Sec. 3.3.1. The centre frequency ω_0 of the UWB impulses is determined by L_1, L_2, C_1 as well as the parasitic capacitance C_{para}, it can be expressed as

$$\omega_0 = \frac{1}{\sqrt{(C_1 + C_{para})(L_1 + L_2)}} \tag{3.25}$$

For a good compliance with the FCC mask, the centre frequency is set at 6 GHz. The output is decoupled by two large capacitors. No buffer stage is employed, further decreasing the complexity of the circuit and the power consumption. Thus, short time-domain impulses with a repetition rate equal to the input clock frequency are generated. Fig. 3.8 illustrates the simulated results of the generated 200 MHz impulse sequence and the corresponding input clock signal. As can be seen, a UWB impulse is generated at every rising edge of the input clock signal.

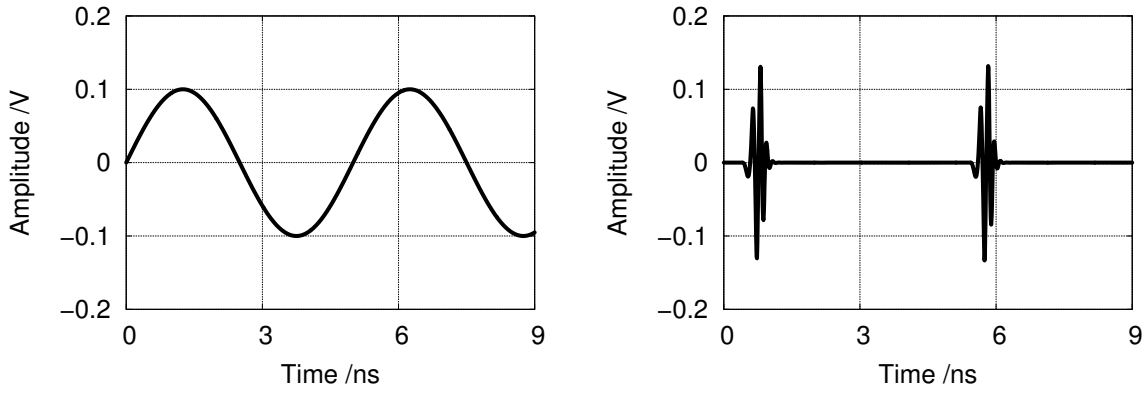

Fig. 3.8: Simulated waveforms of (a) the input clock signal with a frequency of 200 MHz and (b) the generated impulse sequence with a repetition rate equal to the input clock frequency.

The microphotograph of the realized impulse generator IC can be seen in Fig. 3.9. Due to a simple circuit topology, the IC is compact with an overall area of 0.6 x 0.5 mm^2 including bond pads. For characterization, the chip was mounted on a 0.5 mm-thick Rogers R04003C substrate and wire-bonded to external microstrip transmission lines. An SMD chip capacitor is placed in close proximity to the V_{cc} port.

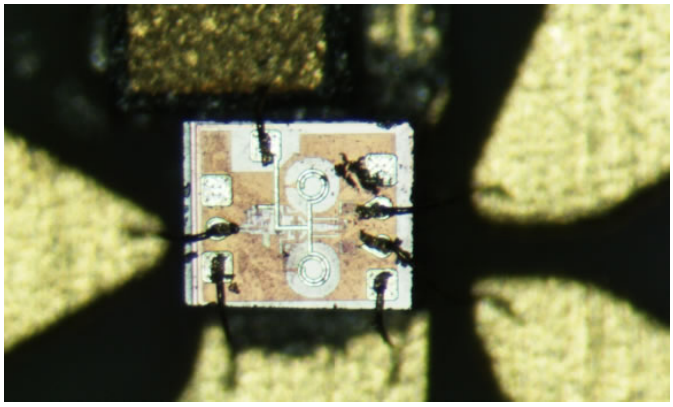

Fig. 3.9: Microphotograph of the realized impulse generator IC. Chip size is 0.3 mm^2.

3.3.3 Measurement Results

The measurements were performed using a sinusoidal continuous-wave signal source to generate the input signal to the impulse generator. The two differential output ports were connected to two channels of a real time oscilloscope with a bandwidth of 13 GHz. The differential output is extracted using the subtraction feature of the oscilloscope. First, the fabricated impulse generator was fed with a 100 MHz sinusoidal

input signal with a power level of -15 dBm. The measured waveform in comparison with the simulation result is seen in Fig. 3.10. It clearly indicates that the simulation

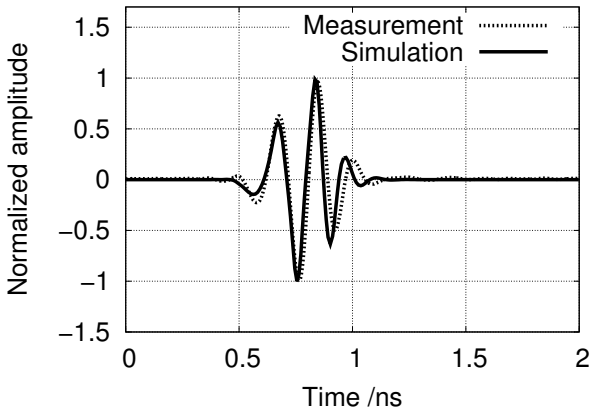

Fig. 3.10: Measured and simulated impulse waveforms. Here the waveforms are normalized for a good comparison.

and measurement results are in good agreement. The measured output impulse sequence with a repetition rate of 100 MHz is shown in Fig. 3.11 (a). The overall power consumption at this rate is 6 mW under a 1.5 V supply voltage, this corresponds to an energy consumption of 60 pJ per pulse. As can be seen, the measured impulses have a peak-peak amplitude of 210 mV, and the impulse envelope has a FWHM of 0.3 ns.

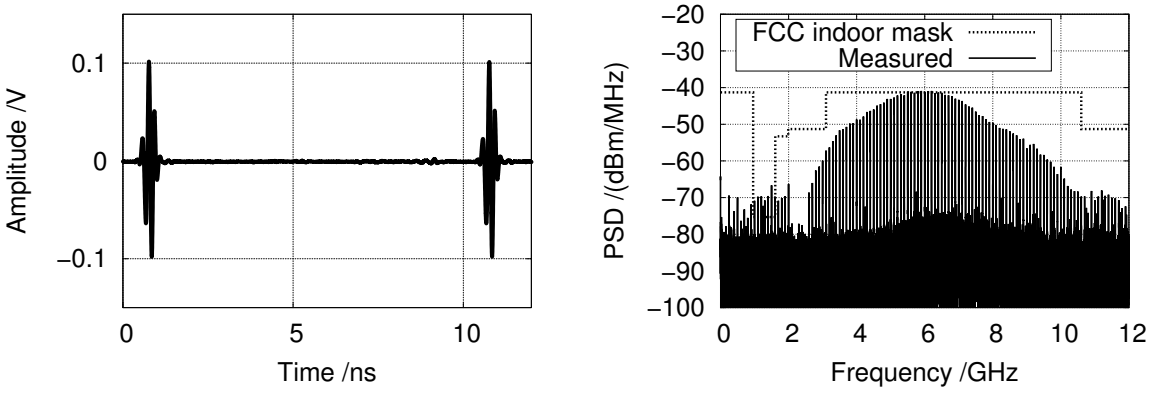

Fig. 3.11: Measured results of the 100 MHz impulse train in (a) time and (b) frequency domain.

Fig. 3.11 (b) depicts the spectrum of the measured 100 MHz impulse train. The measured result shows a maximum PSD of -41.3 dBm/MHz. It has a 10 dB bandwidth of 4.9 GHz from 3.5-8.4 GHz with the centre frequency around 6 GHz. It can be seen that the output spectrum complies well with the FCC spectral mask for indoor UWB

applications. It is worth to mention that the spectra do violate the mask in the GPS notch, however, this will be remedied by the antenna frequency response.

Secondly, the circuit was tested at 200 MHz and 1.3 GHz input frequencies, respectively. The measured output waveforms can be seen in Fig. 3.12. It shows that the

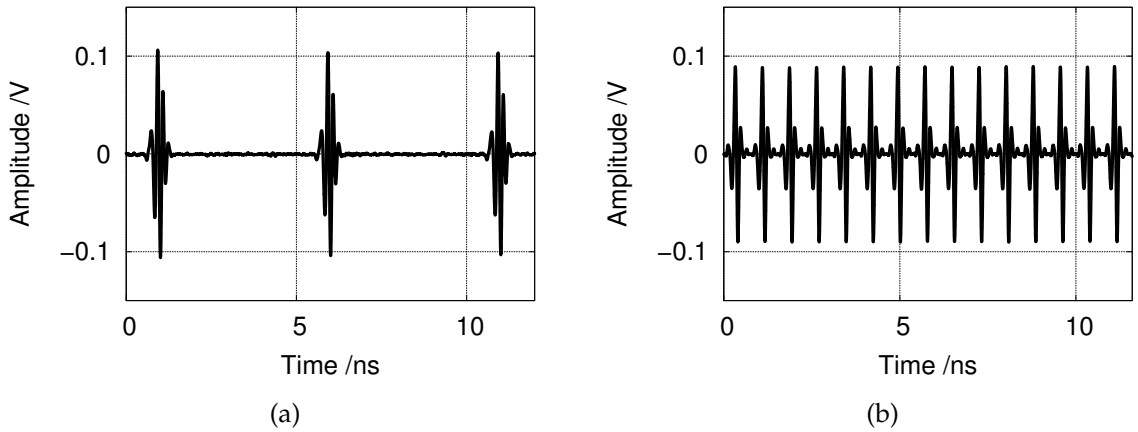

Fig. 3.12: Measured output UWB impulse waveforms at (a) 200 MHz and (b) 1.3 GHz input frequencies.

realized circuit generates uniform impulses in terms of pulse shape and amplitude up to 1.3 GHz. The circuit can also work in excess of 1.3 GHz, but with a degraded performance. This is mainly because either transistor T_1 or T_2 is in saturation, and the bipolar transistors need some time to recover from saturation. The complete impulse generator consumes 6.5 mW at 200 MHz and 9.7 mW at 1.3 GHz impulse repetition rates, and the energy consumption per pulse is 32.5 pJ and 7.4 pJ, respectively.

Fig. 3.13 illustrates the energy consumption per pulse versus the output impulse repetition rate. It indicates that the impulse generator has a lower energy consumption

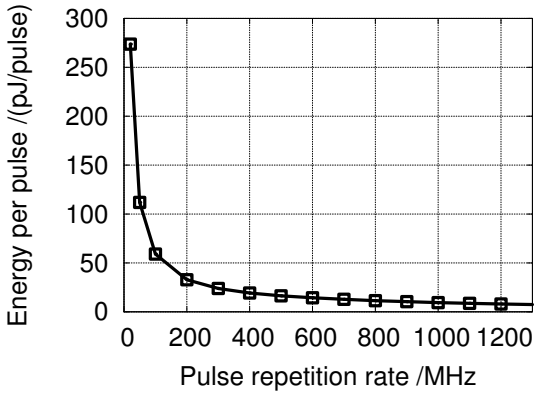

Fig. 3.13: Measured energy consumption per pulse versus output impulse repetition rate. It decreases with increasing repetition rate.

per pulse at higher output impulse repetition rate. This is due to the frequency-independent power consumption of the Schmitt trigger together with the current spike circuit. As can be seen, the energy consumption per pulse is smaller than 10 pJ when the output impulse repetition rate is larger than 800 MHz.

In order to construct the complete UWB transmitter, a dipole fed circular slot antenna is employed. The antenna is provided through the project collaboration with the Institute of Microwave Techniques at UIm University and is realized on a Rogers RO4003C substrate. It has a circular aperture in the ground plane and a broadband dipole element on the reverse side exciting this aperture. Measured results show a quite uniform radiation pattern over the band from 3.1-10.6 GHz and a mean gain of 2.9 dBi. More detailed information on the antenna can be found in [48]. The impulse generator IC is mounted on the substrate where the dipole fed circular slot antenna is realized and wire-bonded to the feed-lines, as shown in Fig. 3.14. A commercial voltage regulator is employed to allow the transmitter to operate from a 6 V battery supply. Transient measurements of the UWB transmitter both in the E-plane and H-

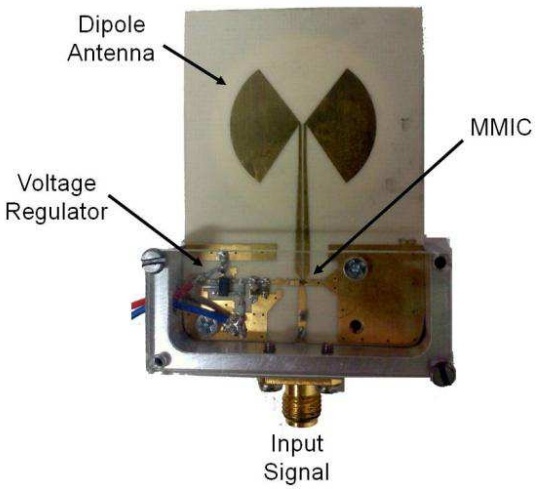

Fig. 3.14: Photograph of the front view of the complete transmitter.

plane were performed. The measured results are illustrated in Fig. 3.15. The pictures show the measured normalized voltage amplitude against azimuth angle and time. The data between -0.2 and 0.3 ns clearly shows the multi-cycle impulse in the time domain. It can be seen that the differential antenna has a very wide beam-width, which is helpful for communication applications.

3.4 Differential Tunable Impulse Generator

The impulse generator presented in section 3.3 is easily modified to introduce tunability. This section explains the circuit implementation to achieve the tunable function and presents the measured results of the realized IC.

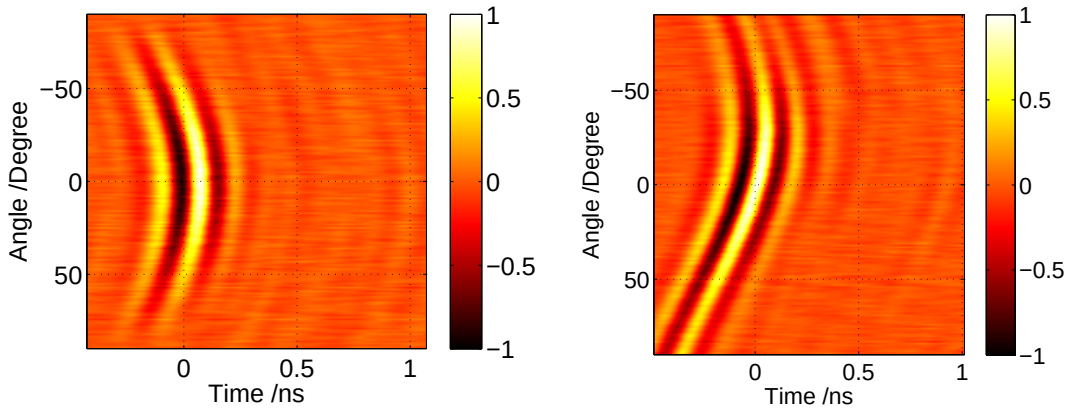

Fig. 3.15: Normalized received amplitudes in the (a) E-plane and (b) H-plane.

3.4.1 Circuit Implementation

As discussed in section 3.3.2, the current spike width is mainly determined by the resistance value R_1 and the size of transistor T_3 shown in Fig. 3.6. Here, a control circuit is introduced to generate a configurable current spike width. This leads to a tunable duration of the generated impulses, whose spectrum correspondingly has a controllable 10 dB bandwidth. Meanwhile, a varactor is used in the oscillator core to adjust the centre frequency of the impulses. The complete block diagram of this impulse generator can be seen in Fig. 3.16. The two tuning voltages (V_{tune1} and V_{tune2}) set the impulse parameters to conform to the spectral allocations in the USA, Europe and Japan. To the best of the author's knowledge, this is the first pulse source with direct pulse generation adaptable to all the three bands.

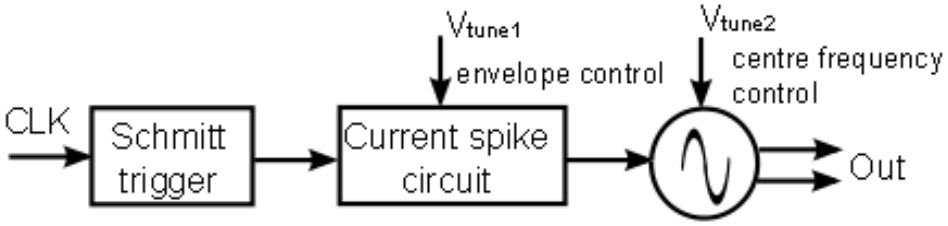

Fig. 3.16: Block diagram of the differential tunable UWB impulse generator.

Fig. 3.17 plots the complete schematic of the tunable impulse generator. Compared to the circuit shown in Fig. 3.6, two modifications have been done: a parallel capacitor C_{B3} which is switched in and out by transistor T_7 is inserted and a varactor C_2 is placed in series with capacitor C_1. The capacitance value of C_{B3} is 2 pF. Consider Fig. 3.17, when $V_{tune1} = 0$, the transistor T_7 is off and the charging circuit only includes R_1 and C_{BE3}. The time constant τ of the charging circuit is the same as in Eq. 3.24. When $V_{tune1} = 1$ V, T_7 is on. For simplicity, the transistor T_7 can be treated as an ideal switch

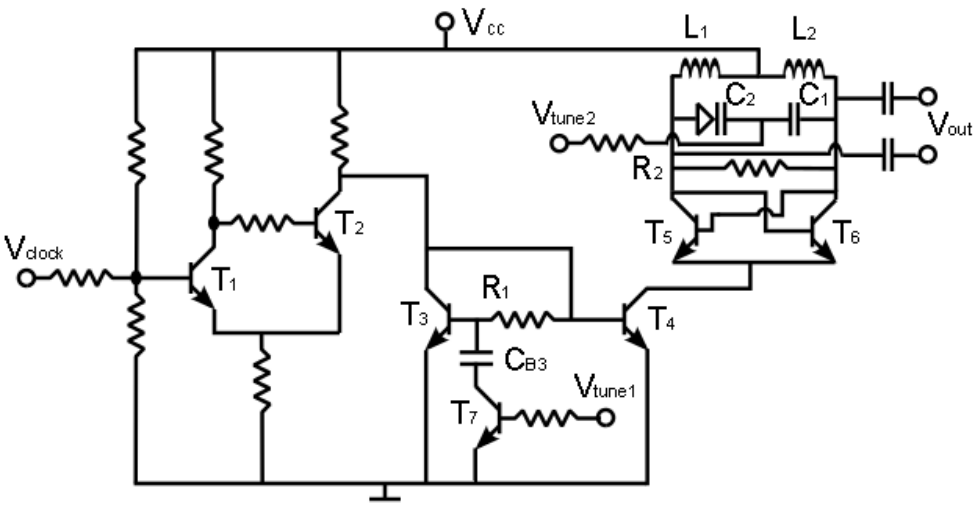

Fig. 3.17: Complete circuit schematic of the impulse generator tunable to FCC, ECC and Japanese masks. Detailed circuit parameters are presented in Appendix A.2.

here and the charging circuit includes R_1 and C_{BE3} in parallel with C_{B3}. In this case, the time constant τ can be written as

$$\tau = R_1(C_{BE3} + C_{B3}) \tag{3.26}$$

In the latter case, the current spike width will be much wider because C_{B3} is much larger than C_{BE3}. By suitable selection of the resistance value of R_1, the current spike has a FWHM of either 0.4 ns or 2 ns. The different spike widths correspondingly introduce different durations of the oscillation, as indicated in Fig. 3.18.

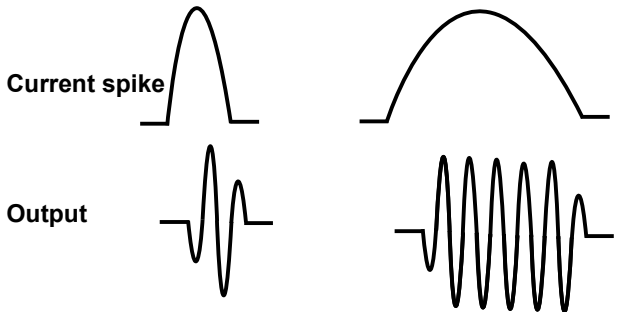

Fig. 3.18: The relationship between the current spike width and the output oscillation signal.

Different from Fig. 3.6, the circuit here employs a varactor inside of the oscillator core. The centre frequency ω_0 is determined by L_1, L_2, C_1, C_2 as well as the parasitic capacitance C_{para}. It can be expressed as

$$\omega_0 = \frac{1}{\sqrt{(\frac{C_1 C_2}{C_1+C_2} + C_{para})(L_1 + L_2)}} \tag{3.27}$$

where the value of C_2 is controlled by the control voltage V_{tune2}. Consequently, ω_0 is directly related to V_{tune2}.

As a conclusion, when the shorter spike current with V_{tune1} = 0 triggers the oscillator, the generated impulse will be very short. The corresponding spectrum has a large 10 dB bandwidth and complies with the FCC mask. Under the condition of V_{tune1} = 1 V, multi-cycle impulses with a reduced 10 dB bandwidth are generated. The oscillation in this mode is quenched off after a certain duration. By adjusting the centre frequency ω_0 by changing the varactor capacitance C_2, it suits either the ECC or the Japanese spectral mask. The microphotograph of the realized tunable impulse generator is shown in Fig. 3.19. It is a compact design with an area of 0.53 x 0.61 mm^2.

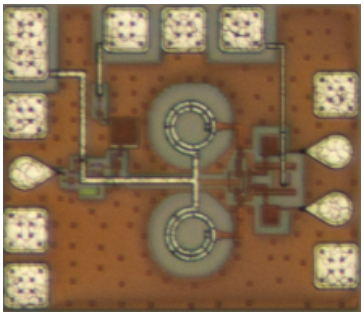

Fig. 3.19: Microphotogragh of the realized impulse generator IC. This compact design has an area of 0.32 mm^2.

3.4.2 Measured Results

The tunable impulse generator was measured on wafer. Ground-signal-ground (GSG) and ground-signal-signal-ground (GSSG) microwave probes with a 100 μm pitch were used to connect the input and output ports of the circuit. The circuit was tested with a 100 MHz sinusoidal input signal.

A. Targeting the FCC mask

By setting V_{tune1} = 0 and V_{tune2} = 2.0 V, the generated impulses target the FCC mask. Now the LC oscillator is triggered with shorter current spikes generated on chip. Fig. 3.20 (a) shows the measured 100 MHz impulse train in the time domain. The measured sub-nanosecond impulses have a peak-peak amplitude of 0.36 V. As can be seen, the FWHM of the envelope for these impulses is around 0.4 ns. The circuit consumes a total power of 6 mW. The output impulse repetition rate in this mode can be up to the GHz range. Fig. 3.20 (b) plots the normalized PSD of this impulse

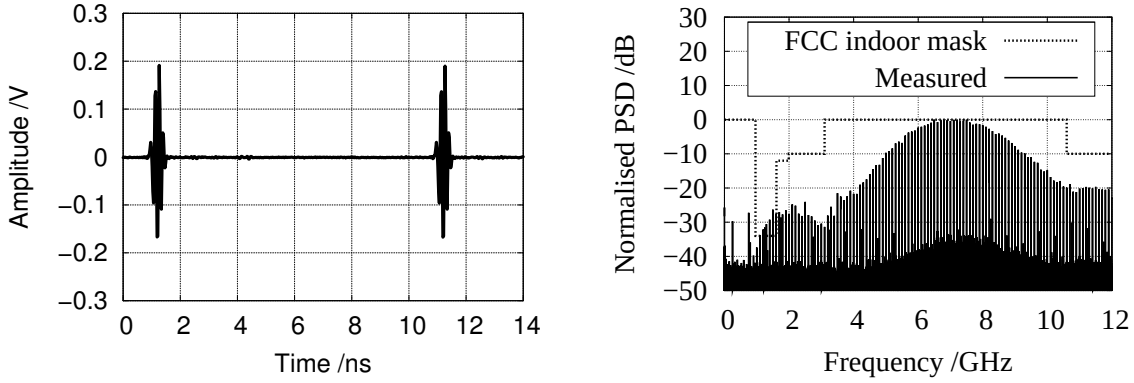

(a) (b)

Fig. 3.20: Measured impulse train in (a) time and (b) frequency domain. The output spectrum complies well with the FCC indoor mask.

train complying with the normalized FCC mask for indoor systems. In general, the maximum EIRP also depends on the gain of the transmission antenna, the impulse repetition rate and the modulation type. A normalized PSD can sufficiently show the fitness for the spectral mask. This impulse train has a 10 dB bandwidth of 4.2 GHz from 5 to 9.2 GHz with the center frequency around 7 GHz. It can be seen that the output spectrum complies well with the FCC indoor mask.

B. Targeting the ECC mask

The impulse generator is suitable for the ECC mask when V_{tune1} = 1 V and V_{tune2} = 2.3 V. The LC oscillator is triggered with a longer current spike with a FWHM of 2 ns under these conditions. The measured output impulse train in the time domain can

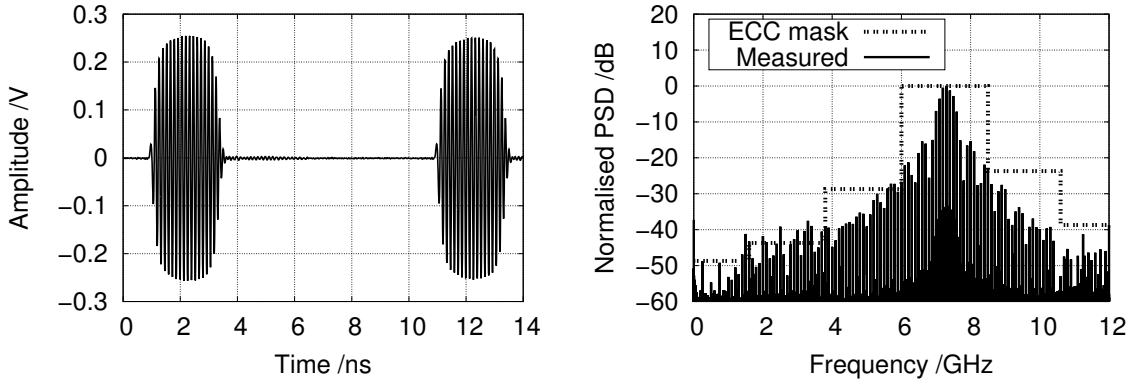

(a) (b)

Fig. 3.21: Measured impulse train with a repetition rate of 100 MHz rate in (a) time and (b) frequency domain under the ECC mode.

be seen in Fig. 3.21 (a). The impulses have a peak-peak amplitude of 0.5 V and the

FWHM of the envelope is around 2 ns. The circuit has a total power consumption of 10 mW and a maximum output impulse repetition rate exceeding 300 MHz in this situation. Fig. 3.21 (b) shows the spectrum information of the measured 100 MHz impulse train. It has a centre frequency around 7 GHz with a 10 dB bandwidth of 600 MHz. As can be seen, the output spectrum fits well into the ECC mask.

C. Targeting the Japanese mask

Through changing the value of V_{tune2}, the center frequency of the impulses will be shifted. Fig. 3.22 (a) shows the measured time-domain waveforms. In this measure-

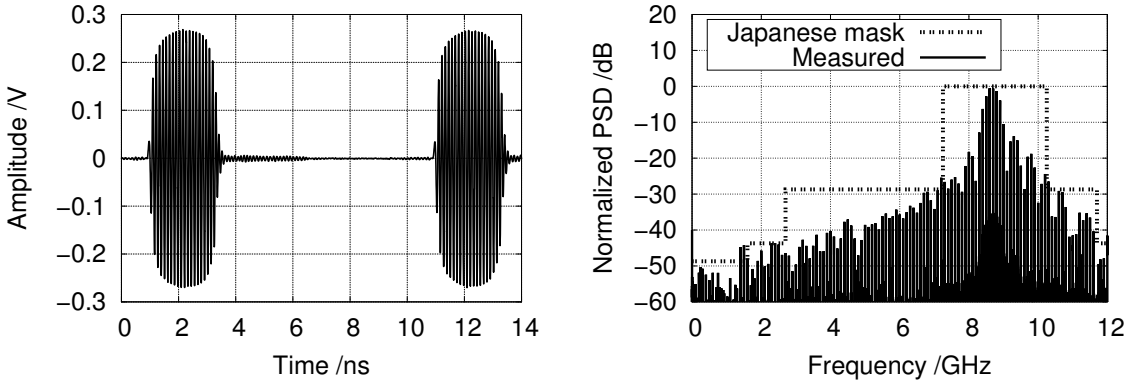

(a) (b)

Fig. 3.22: Measured impulse train with a repetition rate of 100 MHz rate in (a) time and (b) frequency domain with targeting the Japanese mask.

ment, V_{tune1} = 1 V and V_{tune2} = 6 V. The measured impulse train has a similar envelope as in the last case because the triggering current spike has the same width. The peak-peak amplitude of the impulses, whose envelope has a FWHM of 2 ns, is 0.5 V. The complete power consumption in this mode is 10 mW. The spectrum information is plotted in Fig. 3.22 (b). It shows that the centre frequency is shifted to 8.7 GHz, leading to a good fit with the Japanese mask. The performance measured on wafer under these three modes are summarized in Tab. 3.1. As a conclusion, this circuit

Target	V_{PP} /V	FWHM of the envelope /ns	10 dB BW /GHz	Power cons. /mW
FCC V_1=0, V_2=2.0 V	0.36	0.4	4.2	6
ECC V_1=1 V, V_2=2.3 V	0.5	2	0.6	10
Japanese mask V_1=1 V, V_2=6 V	0.5	2	0.6	10

Tab. 3.1: Performance summary of the tunable impulse generator.

shows a low power consumption under all these three modes. The tunable function is easily achieved by adjusting two control voltages. This impulse generator can be used for OOK and PPM schemes in all these three modes.

The impulse generator IC is also mounted on a RO4003C laminate which is packaged in an aluminium case, as shown in Fig. 3.23 (a). SMA connectors are employed

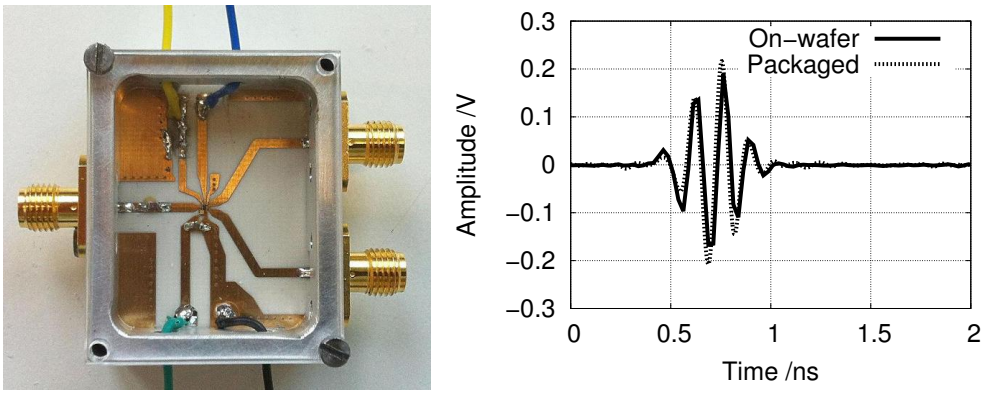

(a) (b)

Fig. 3.23: (a) Picture of the packaged circuit and (b) comparison of the packaged and on-wafer measured impulse waveforms.

for characterizing the performance of the transmitter. In Fig. 3.23 (b), the measured time-domain waveform targeting the FCC indoor mask can be seen. It is compared with the result measured on wafer under the same settings. It can be seen that the packaging only has a negligible influence. The slight increase of the amplitude of the packaged version is due to omitting feed cables used in the on-wafer measurement which cause slight attenuation. The measurement results in the other two modes also show great agreement with results measured on wafer.

3.5 Differential Impulse Generator with BPM Function

BPM capability can be introduced by modifying the DC currents flowing in the individual branches of the cross-coupled LC oscillator. This section explains the circuit implementation to achieve biphase modulation function and shows the measured results of the successfully realized IC.

3.5.1 Circuit Implementation

The block digram of the impulse generator with the BPM function can be seen in Fig. 3.24. Different from the impulse generator design presented in Sec. 3.3, a phase control circuit is employed to introduce a controllable asymmetry in the oscillator core,

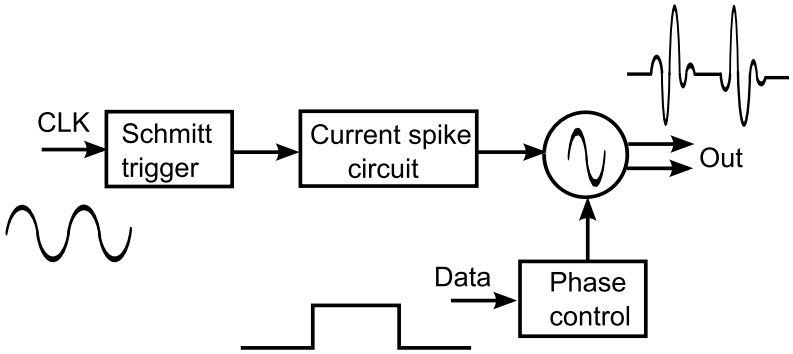

Fig. 3.24: Block diagram of the differential UWB impulse generator with BPM function.

which in turn generates controllable start-up phase conditions. This property realizes the BPM functionality.

The complete circuit schematic of this impulse generator is plotted in Fig. 3.25. Compared to the circuit plotted in Fig. 3.6, a phase control circuit determining the DC current flowing in the individual branch of the oscillator core is added. Furthermore, T_5 and T_6 have the same size. As shown in Fig. 3.25, additional branch currents are injected through current mirrors implemented with T_7, T_9 and T_8,T_{10}. If the input data signal is low, transistor T_9 blocks, and the collector current I_1 of T_7 is zero due to the current mirror configuration. At the same time, the supply voltage V_1 lets T_{10} conduct, this correspondingly introduces a collector current I_2 of T_8 owing to the current mirror configuration of T_8 and T_{10}, because T_{11} is off. The current I_2 causes a

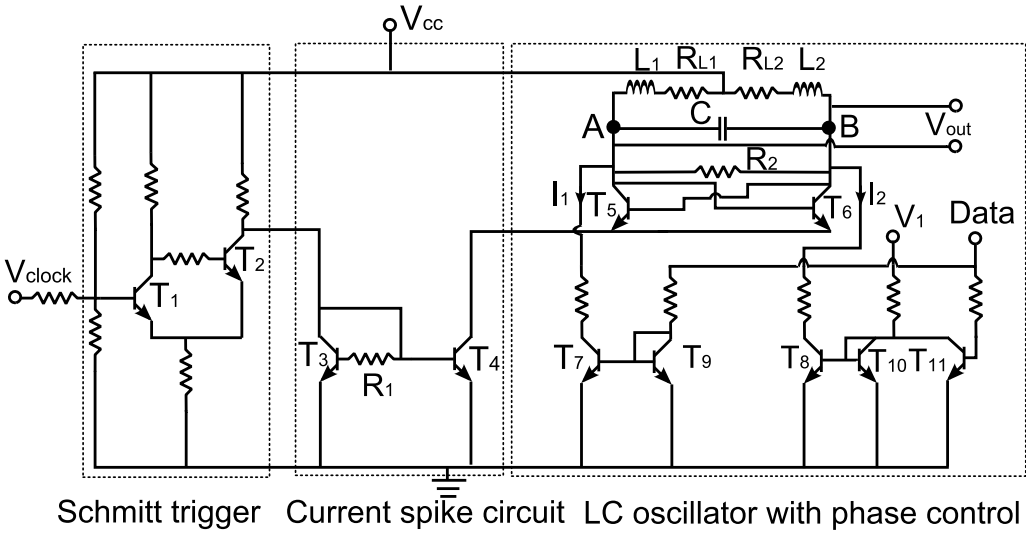

Fig. 3.25: Complete circuit schematic of the differential impulse generator with BPM function. Detailed circuit parameters can be found in Appendix A.3.

voltage drop through the resistor R_{L2} which is connected in series with the inductor L_2. As a result, the voltage potential at point B is lower than that at A, which

makes the initial voltage condition $v_{out}(0)$ positive. If the input data signal is high, the transistor T_{11} switches into saturation, correspondingly, T_{10} blocks. As a result, the collector current I_2 of T_8 is zero. Meanwhile, T_9 is turned on, which introduces a collector current I_1 in T_7. In this situation, the voltage potential at point B is larger than that at A, making $v_{out}(0)$ negative. As a conclusion, different applied data signal levels generate opposite signs of the initial voltage condition.

According to Eq. 3.20, the initial phase ϕ_0 depends on the initial voltage condition $v_{out}(0)$, i.e., the solution of ϕ_0 equals 0 if $v_{out}(0)$ is set to positive, while ϕ_0 is π when $v_{out}(0)$ is negative. The LC oscillator will start up in one of these two phase states as soon as the collector current of the tail transistor T_4 is high enough to create a negative real part of the impedance at the collector terminals of the cross-coupled pair (T_5 and T_6). This controllable phase condition introduces a BPM function. Additionally, the different voltage potentials at points A and B with an amplitude in mV range significantly shortens the start-up time, according to Eq. 3.19.

Fig. 3.26 shows the micro-photograph of the realized impulse generator IC. It is a quite compact design with an overall area of 0.3 mm^2. It is worth to mention that this UWB impulse generator can also be used for OOK and PPM schemes, using appropriately modulated input signal.

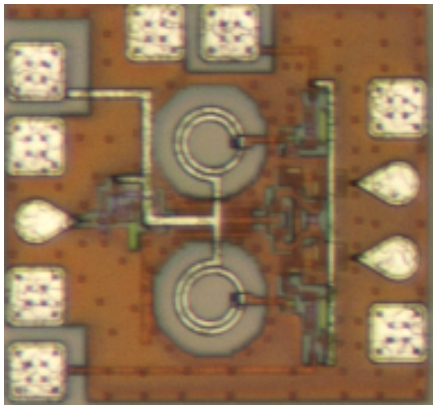

Fig. 3.26: Microphotogragh of the realized impulse generator IC. This compact design has an overall area of 0.56 x 0.53 mm^2 including bond pads.

3.5.2 Measured Results

First, the IC was characterized on wafer using microwave GSG and GSSG probes. The input clock port was fed with a 200 MHz sinusoidal signal with a power level of -15 dBm, while the data port is connected to ground. Fig. 3.27 depicts the measured time-domain waveform in comparison with the simulation result. It can be seen that both results are in excellent agreement. The measured impulse waveform has a peak-peak amplitude of 260 mV and an envelope width of 0.3 ns FWHM. Additionally, the impulse shape shows a great symmetry with fast start-up and turn-off. The complete

power consumption under this set-up is 8.7 mW, which corresponds to an energy consumption of 43.5 pJ per pulse.

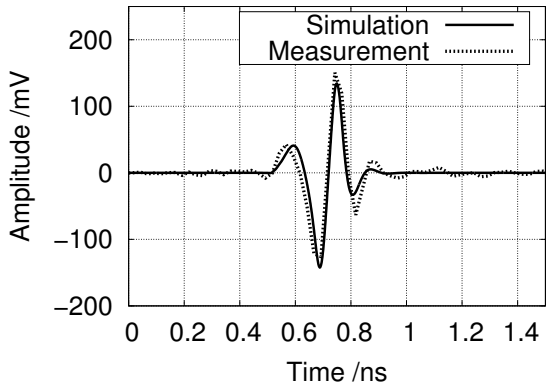

Fig. 3.27: Comparison of the measured and simulated impulse waveforms with the data port shorted to ground.

Then, different voltages (either 0 or 1.2 V) were applied to the data port with the purpose of demonstrating the BPM performance. The measured results with a 200 MHz clock signal is shown in Fig. 3.28. It can be seen that the orientation of the

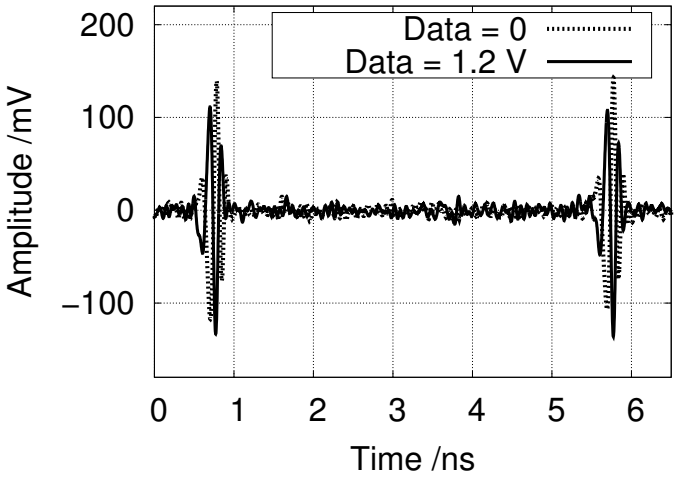

Fig. 3.28: Measured impulses with different applied data signal in time domain. The results show a perfect biphase modulation.

impulses is clearly reversed due to the opposite start-up phase conditions. A good BPM is achieved because the other parameters, such as the Q-factor and resonant frequency are identical, the impulse shapes are almost the same under these two conditions. The complete power consumption is 10.6 mW when the 1.2 V voltage applied on the data port, which is slightly higher compared to the case of the data port connected ground. This is because a larger collector current is required to switch the transistor T_{11} into saturation.

Fig. 3.29 depicts the normalized spectra of the 200 MHz impulse trains with different applied data signals. Clearly, the very short impulses have an extremely large band-

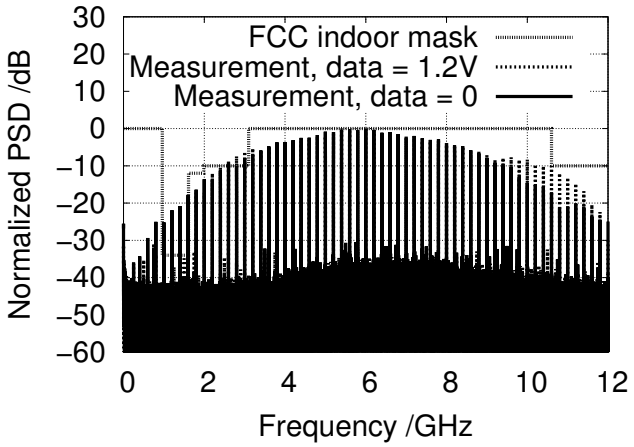

Fig. 3.29: Measured impulses with different applied data signal in frequency domain. The output spectra of the 200 MHz impulse trains in both situations comply well with the FCC indoor mask.

width. The measured 10 dB bandwidth is from 2.6 - 9.6 GHz when the data port is grounded, and from 2.6- 10.2 GHz if the data port is 1.2 V. The spectrum lines under these two set-ups overlap with each other quite well. The spectra do violate the mask in the GPS notch, however, this will be remedied by the antenna frequency response. The on-wafer measured results under the two set-ups are summarized in Tab. 3.2.

Mode (setting)	10dB bandwidth (GHz)	V_{pp} (V)	power cons. (mW)
data = 0	7	0.26	8.7
data = 1.2 V	7.6	0.26	10.6

Tab. 3.2: Performances of impulse generator with different applied voltages at the data port.

Furthermore, to demonstrate the high-speed performance, the IC was tested with a 1.2 GHz sinusoidal CLK signal. The measured impulse waveforms are shown in Fig. 3.30 (a). It can be seen that the impulse shape is still symmetric. The circuit has a low power consumption of 15 mW with data port grounded, and 17 mW with data port connected to 1.2 V. The corresponding energy consumption per impulse is 12.5 pJ and 14.2 pJ respectively. Another experiment was performed to verify the IC can generate a biphase modulated impulse sequence. Fig. 3.30 (b) displays the measured clock signal, modulated data signal and measured modulated impulse sequence. The total power consumption of the impulse generator is 9.8 mW in this mode of operation.

The impulse generator IC is again mounted on an RO4003C substrate and packaged in an aluminium case, as shown in Fig. 3.31 (a). The packaged IC is measured under

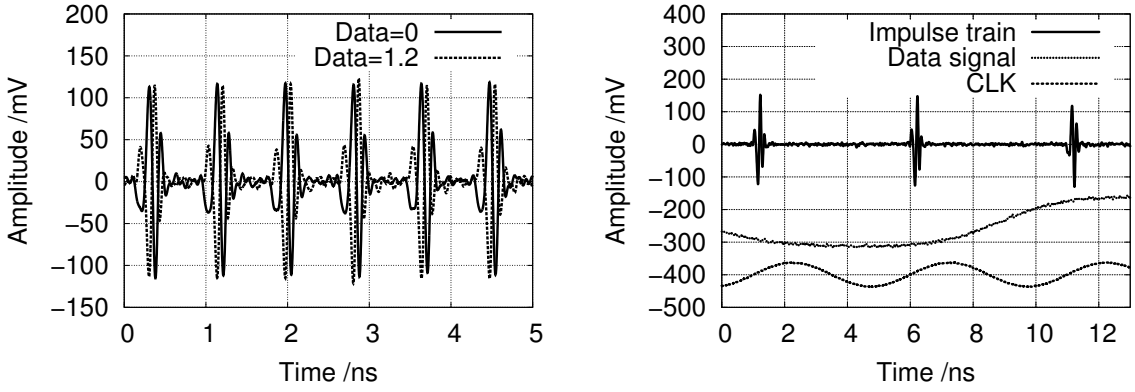

(a) (b)

Fig. 3.30: (a) Measured 1.2 GHz impulse trains with different applied voltages at the data port and (b) impulse sequence of an applied modulation signal through data port.

the conditions that the clock port is fed with a 200 MHz sinusoidal signal and the data port is grounded. Fig. 3.31 (b) displays a comparison of the measured waveforms. It can be seen that the packaging introduces negligible influence on the circuit performance. Fig. 3.31 (c) illustrates the impulse generator IC packaged together with a dipole fed circular slot antenna.

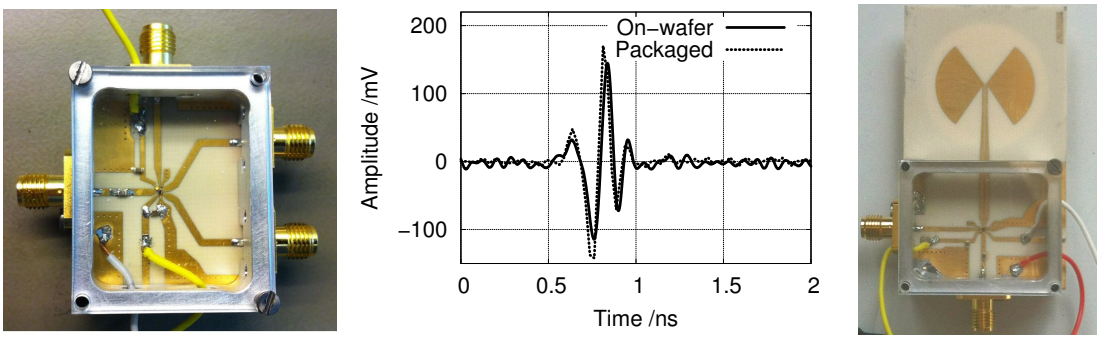

(a) (b) (c)

Fig. 3.31: (a) Package picture and (b) comparison between packaged and on-wafer measured impulse waveforms and (c) the complete transmitter.

3.6 In-body UWB Beacon Transmitter

This section describes the implementation of an active UWB beacon transmitter which can be integrated on catheter tips as a means of tracking interventional devices. Several techniques have been reported for catheter tracking, such as X-ray, electromag-

netic means based on nine coils [49], magnetic resonance imaging (MRI) [50] and ultra-sonic technique [51]. Among them, X-ray is the most common technique. Compared to X-ray, UWB technology has the advantage of very low energy radiation. Moreover, UWB approach has the property of lower complexity and decreased cost.

Here a UWB transmitter is designed as an active beacon to localize in-body interventional devices. Different from the previously described impulse generators, a high output voltage swing is required to partially compensate for the high attenuation in biological tissue. This is achieved by employing a UWB power amplifier (PA) to further amplify the generated impulses. For realizing a low power consumption, a sleep mode is introduced to the PA.

3.6.1 Transmitter Topology

Fig. 3.32 illustrates the block diagram of the proposed UWB transmitter. As can be

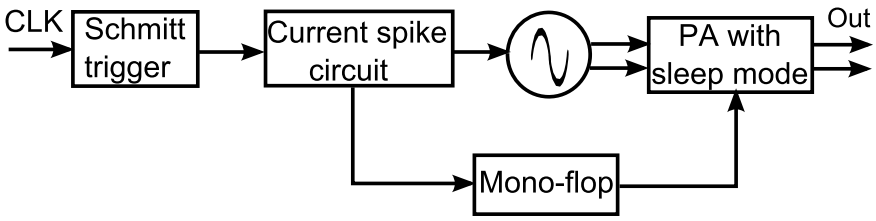

Fig. 3.32: Complete block diagram of the proposed differential UWB transmitter employed as an active beacon.

seen, the impulse generation principle is similar to the one described in Sec. 3.3.2. Different from the previous versions, a monoflop circuit and a UWB PA are added. A voltage spike train generated by the Schmitt trigger and the current spike circuit controls the monoflop circuit. The output of the mono-flop ensures that the PA is only turned on during the impulse generation period. This property significantly reduces the power consumption of the transmitter.

3.6.2 Impulse Generation and Monoflop Circuit

The schematic of the impulse generation circuit together with the mono-flop can be seen in Fig. 3.33. As discussed in Sec. 3.3.2, the Schmitt trigger and the current spike circuit generate current spikes to briefly switch on the LC oscillator. With proper selections of the transistor sizes and the passive component values, simulation results show that the generated impulses have an envelope width of 0.4 ns FWHM and an amplitude of 0.2 V_{pp} in this design. Meanwhile, the collector voltage spike in T_3 performs as the input signal to the monoflop circuit. The mono-flop circuit generates another voltage spike train with the spike width determined by the resistance R_2 and the capacitance C_2. These voltage spikes in turn generate current spikes at the

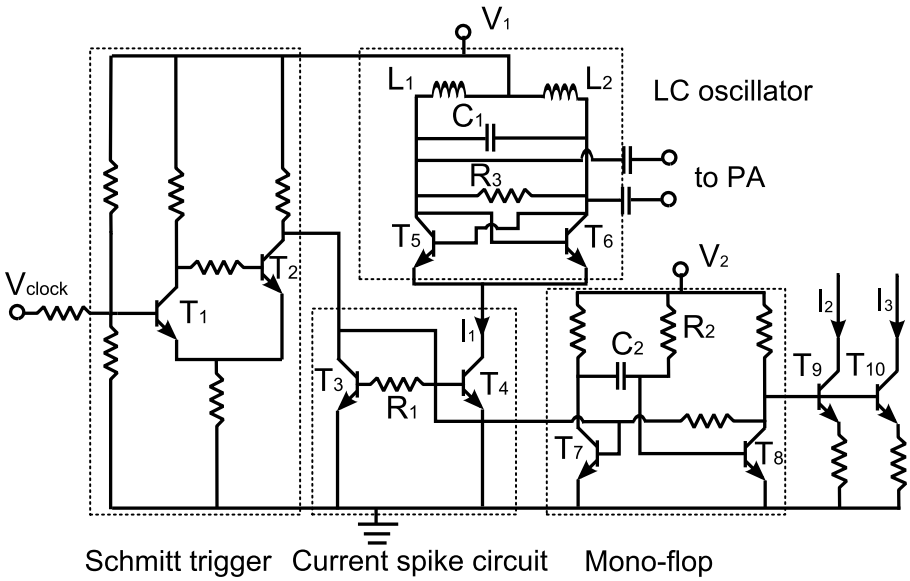

Fig. 3.33: Circuit schematic of the impulse generation circuit and the monoflop. Circuit details are given in the Appendix A.4.

collectors of T_9 and T_{10}, which are used to briefly activate the differential PA in the following stage.

Fig. 3.34 shows the simulated information of I_1, I_2 and the collector potential of T_3. As can be seen, the mono-flop delays I_2 slightly compared to I_1 in order to compensate the delay generated by the LC oscillator. So the differential UWB PA is turned on only when the generated impulses arrive at the PA. The widths of I_2 and I_3 are the same and selected according to the width of the impulses from the LC oscillator.

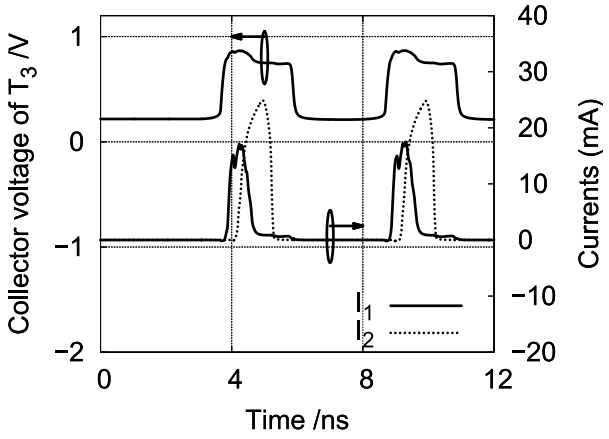

Fig. 3.34: Transistor level simulation: the collector potential of T_3, I_1, I_2.

3.6.3 Differential UWB Power Amplifier

A PA with wide bandwidth is required to further amplify the impulses from the LC oscillator since a high output voltage swing is required for in-body localizations. Several approaches for designing a wideband PA have been published. E.g., [52] proposes a distributed architecture to provide wide-band gain and shows an output 1 dB compression point (OP_{1dB}) above 5.6 dBm between 3-10 GHz. However, it occupies a large chip area and has a high power consumption. Another design, shown in [53], reports a single-ended PA adopting a current-reuse technique, inductive peaking and resistive feedback. Although this circuit topology is simple, the on-chip spiral inductors occupy a large chip area.

In this thesis a fully differential PA based on resistive feedback with a simple circuit topology is proposed, as illustrated in Fig. 3.35. The inductor-less design minimizes chip area while the resistive negative feedback results in near-constant group delay across the complete UWB band. The input and output are differential as the PA will be directly connected to the output of the LC oscillator and its output is fed to a symmetrical antenna. A current mirror is used to bias the differential cascode stage. The two current sources (I_2 and I_3) are controlled by the mono-flop, which introduces the sleep mode, as discussed. The circuit performance in the differential mode is dis-

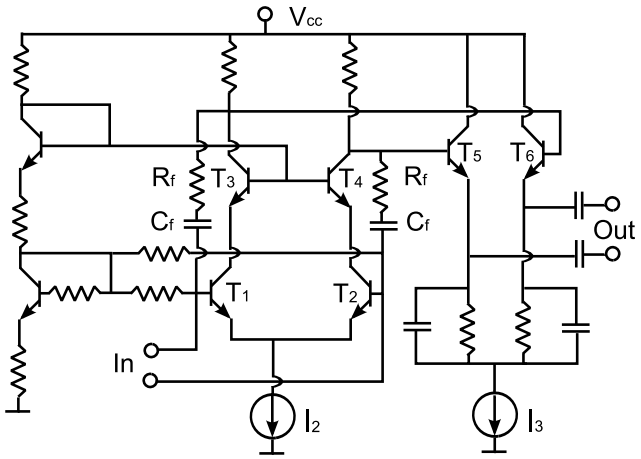

Fig. 3.35: Complete Schematic diagram of the fully differential UWB PA. Detailed circuit parameters are presented in Appendix A.4.

cussed here. As shown in Fig. 3.35, the emitter-coupled pair consists of two identical half circuits. Only the left half-circuit is discussed in the following. Transistor T_1, which is in common emitter configuration, and transistor T_3 in common base topology form the cascode configuration. The cascode topology is employed to reduce the Miller effect at the input of transistor T_1, which in turn increases the operating bandwidth. In this design, the key technique for achieving ultra-wide bandwidth is the resistive feedback (R_f), which is a widely-used approach to exchange gain for bandwidth [54, 55]. C_f is inserted for DC-decoupling. According to [54], the increment of the 3-dB bandwidth depends on the open-loop DC voltage gain A_0 of the cascode

structure (T_1 and T_3) and the feedback resistance R_f. If the 3-dB cut-off frequency of the open-loop cascode structure is ω_0, the closed-loop cut-off frequency can be expressed as

$$\omega_0' = \omega_0(1 + \frac{A_0 R_G}{R_G + R_f}) \tag{3.28}$$

where R_G is the source impedance and equals to 50 Ω. For a compromise between sufficient gain, achievable bandwidth and high linearity, the emitter size of T_1 is chosen to be 0.5μm x 30μm and the collector current is 10 mA. S-parameter simulation was performed to investigate the open-loop 3-dB bandwidth of the cascode structure. It shows a simulated open-loop 3-dB bandwidth of 3.8 GHz and a simulated open-loop DC voltage gain of 30 dB. If the wanted bandwidth is around 13 GHz which is larger than the bandwidth of the generated UWB impulses, the needed resistance value of R_f is 590 Ω, calculated from Eq. 3.28. Then, the closed-loop DC voltage gain can be calculated as

$$A_0' = -\frac{A_0 R_F}{R_F + (1 + A_0) R_G} = -8.4 = 18.5(dB) \tag{3.29}$$

It can be clearly seen that the shunt-shunt feedback does enhance the bandwidth, however, at the cost of gain reduction. Another important issue to be discussed here is matching. The input impedance is designed to be around 100 Ω since the LC oscillator needs such a load. This is easily realized by the resistive feedback. The in-body antennas have a low feed-point impedance, and hence the output buffers are designed for around 15 Ω output resistance.

For characterizing the PA performance, a differential PA with continuously supplied currents was fabricated and measured. Differential S-parameters were measured with the help of two identical passive microstrip line UWB baluns, whose influence was removed during the calibration process. The measured S-parameters can be seen in Fig. 3.36. The measured results show a maximum differential gain of 19 dB with a

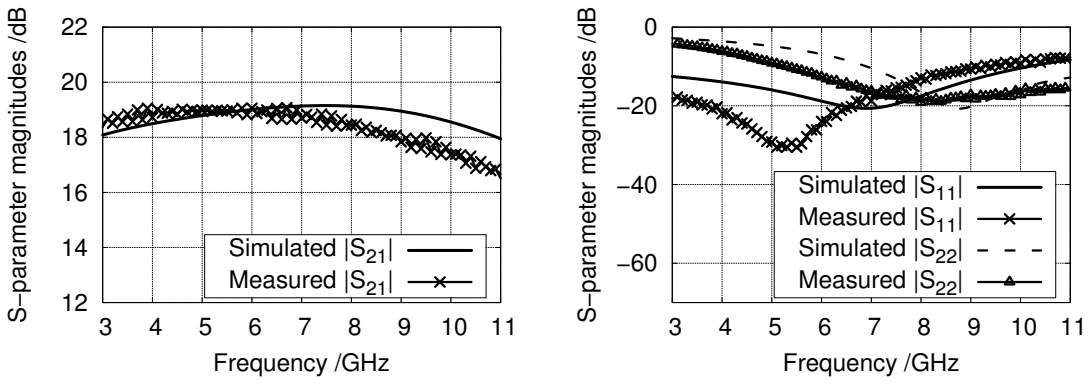

(a) Gain (b) Matching

Fig. 3.36: Comparison of the measured and simulated S-parameter magnitudes.

2 dB variation in the complete FCC allocated frequency range from 3.1 to 10.6 GHz.

The input return loss is better than 8.5 dB in the whole UWB frequency range. Because the output impedance is designed for an in-body symmetrical antenna which has a small feed point resistance around 15 Ω, S_{22} is normalized to 15 Ω and shown in Fig. 3.36 (b). The output return loss has a value better than 5 dB.

The linearity of this PA was characterized by OP_{1dB}. Fig. 3.37 depicts the measured result in the complete FCC allocated frequency band. It can be seen that this amplifier achieves more than 8.6 dBm output power at 1 dB compression points from 3-11 GHz, and the maximum achievable OP_{1dB} is 10.5 dBm at 5 GHz. The differential PA has a power consumption of 260 mW. However, when it operates together with the monoflop circuit, the PA operates in the sleep mode with almost no power consumption during most of a period. Therefore, the PA power consumption will be significantly reduced when the sleep mode is introduced, depending on the clock frequency. The micro-photograph of the complete transmitter can be seen in Fig. 3.38. This chip has a small size of 0.39 mm^2 including all bond pads.

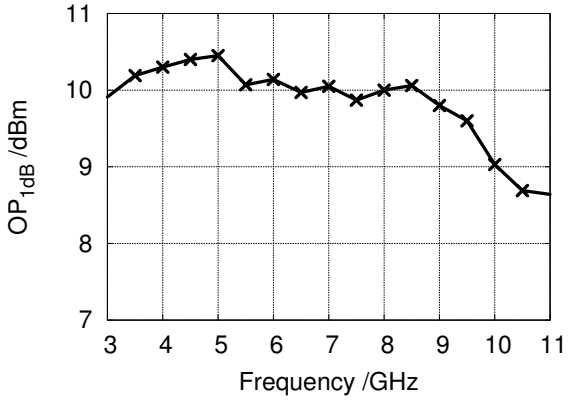

Fig. 3.37: The measured OP_{1dB} of the differential PA versus frequencies in the FCC allocated range.

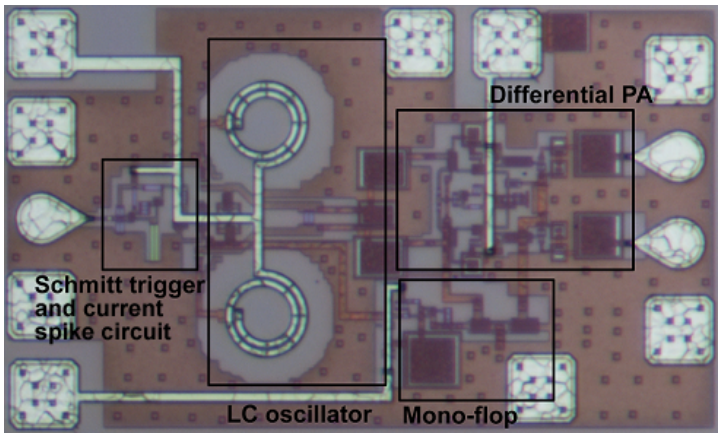

Fig. 3.38: Chip micro-photograph of the differential UWB transmitter.

3.6.4 Transmitter Characterization

The fabricated IC was first tested on wafer. A 200 MHz sinusoidal signal with a power level of -15 dBm is used as the input clock signal, and a real-time oscilloscope with a 13 GHz bandwidth was used to record the output waveforms. Fig. 3.39 (a) shows the recorded output impulse train. The measured impulses have a peak-peak amplitude of 1.8 V and an envelope width of 0.5 ns FWHM. The complete transmitter

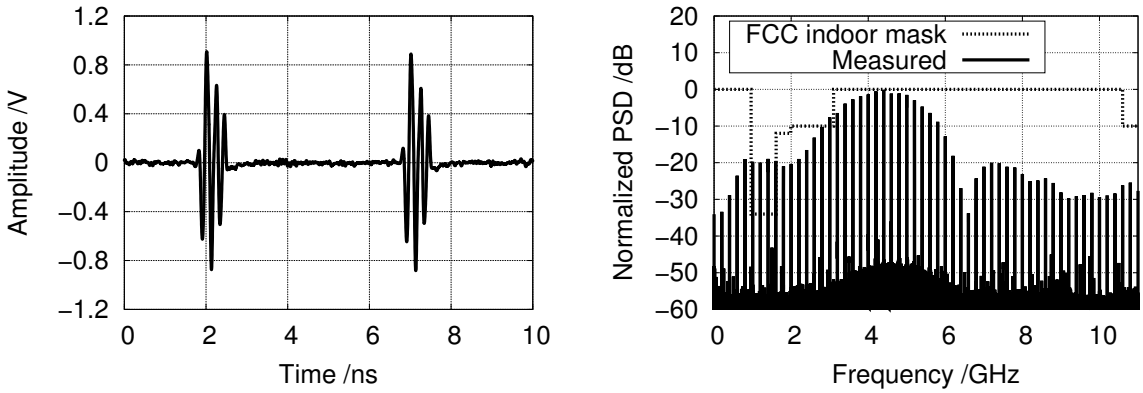

(a) (b)

Fig. 3.39: Measurement results of (a) the time-domain impulse sequence with a repetition rate of 200 MHz and (b) the corresponding spectrum information.

consumes a DC power of 30 mW at 200 MHz pulse rate due to the PA sleep mode. The maximum output pulse repetition rate can be into the GHz range. The corresponding normalized spectrum of the measured impulse train can be seen in Fig. 3.39 (b). It has a large 10-dB bandwidth of 3 GHz.

For realizing the complete beacon transmitter, the IC is mounted at the feed point of a compact dipole antenna. The antenna structure can be seen in Fig. 3.40 (a). It is realized on a Duroid 6010 substrate with a relative electric permittivity of 10.8. This implanted antenna is based on a dipole structure with an elliptical shape, which increases the operating bandwidth. Miniaturization of the antenna is achieved owing to the high permittivity environment. A recess is designed to allow the insertion of the transmitter IC, which decreases the length of bond wires. A detailed explanation of the antenna can be found in [56]. The photograph of the complete UWB transmitter is illustrated in Fig. 3.40 (b). The antenna substrate and the IC are sealed by a layer of water-resistive glue, which allows the transmitter to be placed in a tissue-mimicking fluid. Because of the compact antenna, the complete transmitter has a size of 9 mm x 20 mm. This small size makes the transmitter suitable for in-body applications. Detailed information on the antenna substrate is depicted in Fig. 3.40 (c). As can be seen, the IC is mounted chip-on-board at the feedpoint of the symmetric antenna. Fig. 3.40 (d) shows the microphotograph of the IC packaged using a wire bonding approach. Three planar SMD chip capacitors are placed in close proximity to the DC ports of the transmitter IC to compensate for the bond wire inductance.

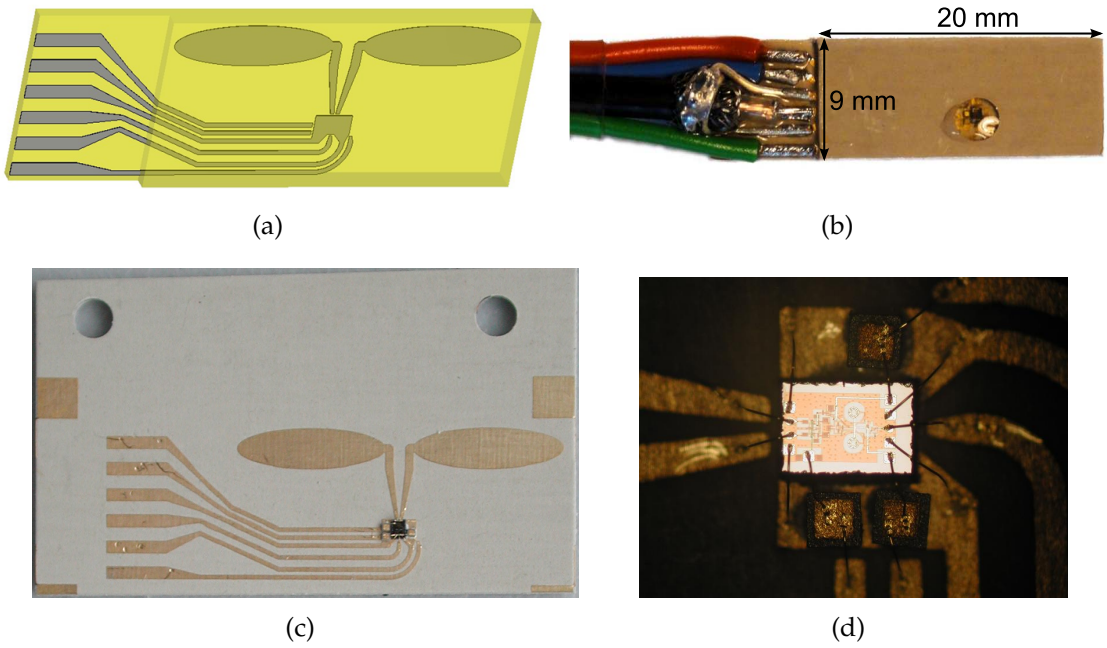

Fig. 3.40: (a) Picture of the antenna structure, (b) photograph of the complete UWB transmitter with the IC sealed by water-resistive glue, (c) photograph of the antenna substrate and (d) microphotograph of the transmitter IC placed chip-on-board on the antenna substrate.

To characterize the packaged transmitter, a medium with similar dielectric properties as human tissue is needed. Therefore, it is worth to mention the properties of human tissues.

Dielectric properties of human tissues

The properties of biological tissues have been investigated in [57]. The relative electrical permittivity and attenuation constants of various tissue components are different, which is due to the different levels of water content. Fig. 3.41 (a) plots the relative permittivity of human skin, fat, muscle and blood from 3-11 GHz. The corresponding attenuation constants are shown in 3.41 (b). As can be seen, all these tissues have a strongly dispersive behaviour. E.g., the relative permittivity of the human skin varies from 29 to 38, and the attenuation constant from 5 dB/cm to 25 dB/cm in the UWB allocated frequency range.

Tissue replacement liquid

The commercially available tissue replacement medium used in this thesis is HSL 5800, which is a mixture of water, oil, and salt [58]. The relative permittivity and the attenuation constant of this tissue-mimicking liquid are shown in Fig. 3.42. As can be seen, both the relative permittivity and the attenuation constant have a linear frequency response. A comparison of HSL 5800 and skin tissue is illustrated in Fig. 3.42, which shows good agreement. Therefore, this medium HSL 5800 can be used as a replacement for the human tissue during the measurements.

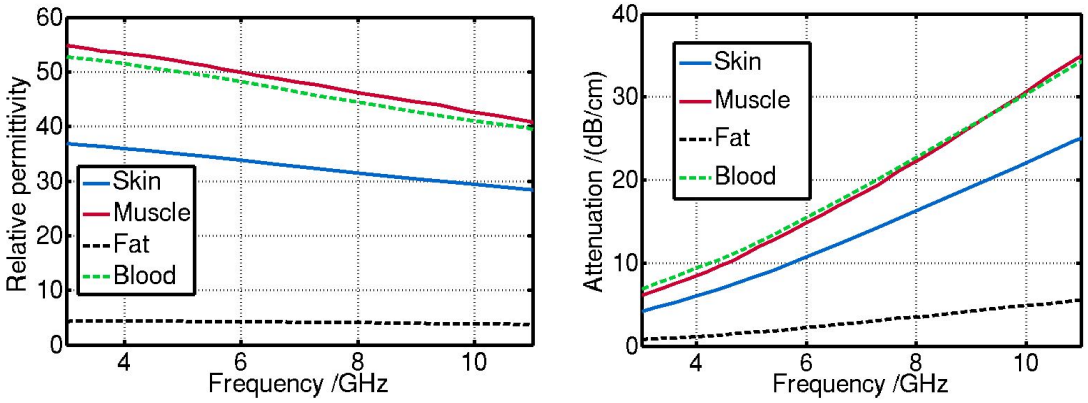

(a) (b)

Fig. 3.41: The relative permittivity (a) and the attenuation constants (b) of the various human tissues. All of them show a linear frequency behaviour.

The set-up for characterizing the packaged beacon transmitter immersed in the tissue-mimicking liquid HSL 5800 is illustrated in Fig. 3.43. Another implanted antenna is employed as the receiving antenna, which is a UWB triplate-fed slot antenna optimized for radiation in human tissue [59]. This receiving antenna can be placed in the tissue-mimicking liquid and has a mean gain of 3.8 dBi from 3.1-10.6 GHz. A stepper motor on top of the liquid tank can precisely control the distance between the transmitter and the receiver antenna, and this distance is 3 cm in this measurement. The received waveforms were recorded by a real time oscilloscope.

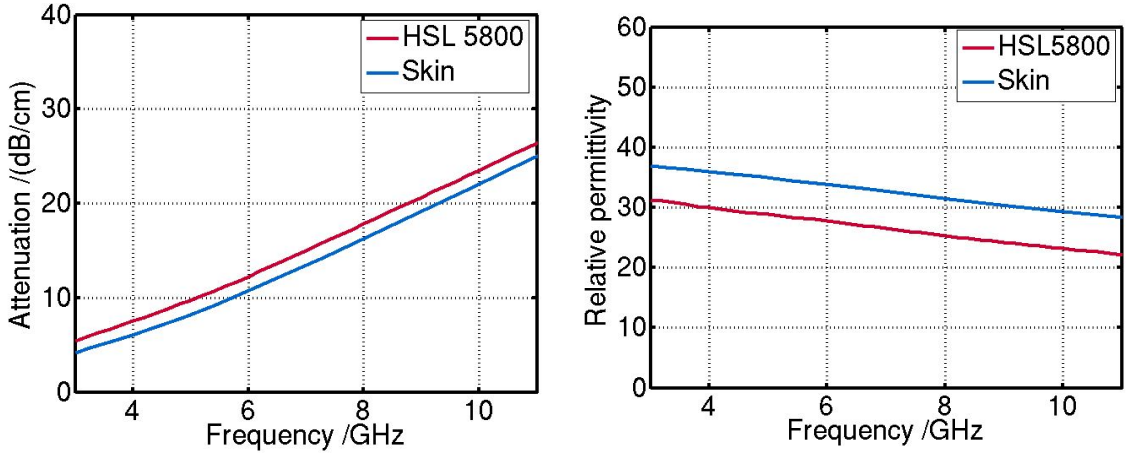

(a) (b)

Fig. 3.42: The relative permittivity (a) and the attenuation constant (b) of the tissue-mimicking liquid HSL 5800. It is a suitable replacement medium for the human skin in the test environment.

This transmission measurement in the liquid was performed in the time domain. The received impulse waveform can be seen in Fig. 3.44. The liquid introduces a

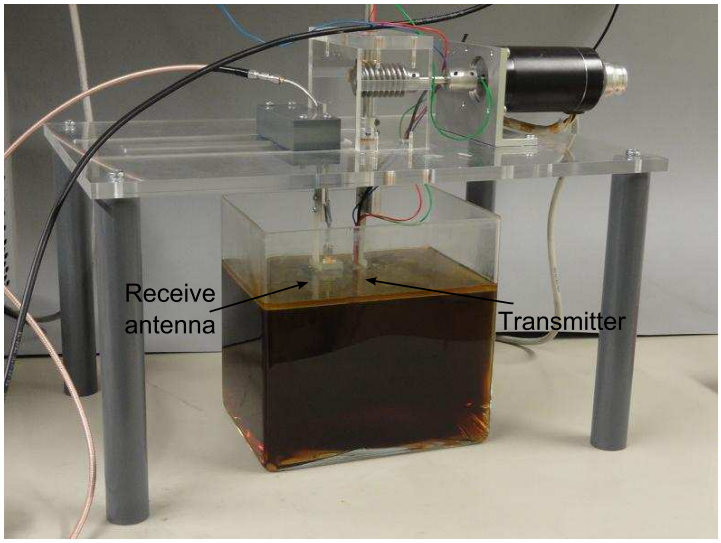

Fig. 3.43: Measurement set-up when characterizing the UWB beacon transmitter. Both the transmitter and the receiver antenna are immersed into the liquid.

large attenuation which makes the amplitude of the received waveform extremely small. Moreover, it clearly indicates that the received impulse shape is significantly broadened. This is mainly due to the increased losses for higher frequencies in the HSL 5800. However, the IR-UWB impulse transmission in this liquid is still well achieved.

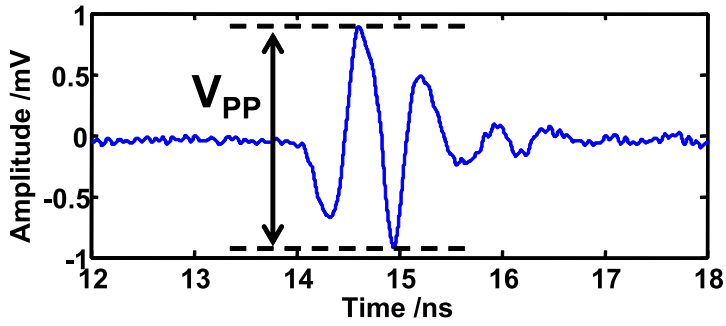

Fig. 3.44: The received impulse waveform with the receive antenna placed with a distance of 3 cm from the transmitter.

Furthermore, the radiation pattern of the transmitter was determined. The distance of the two antennas is still set to 3 cm. The transmitter antenna is rotated and the received impulses are recorded by the real time oscilloscope. The rotation is realized by the stepper motor. Fig. 3.45 illustrates the information of the transmitter rotation. As can be seen, the transmitter is rotated in both E-plane and H-plane. The amplitude of the received impulse at different radiation angles is recorded. Then, the relative received amplitudes versus the rotation angles both in E-pane and H-plane are plotted, as shown in Fig. 3.46.

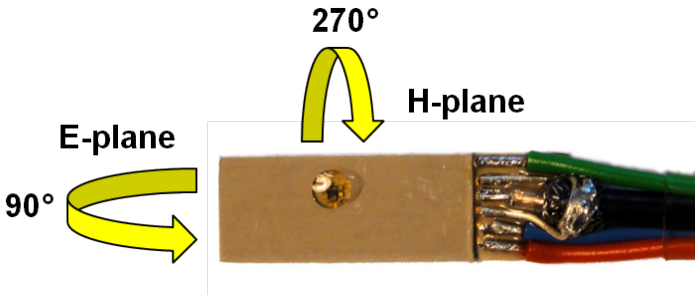

Fig. 3.45: The rotation details of the UWB transmitter for radiation pattern measurement.

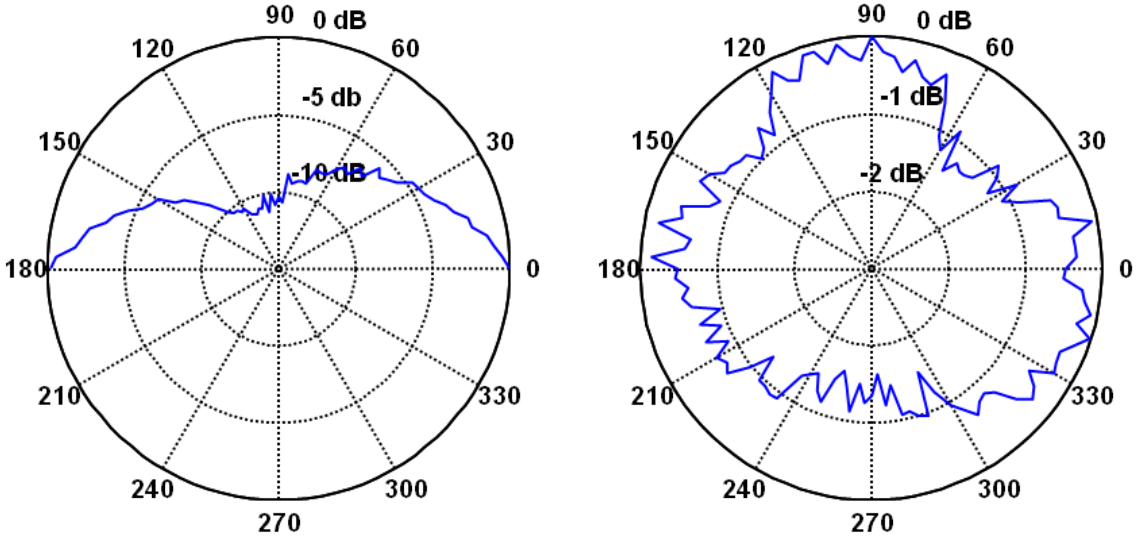

Fig. 3.46: Relative amplitude of the received impulse when rotating the transmitter in (a) E-plane and (b) H-plane.

Chapter 4

Differential IR-UWB Receiver Design

In this chapter different types of receiver frontends are described, which make use of the FCC indoor mask. First a brief review of two widely used receiver topologies for the IR-UWB applications is presented. Then the individual building blocks of the receivers are discussed in detail. Finally, two kinds of receiver frontends are designed and characterized.

4.1 Basic Receiver Concepts

In general, there are two widely used IR-UWB receiver structures: correlation receivers and energy detection receivers [60–62]. The correlation receivers are insensitive to interference, but at the cost of requiring precise synchronization. In contrast, the energy detection receivers are conceptionally simple and do not require synchronization, but are not robust to in-band interferers. This section presents a brief discussion on these two receiver structures.

4.1.1 Correlation Detection

The architecture of a correlation-based receiver is shown in Fig. 4.1. The receiver consists of a receiving antenna, a UWB LNA, a template impulse generator which generates the same waveforms as the transmitted impulses, a UWB multiplier and an integrator circuit. The correlation operation is performed by feeding the received UWB impulses, amplified by a wideband differential LNA, and the template impulses generated on chip into a UWB multiplier. The multiplier output is a measure indicating the alignment of the template impulse with the received impulse in time and shape. In general, the template impulse generator is the same as the impulse generator on the transmitter side. Correspondingly, the received impulse waveforms, which include antenna and transmission media influences may not exactly match the template waveforms. However, this difference is accepted in this thesis in order to keep

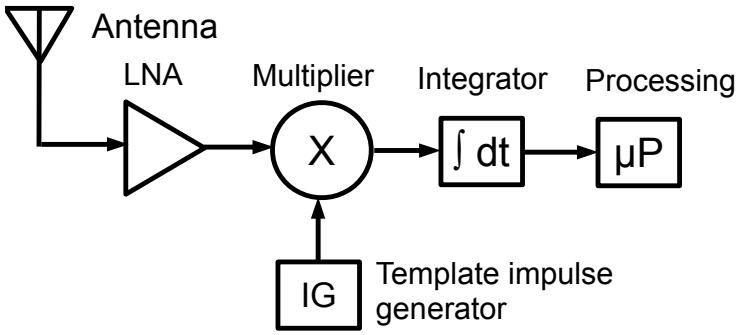

Fig. 4.1: Block diagram of a typical correlation detection receiver.

the architecture simple. Indeed, a cross-correlation is performed in this simple receiver. Mathematically, a cross-correlation function (CCF) is defined to express the influence of the time shift τ between the two impulses. The function of the CCF can be expressed as

$$CCF(\tau) = \int_{-\infty}^{+\infty} R^*(t)T(t+\tau)dt \tag{4.1}$$

where R(t) and T(t) are the received impulse and the template impulse, respectively. When R(t) and T(t) are not complex valued functions, the complex conjugate of R(t) can be omitted. The CCF achieves its maximum value when the two impulses are exactly time-aligned with each other. The cross-correlation receiver is a classical matched filter system and provides the best performance in terms of signal to noise ratio when R(t) and T(t) are matched in time [62]. It presents a significant resistance to in-band interferences.

Previous publications have investigated the influence of time shifts between the received and template impulses. E.g., [27] plots the correlation function of the fifth derivative Gaussian pulses. It clearly indicates that a slight misalignment between the two impulses in the range of picoseconds in the time domain results in a large decrease on the correlation function. So, this correlation-based receiver requires extremely accurate timing synchronization. This synchronization issue may largely increase the receiver complexity for communication applications. However, this problem can be easily solved when this kind of receiver is employed for radar and sensing applications, because the transmitter and the receiver in such applications are always co-located and well synchronized with a common reference.

4.1.2 Energy Detection

As can be seen in Fig. 4.2, an energy detection receiver consists of a receiving antenna, a UWB LNA, a UWB squaring circuit and an integrator. This receiver detects the energy of the received UWB impulses rather than the actual waveforms, reducing the circuit complexity. Compared to the correlation receiver, it eliminates the need for

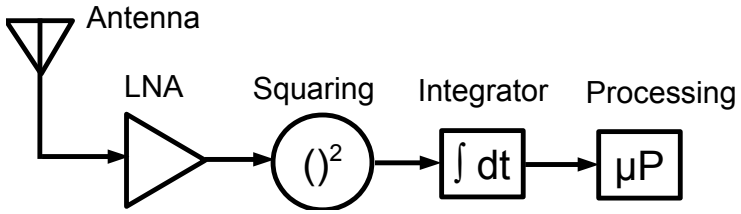

Fig. 4.2: Block diagram of a non-coherent energy detection receiver.

precise synchronization which further makes the receiver architecture simpler and leads to lower power consumption. These properties make this receiver extremely suitable for OOK communication and localizations based on a TDoA approach [63–65]. On the downside, the energy detection receiver is not rejecting noise and in-band interferences.

As a conclusion, to assemble the frontend circuits for these two kinds of receivers, the following key components have to be developed:

- a fully differential low noise amplifier,
- a four-quadrant true multiplier,
- a template impulse generator,
- a squaring circuit,
- and a low-pass filter performing integration.

These components will be discussed in detail in the following sections.

4.2 Fully Differential Low Noise Amplifier

This section discusses the design of a fully differential LNA, which is used in both the correlation and the energy detection receivers. First, the circuit topology and approach to realize a low noise figure are presented. Then, the fabricated IC is characterized on wafer. Both small-signal and large-signal performance of the UWB LNA is measured.

4.2.1 Circuit Design

The UWB LNA should offer low noise figure as well as high and flat gain over the complete UWB frequency band, since it is the first stage of a receiver frontend. Another important consideration is that the group delay variation, which determines the impulse shape distortion in the time-domain, should be small. Moreover, a sufficient

linearity and low power consumption have to be targeted. So far, many techniques have been reported to realize the aforementioned goals. [66–68] employ distributed amplifiers to cover the full FCC allocated band. The distributed amplifier is a well-known wideband topology operating from DC to extremely high frequencies with a constant group delay. However, these circuits suffer from high power consumption, inferior noise behaviour and a large chip size. Another example shown in [69] uses broadband reactive matching to achieve wideband amplification. The proposed circuit shows a high gain and a low power consumption within the ECC allocated frequency range. However, the input matching network introduces significant losses and a large group delay variation. Furthermore, the on-chip inductors occupy a large area. Another widely used technique is the negative feedback amplifier [70–72]. The single-ended UWB LNA in [70] shows a constant group velocity, extremely broadband gain and matching and a low noise figure with a highly compact chip size, although the negative feedback does introduce additional noise and negatively influences the power gain.

The differential LNA designed in this thesis follows the method in [70]. It is based on resistive feedback and avoids any spiral inductors. Fig. 4.3 shows the complete schematic of the differential UWB LNA. The LNA consists of an emitter-coupled pair with cascoded devices, followed by two symmetric emitter follower buffers. The

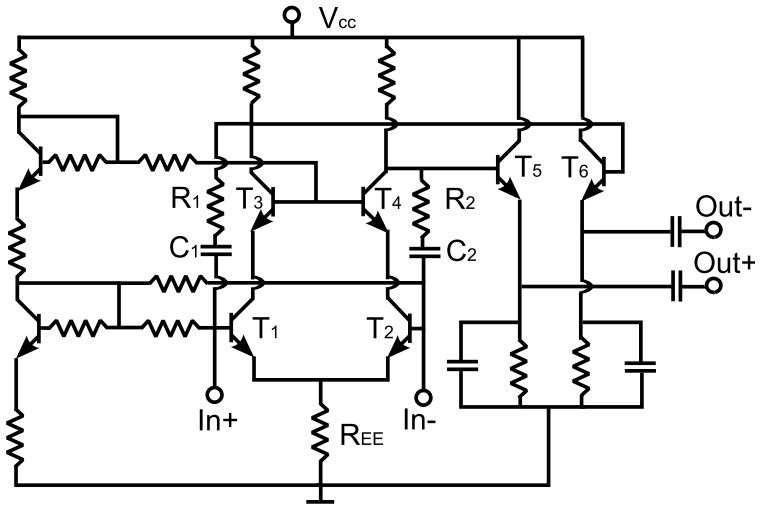

Fig. 4.3: Schematic of the proposed fully differential LNA, it is based on a cascoded emitter-coupled pair with shunt-shunt feedback. The buffer stage is employed for inter-stage matching.

cascode stages are DC biased through a current mirror. It is designed to be fully differential as the LNA will be directly connected to a symmetrical antenna, and shall feed a Gilbert cell type multiplier, eliminating an unbal circuit. By placing identical transistors and passive components in the two branches, the emitter-coupled pair is fully symmetric. The resistor R_{EE} is used as the tail current source and provides common-mode rejection.

The differential LNA has a similar circuit topology as the UWB PA shown in Fig.

3.35. The cascode configuration is employed to reduce the Miller effect at the input transistors, thus increasing the bandwidth. The shunt-shunt feedback components (R_1, C_1 and R_2, C_2) further broaden the operating bandwidth and improve the input matching simultaneously. The two emitter follower stages are placed as impedance converters, which offer high input impedance for the cascode stage and low output impedance for the following stages. The functionality of the emitter degeneration capacitors in the buffer stage is to increase the operating bandwidth. The linearity of this LNA strongly depends on the current of the buffer stages. As a compromise between total power consumption and the linearity, each emitter-follower draws a DC current of 5.8 mA.

An important parameter which needs to be further considered is the noise figure. As discussed in Sec. 3.6.3, the wide bandwidth operation is achieved through resistive feedback. However, one drawback of the resistive feedback is the increase of noise figure. According to [73], the noise figure F of an arbitrary two-port can be expressed as

$$F = F_{min} + \frac{4r_n|\Gamma_S - \Gamma_{S,opt}|^2}{(1-|\Gamma_S|^2)|1+\Gamma_{S,opt}|^2} \tag{4.2}$$

where F_{min} is the minimum achievable noise figure, Γ_S means the source reflection coefficient, $\Gamma_{S,opt}$ corresponds to the noise-optimum source reflection coefficient and r_n is the normalized value of the equivalent noise resistance R_n with

$$r_n = \frac{R_n}{Z_0} \tag{4.3}$$

where Z_0 is the reference impedance and equals to 100 Ω here because of the differential design. Here the source impedance is 100 Ω in differential circuit when considering noise figures, so $|\Gamma_S|$=0. Eq. 4.2 can be modified as

$$F = F_{min} + \frac{4r_n|\Gamma_{S,opt}|^2}{|1+\Gamma_{S,opt}|^2} \tag{4.4}$$

Eq. 4.4 clearly shows that the noise figure strongly depends on F_{min}, $\Gamma_{S,opt}$ and r_n. According to [74], small values of $|\Gamma_{S,opt}|$ and r_n can be achieved by a large transistor size. In this design, the transistors T_1, T_2, T_3 and T_4 have the same emitter dimension of 0.5μm x 25μm and the same collector current of 5 mA.

The resistive feedback network increases F_{min} and r_n because of the resistance thermal noise. Here several simulations were performed to investigate this influence. First, the simulated results of F_{min} are plotted in Fig. 4.4 (a). As can be seen, the feedback network introduces an increment of 0.6 dB to F_{min}. However, the main noise contributor to the overall circuit comes from the input transistors. Then, the influence of r_n was simulated. The results are illustrated in Fig.4.4 (b). As can be seen, r_n does increase with applying the feedback network. However, it still has a small

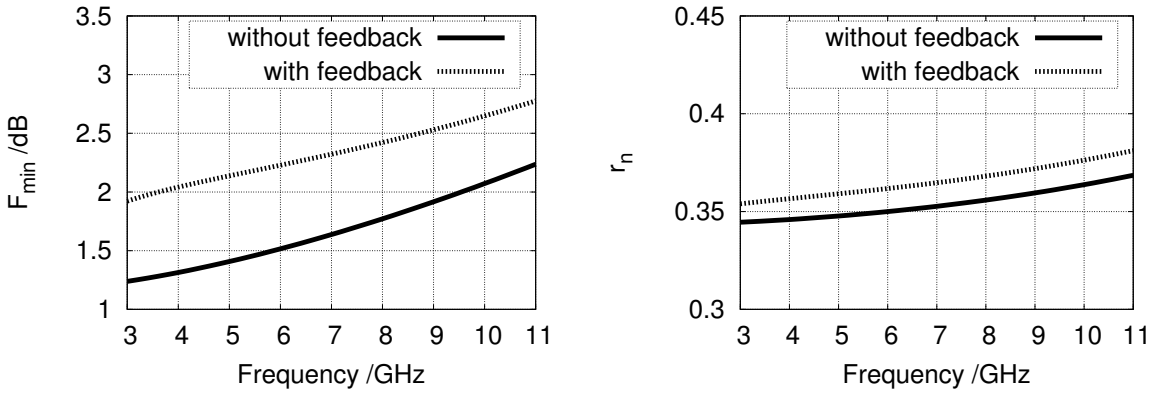

(a) F_{min} (b) r_n

Fig. 4.4: Simulated results of (a) F_{min} and (b) r_n, without and with feedback.

value, this is mainly due to the careful selection of input transistor size and adjustment of bias points. Furthermore, Fig. 4.5 (a) depicts the influence of the resistive feedback on $\Gamma_{S,opt}$. It shows that the track of $\Gamma_{S,opt}$ moves towards the centre of the Smith chart, which is beneficial to offset the increase in F_{min} and r_n. At last, the influence of the feedback network on the differential noise figure of the LNA is shown in Fig. 4.5 (b). Although the feedback does contribute noise, the noise figure still has a small value around 3 dB even at 11 GHz, showing an outstanding noise performance while achieving wide bandwidth.

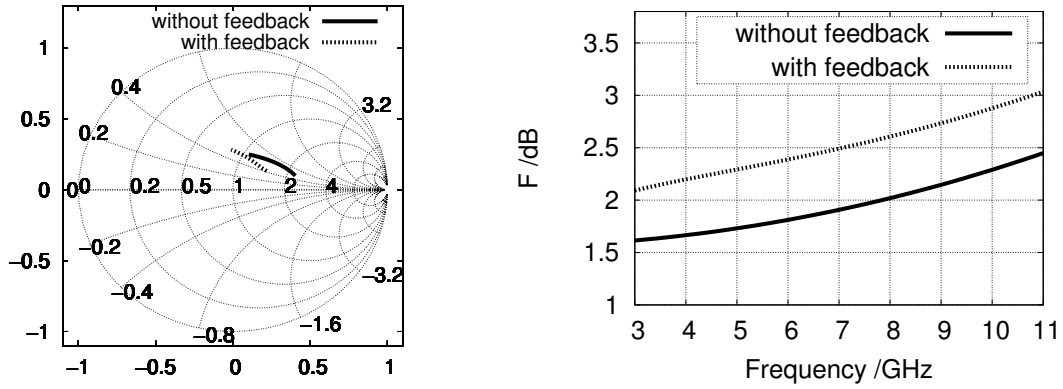

(a) $\Gamma_{S,opt}$ (b) Noise figure

Fig. 4.5: Comparison of (a) $\Gamma_{S,opt}$ and (b) differential noise figures of the LNA without and with feedback.

Fig. 4.6 shows the microphotograph of the fabricated LNA. Through a suitable arrangement of all the components and increasing the length of the DC feed lines to obtain the same number of crossings between each signal path and DC path, this layout shows a high symmetry, which is extremely helpful to maintain the balancing advantages of the fully differential configuration. Avoiding large on-chip inductors,

this chip has an extremely small area of 0.37 x 0.38 mm^2. It should be also noticed that the lowest available metal layer was placed below the large-sized bonding pads to provide a ground shield and avoid substrate noise pick-up.

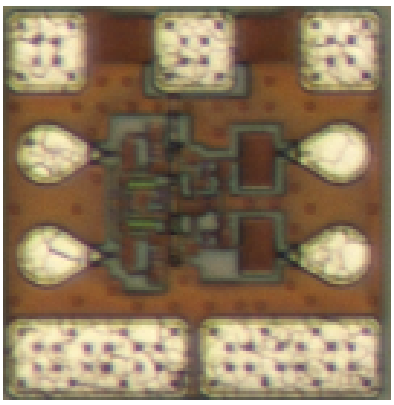

Fig. 4.6: Microphotograph of the differential UWB LNA. It has an extremely small area of 0.14 mm^2.

4.2.2 Measured Results

The on-wafer measurements were done using two RF GSSG probes with a 100 μm pitch. Two identical passive microstrip line UWB baluns were used for differential S-parameter measurements. The influence of the two passive baluns was removed through the calibration process. The S-parameter measurement was performed from 3 to 11 GHz because the UWB baluns operate in this frequency range. The differential LNA shows a maximum gain of 19.9 dB with a 1.8 dB variation in the complete UWB rang from 3.1 to 10.6 GHz, as shown in Fig. 4.7 (a). The non-ideal performance of the UWB balun generates some ripples on the measured curves. The measured input return loss has a value better than 7 dB, and the output return loss is better than 6 dB in the complete FCC allocated range, as depicted in Fig. 4.7 (b). As can be seen, all the measured S-parameter magnitudes are quite close to the simulated ones.

Another important parameter for IR-UWB LNAs is the group delay variation. Because the proposed LNA relies on negative feedback for matching, a small group delay variation within the entire band has been achieved. As plotted in Fig. 4.8 (a), the measured group delay variation is smaller than 15 ps over the 3.1-10.6 GHz range. To figure out the 3-dB bandwidth of this differential LNA, a single-ended measurement from port in+ to out- was performed with the other two ports terminated by 50 Ω RF terminations. For comparison, the differential circuit was then re-simulated for this particular single-ended configuration. The comparison of the simulated and measured single-ended gain is shown in Fig. 4.8 (b). It is clear that both the measured single-ended and differential gains are extremely close to the simulated ones, as illustrated in Fig. 4.7 (a) and Fig. 4.8 (b). So, the 3-dB bandwidth of this circuit can be concluded to be from 0.6 to 12.6 GHz.

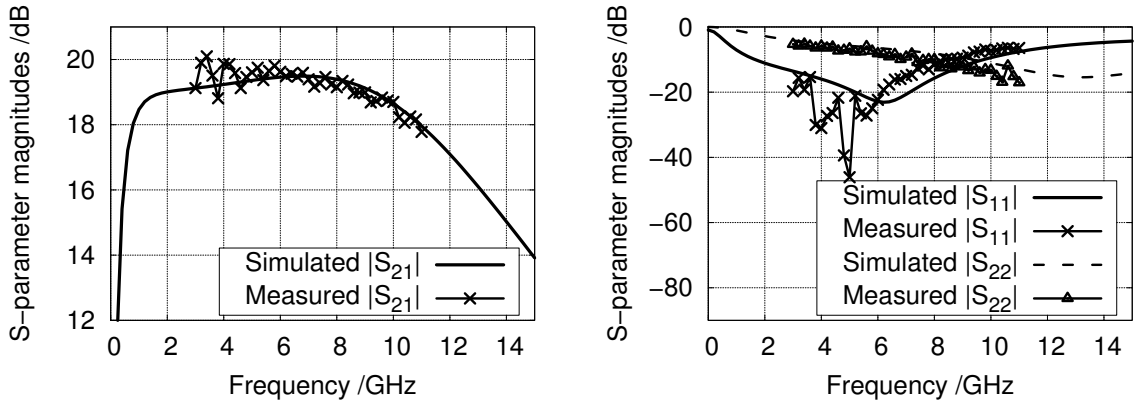

(a) Gain (b) Matching

Fig. 4.7: Comparison of the measured and simulated S-parameter magnitudes of the differential LNA.

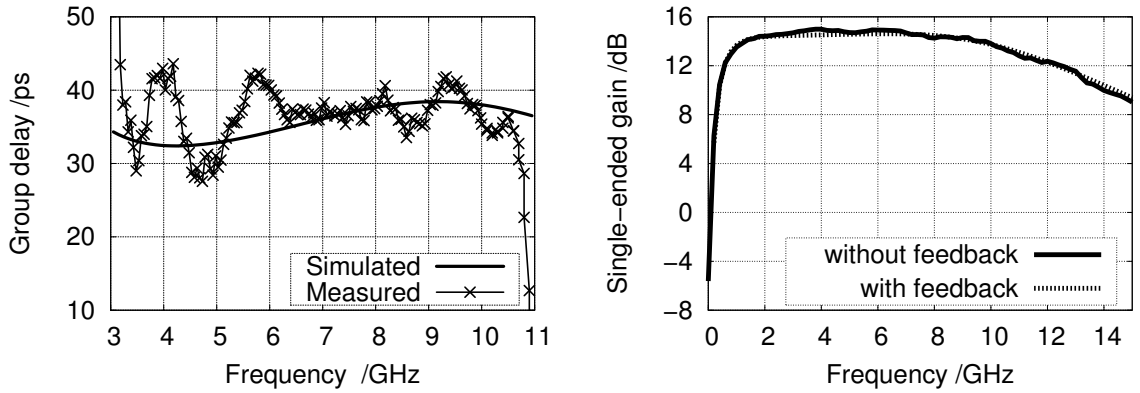

(a) Group delay (b) Single-ended gain

Fig. 4.8: Measured and simulated results of (a) the group delay and (b) the single-ended gain of the fabricated UWB LNA.

In terms of the noise figure measurement, the method proposed in [75] is employed to extract the differential noise figure from single-ended measurements. First, the single-ended noise figure (F_{31}) (port in- and port out+ are terminated by 50 Ω) was performed. Then, the transducer gains from port out- to in+ (G_{31}) and from port out+ to in+ (G_{32}) were measured. Due to the perfect symmetry of this circuit, the differential noise figure can be expressed as

$$F_{diff} = 1 + \frac{1}{G_{31} + G_{32}}(F_{31}G_{31} - G_{31} - G_{32}). \tag{4.5}$$

The information of all the noise figures can be seen in Fig. 4.9 (a). The measured single-ended and extracted differential noise figures show excellent agreement with the simulated ones. The differential LNA has a differential noise figure varying from

2.1 to 2.9 dB across the whole FCC allocated UWB band. Another important param-

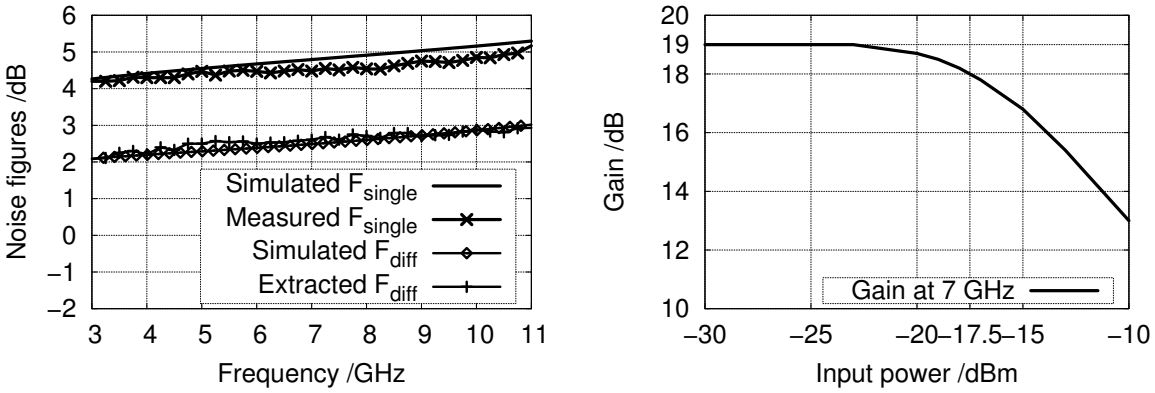

(a) Noise figures (b) Linearity

Fig. 4.9: (a) The measured single-ended and extracted differential noise figures in comparison with the simulated ones and (b) the measured LNA gain depending on input power at 7 GHz.

eter is the 1-dB compression point, which indicates the linearity performance of this amplifier. As shown in Fig. 4.9 (b), the measured input 1-dB compression point at 7 GHz is -17.5 dBm and the output 1-dB compression point is 1.5 dBm at this frequency. The LNA draws a DC current of 22 mA from a 3.5 V supply. As a conclusion, this LNA shows a great overall performance while occupying an extremely small area. Detailed circuit parameters of the LNA are given in Appendix A.5.

4.3 Correlation Detection Receiver

As discussed in Sec. 4.1.1, the multiplier-based correlation detection compares the received UWB impulse with a delayed replica and indicates the similarity between the two waveforms. In this work, the correlation is performed in the analog domain which leads to an energy efficient solution by omitting the power-hungry wide-bandwidth analog-to-digital converters (ADCs) and allows to handle very high-speed signals. In terms of hardware implementation, a four quadrant analog multiplier based on a Gilbert cell is used to perform the wideband multiplication.

4.3.1 Correlator based on analog correlation

The complete schematic of the wideband analog correlator can be seen in Fig. 4.10. The core of the correlator is a Gilbert cell multiplier, which comprises two differential stages in parallel with cross-coupled outputs. The multiplier is complemented with two low-pass filters and a differential output buffer.

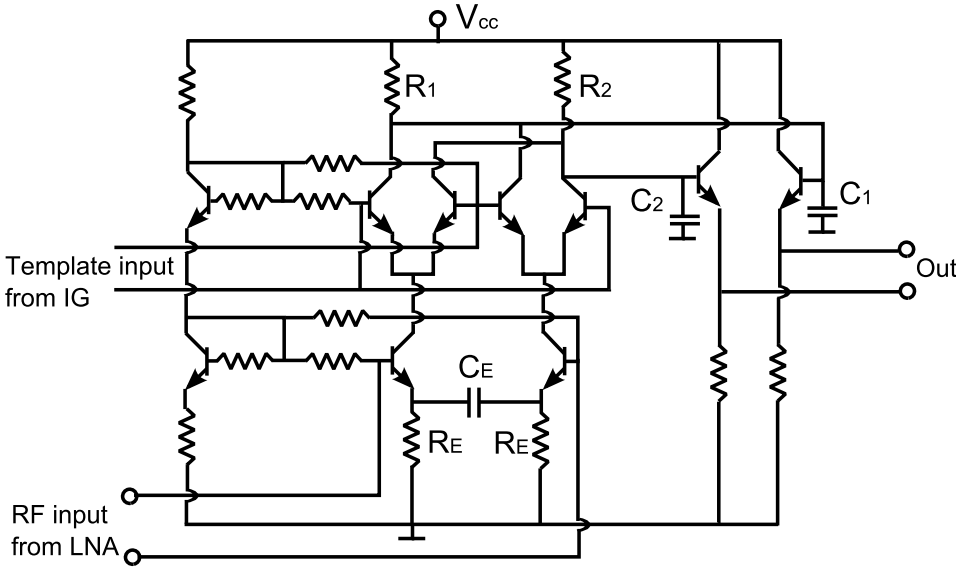

Fig. 4.10: Complete schematic of the UWB correlator with a real-time multiplier, low-pass filters and a differential buffer. Detailed circuit parameters are presented in Appendix A.6.

The Gilbert cell performs as a wideband, four-quadrant true multiplication with proper template impulse amplitude applied to the quad. A stacked current mirror is employed for biasing the Gilbert cell. A capacitively shunted resistive emitter degeneration, formed by C_E with R_E, compensates the gain roll-off at high frequencies and in turn results in a necessary gain flatness over the whole FCC allocated UWB frequency band. The load resistors (R_1, R_2) of the Gilbert cell and the shunt capacitors (C_1, C_2) of the buffers form two low-pass filters with 800 MHz 3-dB bandwidth. The functionality of the filters is to detect the envelope of the multiplied signals.

Operation with sinusoidal inputs

In order to evaluate the conversion gain and the linearity of the UWB correlator, two sinusoidal sources were employed at the template and the RF input ports. The simulation configuration can be seen in Fig. 4.11 (a). The correlator circuit was simulated for down-conversion to a fixed output intermediate frequency (IF) of 100 MHz while sweeping RF frequencies from 3-11 GHz.

Fig. 4.12 (a) shows the simulated differential conversion gain (P_{out}-P_{RF}) versus input RF frequencies. The RF power has a fixed value of -10 dBm, while the sinusoidal power applied to the template input varies from -30 dBm to -10 dBm. The simulation result indicates that 3-dB cut-off frequencies well exceed the FCC allocated UWB range. As a conclusion, the correlator circuit is suitable for UWB applications. Linearity of the RF port was simulated by the input 1-dB compression point (IP_{1dB}) at a fixed IF of 100 MHz with the template port having a fixed power of -10 dBm. The simulated IP_{1dB} versus input RF frequencies can be seen in Fig. 4.12 (b). The circuit shows a good linearity with IP_{1dB} larger than 0 dBm within the complete FCC allocated frequency range.

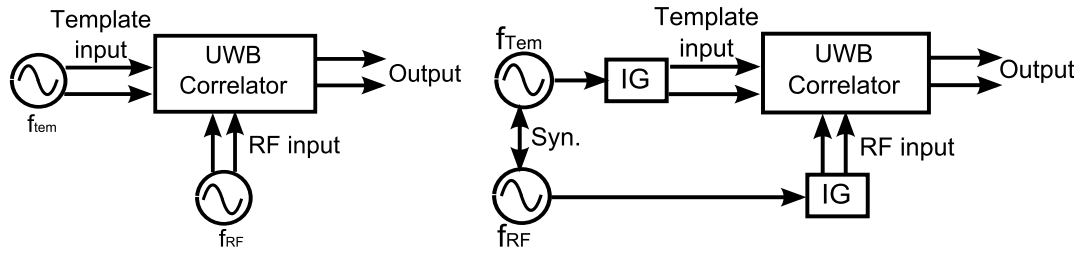

Fig. 4.11: Simulation configurations for characterizing the correlation circuit with (a) sinusoidal signals as inputs and (b) UWB impulses as inputs.

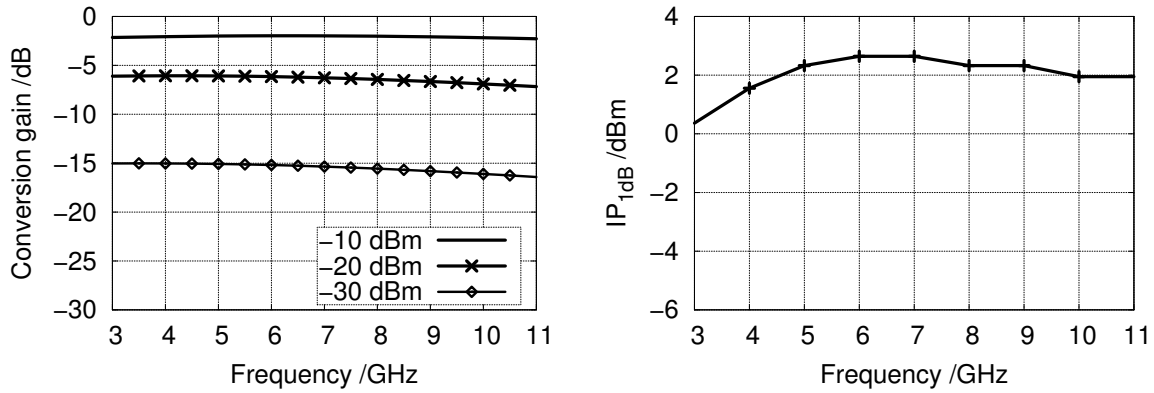

Fig. 4.12: Simulation results of (a) the conversion gain when down-conversion to a fixed IF of 100 MHz with different input power levels at template port and (b) IP_{1dB} versus frequencies.

Operation with UWB impulses

The multiplication performance in the time domain was evaluated by connecting two UWB impulse generators shown in Fig. 3.6 to the input ports of this correlator. The simulation set-up is illustrated in Fig. 4.11 (b). The clocks of the two impulse generators (f_{RF}, f_{Tem}) were well synchronized and set to a common frequency of 200 MHz. This strategy makes sure that the two branches of the generated impulses reach the correlator at the same time. The simulated result at the output of the Gilbert cell can be seen in Fig. 4.13 (a). It shows a perfect real-time multiplication. Fig. 4.13 (b) depicts the simulated output transients from the correlator circuit. As can be seen, the envelope of the multiplied signal shown in Fig. 4.13 (a) is clearly detected by the low-pass filter.

Another simulation was done to demonstrate the correlation performance of the proposed system. To get different time shifts τ between the two impulses, the RF clock was swept in discrete phase steps. The correlation function versus τ can be calculated by mathematically integrating over the correlator output signal for every phase

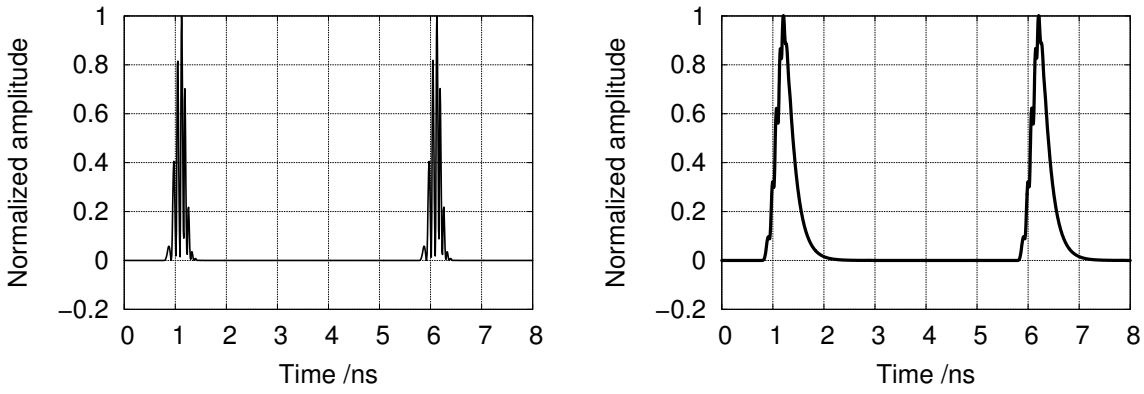

(a) (b)

Fig. 4.13: Simulated output transients of (a) the Gilbert cell and (b) the correlator, at feeding two time-aligned impulse sequences with a repetition rate of 200 MHz to the input ports of the correlator.

step. The simulated result of the normalized correlation function is illustrated in Fig. 4.14 (a). A good symmetry has been maintained. Fig. 4.14 (b) focuses on the vicinity of the correlation maximum. As can be seen, the correlator output significantly depends on the time alignment. A slight misalignment of 20 ps results in a decrease of 30% from the correlation maximum.

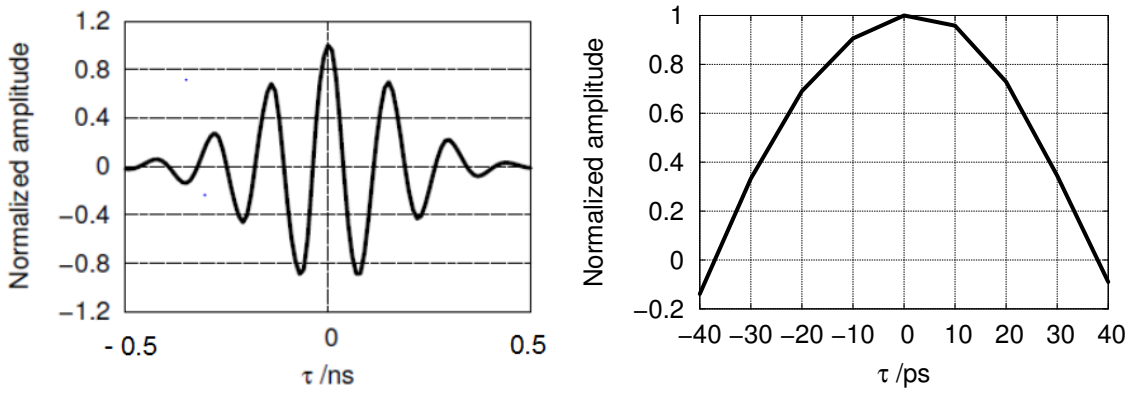

(a) (b)

Fig. 4.14: (a) Simulated normalized correlation of two UWB impulses generated by the impulse generation circuit shown in Fig. 3.6 and (b) details in the vicinity of the correlation maximum.

4.3.2 Fully Monolithic Correlation Receiver

Fig. 4.15 shows the block diagram of the fully monolithic correlation receiver. It

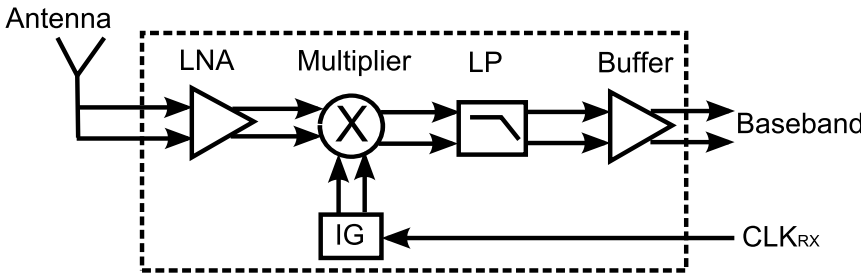

Fig. 4.15: Complete block digram of the monolithic correlation receiver frontend.

consists of a fully differential wideband LNA, a template impulse generator and a multiplier-based correlator. The received waveforms from the antenna are first amplified by the LNA which is presented in Sec. 4.2. The correlation reception is realized by feeding the amplified waveforms and the impulses generated on chip by the template impulse generator into the correlator circuit explained in Sec. 4.3.1, which includes an analog multiplier, low-pass filters and buffers. As discussed in Sec. 4.1.1, the template impulse generator is the same as the generator on the transmitter side, the impulse distortions due to antenna influences and channel response are not considered in order to keep the receiver structure simple.

The microphotograph of the fabricated differential receiver IC is shown in Fig. 4.16. It has a size of 0.57 x 0.89 mm^2 and consumes a total DC power of 130 mW. The

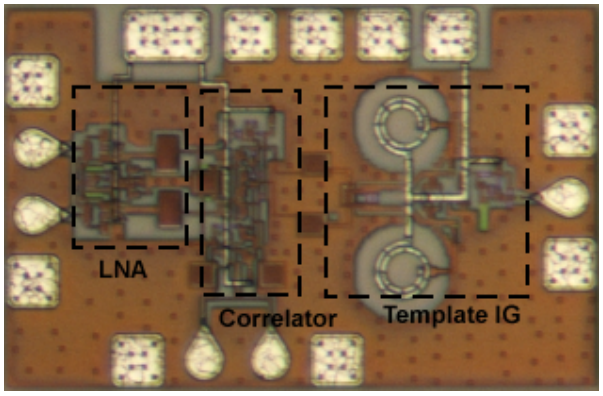

Fig. 4.16: Chip micrograph of the differential monolithic correlation receiver frontend. The fully integrated frontend circuit has a small area of 0.51 mm^2.

power consumption is significantly reduced compared to the single-ended version published earlier [29] due to the elimination of active baluns and the use of a highly efficient impulse generator concept.

The fabricated receiver frontend IC was characterized on wafer. Fig. 4.17 shows the experiment set-up. The UWB impulse generator depicted in Fig. 3.9 was employed to generate transmitted impulse train. Two 20-dB attenuators were placed between the impulse generator and the receive frontend IC. The two clock signals (CLK_{TX} for the impulse generator and CLK_{RX} for the receiver) were set to a common frequency of 200 MHz and well synchronized. The need for wideband true time delay

was replaced by adjusting the phase shift between CLK_{TX} and CLK_{RX}. The output transients were recorded by a real time oscilloscope.

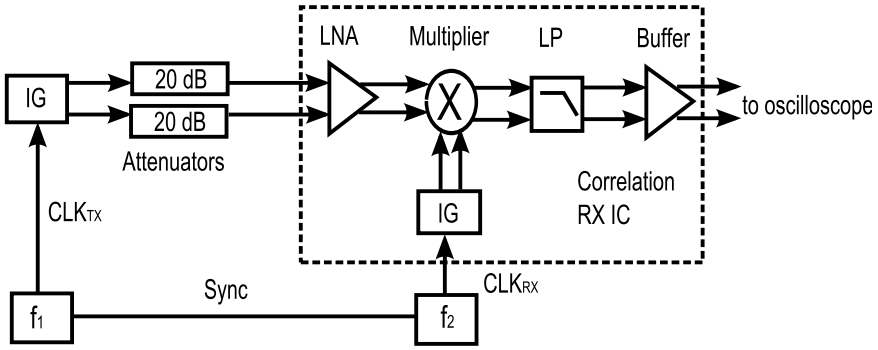

Fig. 4.17: Measurement set-up for characterizing the fabricated correlation receiver frontend. The UWB impulse generator shown in Fig. 3.9 was used to generate input impulses for the receiver.

Fig. 4.18 (a) illustrates the detected differential output transients with a repetition rate of 200 MHz in comparison with simulated ones. In this experiment, the phase shift between CLK_{TX} and CLK_{RX} is manually adjusted for maximum correlation output. As can be seen, it shows an excellent agreement with simulated results. The correlation function of the receiver frontend was evaluated by sweeping the CLK_{RX} in discrete phase steps to generate different time shifts τ between the received and template UWB impulses. The differential correlator output transients versus τ was recorded by the real-time oscilloscope and then integrated over the product for every τ. Both the measured and simulated correlation functions are shown in Fig. 4.18 (b). As can be seen, the measurement is quite similar with the simulated result.

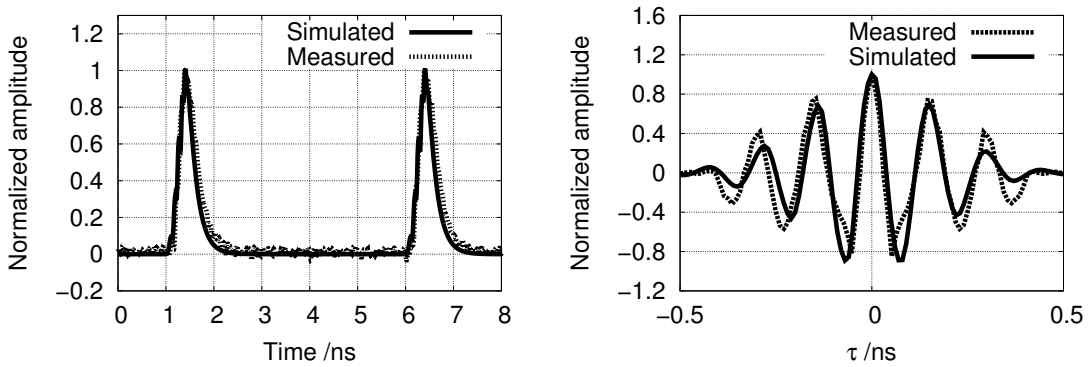

(a) (b)

Fig. 4.18: (a) Comparison of normalized measured and simulated receiver output transients with time-alignment of received and template impulses and (b) on-wafer measured correlation in comparison with a simulated one.

The minimum discernible signal (MDS) can be used for characterizing the receiver sensitivity [55]. Here, the MDS refers to the lowest input signal level which neces-

sary by the receiver to generate an output DC-voltage equal to the RMS noise voltage referred to a specified IF bandwidth. In order to characterize the MDS, the receiver frontend IC was tested with different average input power levels. The experimental set-up was similar as shown in Fig. 4.17. The only difference was that different attenuations were placed between the impulse generator and the receiver IC to introduce different average input signal levels. Here, the average input power level was detected by the Agilent E4416A power meter. The phase shift between CLK_{TX} and CLK_{RX} was adjusted for maximum correlation output voltage amplitude. Fig. 4.19 illustrates the differential correlator DC output voltages captured by a digital voltmeter. The result is plotted in double-log scale. The RMS noise amplitude was

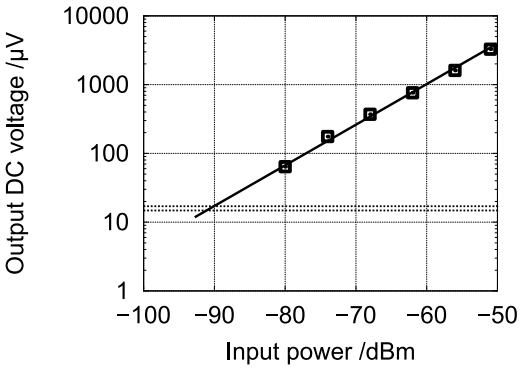

Fig. 4.19: Measured correlator output DC voltages versus input power levels.

evaluated by the Agilent 4395A spectrum analyser. During the measurement, the template impulse generator is fed by a 200 MHz clock signal, while the external impulse generator is switched off. The measured RMS noise voltage with a chosen IF bandwidth of 100 KHz approximately equals to 16 $\pm$ 1.8 μV. The MDS of this receiver can be evaluated by linear regression, as shown in Fig. 4.19. As a conclusion, the MDS of the fabricated receiver IC is approximated to -90.6 $\pm$ 0.6 dBm with a 100 kHz IF bandwidth.

For characterizing the performance of the complete receiver, the IC is glued onto the antenna substrate, as shown in Fig. 4.20. This dipole fed circular slot antenna is

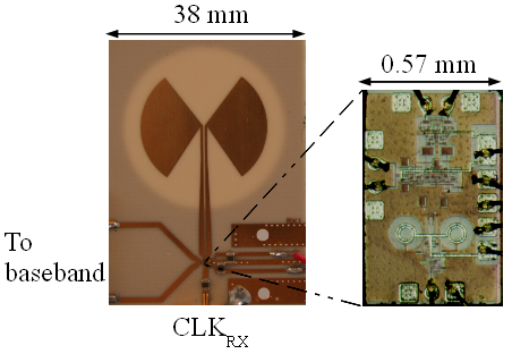

Fig. 4.20: Photograph of the receiver.

realized on a Rogers RO4003C laminate. The receiver IC is wire-bonded to external microstrip transmission lines.

The measurement set-up for characterizing the correlation reception of radiated impulse sequence is shown in Fig. 4.21. The UWB transmitter shown in Fig. 3.15 was

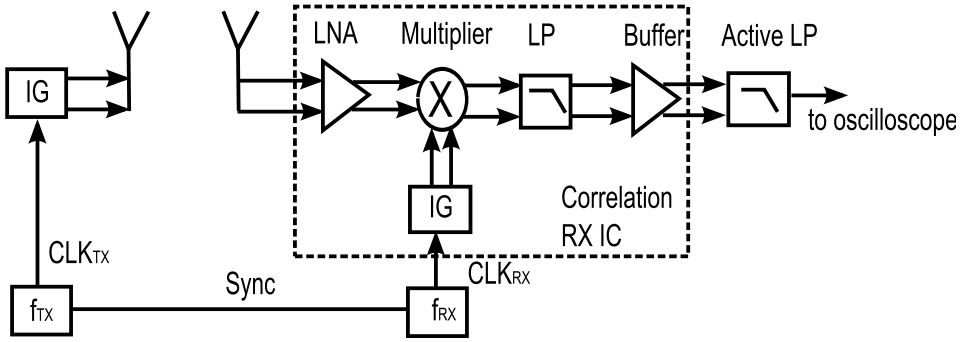

Fig. 4.21: Measurement set-up for characterizing the correlation performance of the fabricated correlation receiver. The UWB transmitter and the receiver were placed at a distance of 20 cm.

used to generate the radiated impulse train. At the receiver side, the received impulses were detected by the correlation based receiver frontend, whose output was connected to an active low-pass filter with a 3 dB corner frequency of 25 KHz. The active filter is based on an operational amplifier with a low-pass filter in each of the two branches, while it also executes the differential to single-end conversion. This active low-pass filter is presented in detail in [27], it is briefly discussed here for clarity. Fig. 4.22 depicts the simplified schematic of the active filter based on two operational amplifiers. This active filter shows a high input impedance (R_1 = 11.3 KΩ) which al-

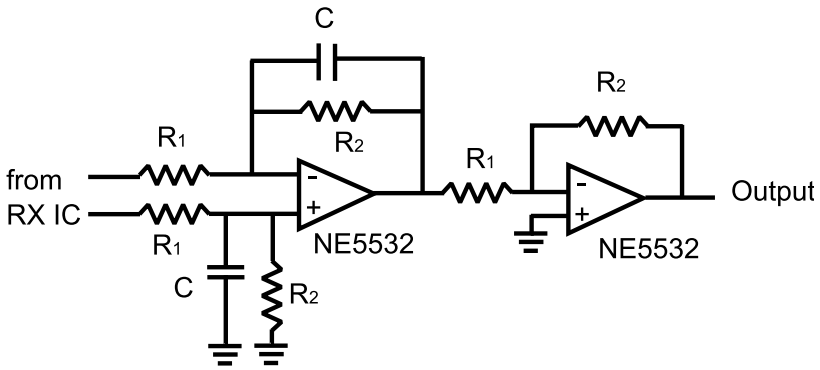

Fig. 4.22: Schematic of the active low-pass filter based on two operational amplifiers. In this design, R_1 = 11.3 KΩ, R_2 = 113 KΩ and C = 56 pF.

lows the filter to be directly connected with the correlation IC. The corner frequency (f_c) of the active filter can be calculated as

$$f_c = \frac{1}{2\pi R_2 C} \tag{4.6}$$

where R_2 = 113 KΩ and C = 56 pF in this design. So, f_c = 25 KHz. Each stage has the same voltage gain, which can be calculated by

$$G_V = -\frac{R_2}{R_1} = -10 \tag{4.7}$$

As a conclusion, this active low-pass filter provides a low-pass property for further integration and a strong amplification to the output signal from the correlation receiver IC.

During the measurements, the transmitter and the receiver were placed at a distance of 20 cm. The method for correlation detection is based on sweeping impulse correlation [27, 76]. A small offset frequency of 100 Hz between the clock frequencies (f_{RX} and f_{TX}) was set to generate a periodically varying time delay between the transmitter and the receiver, which makes the template impulses continuously sweep through the received signals. While the impulses are sweeping, the cross-correlation function is computed by the receiver. Periodic cross-correlation peaks are generated when the received impulse is exactly aligned with the template impulse in time domain. The measured cross-correlation of the received impulses with the template impulses can be seen in Fig. 4.23. The correlation function contains the antenna influences

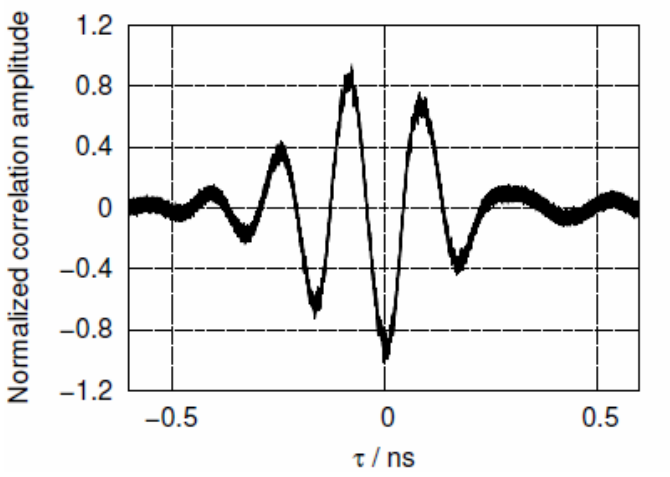

Fig. 4.23: Measured normalized cross-correlation of received impulses with template impulses.

and the channel impulse response. As expected, there is a slight deviation from the correlation function shown in Fig. 4.18 (b).

For demonstrating the suitability of the realized sub-optimal correlation receiver for precise positioning, the transmitter and the receiver were fed by two synchronized 200 MHz sinusoidal signals and co-located while facing to a moving object which was a metal plate with an area of 120 x 150 mm^2 placed at a distance of 20 cm away. The phase shift between the two clock signals was manually adjusted for maximum observable movement amplitude when the target was stationary. This metal plate

was mounted on a linear sled which was moved by an eccentric disc, resulting in a sinusoidal movement. When the plate was moving forward and backward with a movement amplitude of 1 mm, the time-varying output voltage swing from the active low-pass filter is found in Fig. 4.24. As can be seen, the recorded output signal

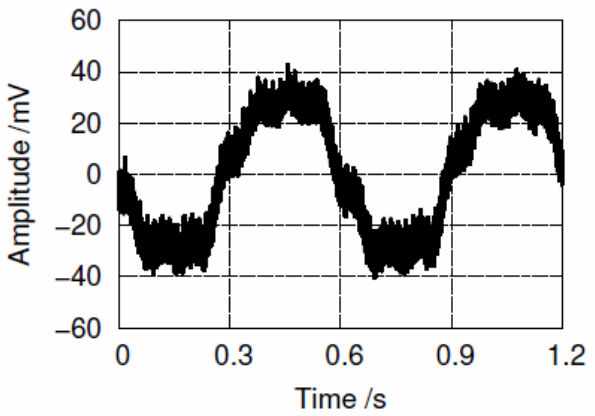

Fig. 4.24: Measurement result obtained on a moving metal target with a movement amplitude of 1 mm at a distance of 20 cm from the realized UWB system.

has a good signal-to-noise ratio, indicating that the true motion tracking capability of the designed system is significantly smaller than 1 mm under these simple lab conditions.

4.3.3 Correlation Reception of Impulse Sequence with BPM

The correlation receiver is tested in connection with the packaged transmitter module shown in Fig. 3.32 (c) to validate the wireless transmission of biphase modulated impulses. It is necessary to notice that the shape of the received UWB impulses will slightly deviate from that of the template impulses. This will correspondingly cause a slight degradation of the amplitude at the receiver output. However, the difference is not taken into account for simplicity. In the experiment, the clock port of the transmitter was fed with a 200 MHz sinusoidal signal, while a signal with a rate of 200 Mbit/s was applied to the data port of the transmitter, as plotted in Fig. 4.25 (a). The impulses sequence directly generated by the impulse generator can be seen in Fig. 3.31 (b).

The fully integrated receiver frontend depicted in Fig. 4.20 was placed at a distance of 20 cm from the transmitter. The clocks of the receiver and the transmitter were manually synchronized. The phase difference between the two clock signals were adjusted for maximum signal amplitude at the correlator output. The measured correlator output transients can be seen in Fig. 4.25(b). Given that the demodulated signal is clearly resolved, this experiment is indicative of a communication speed of 200 Mbit/s, using biphase modulation.

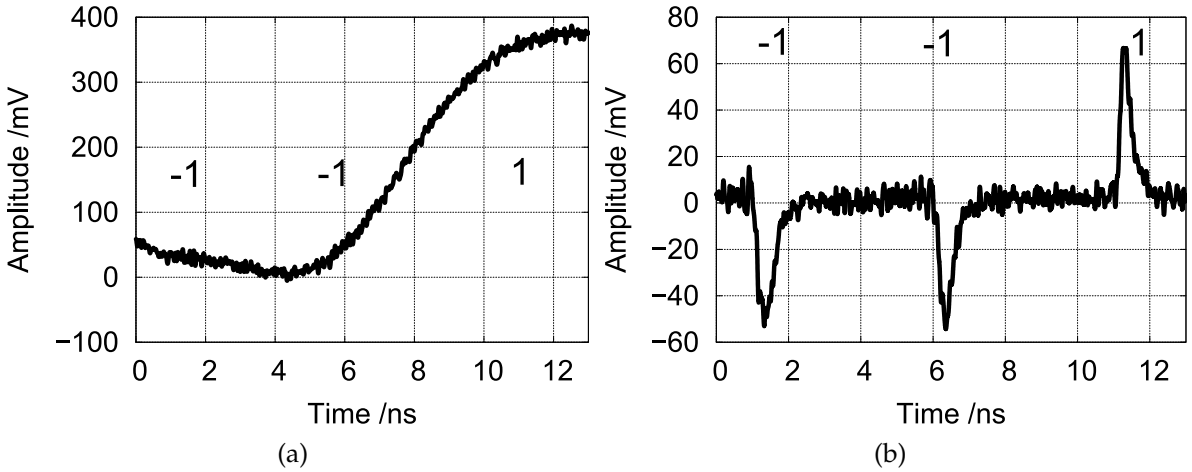

Fig. 4.25: Measured results of (a) the data signal and (b) the demodulated signal from the receiver with the transmitter and the receiver being placed with a distance of 20 cm.

4.4 Energy Detection Receiver

As discussed in Sec. 4.1.2, the key element for an energy detection receiver is a squaring circuit. The proposed energy detection receiver in this work consists of a differential LNA and a differential energy detection circuit which combines a differential squaring circuit, two low-pass filters and a differential buffer, as shown in Fig. 4.26. The detailed design of the energy detection circuit will be discussed in the following.

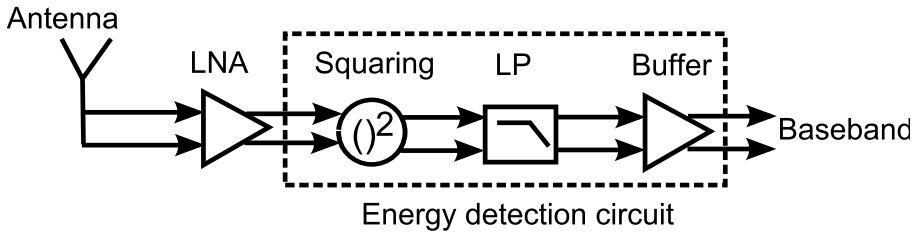

Fig. 4.26: Block diagram of the proposed energy detection receiver.

4.4.1 Energy Detection Circuit

Fig. 4.27 exhibits the schematic of the wideband energy detection circuit, it comprises a squaring circuit, a pair of low-pass filters and a differential output buffer. Similar to the real-time multiplier discussed in Sec. 4.3.1, the core of the squaring circuit is an analog Gilbert cell four quadrant multiplier. The squaring operation is realized by connecting the same signal to both inputs of the Gilbert cell. As can be seen from Fig. 4.27, the differential buffer of the LNA stage is reused here to split the signal path, this in turn saves power consumption. The unbuffered input signal is fed to

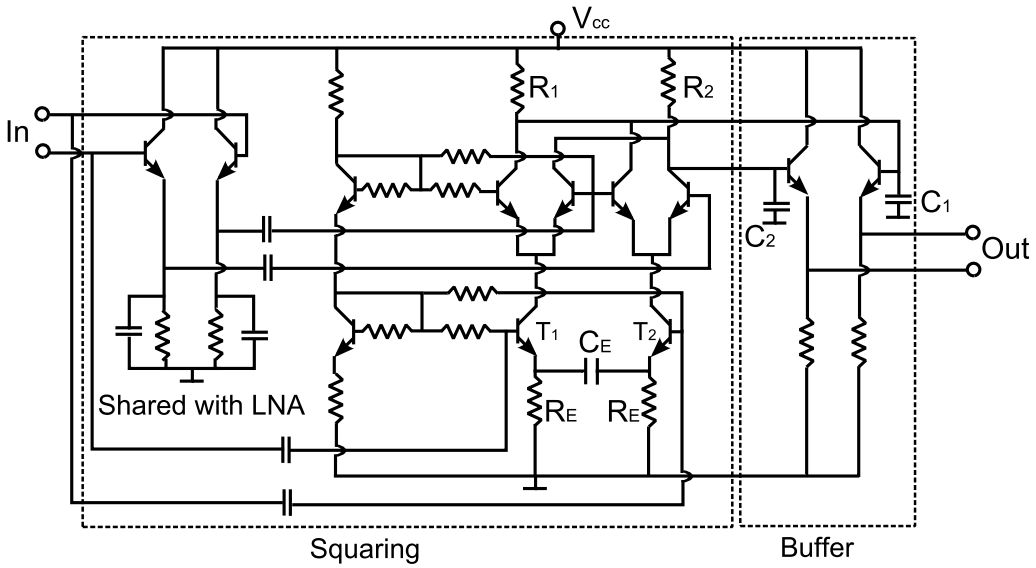

Fig. 4.27: Complete circuit schematic of the energy detection receiver. Detailed circuit parameters are given in Appendix A.7.

the lower pair, while the buffered input signal feeds the top quad. The capacitively shunted resistive emitter degeneration (R_E and C_E) is employed to compensate the gain roll-off at high frequencies, this is critical for achieving a flat gain over the whole UWB frequency band.

The input buffer shared with the differential LNA and the lower pair of the Gilbert cell introduce the same group delay. As a result, the two branches of the input UWB impulses arrive simultaneously at the multiplier. Fig. 4.28 (a) shows a comparison between the output signal waveform of the squaring circuit and the input UWB impulse. The basic squaring operation is clearly visible from the output signal.

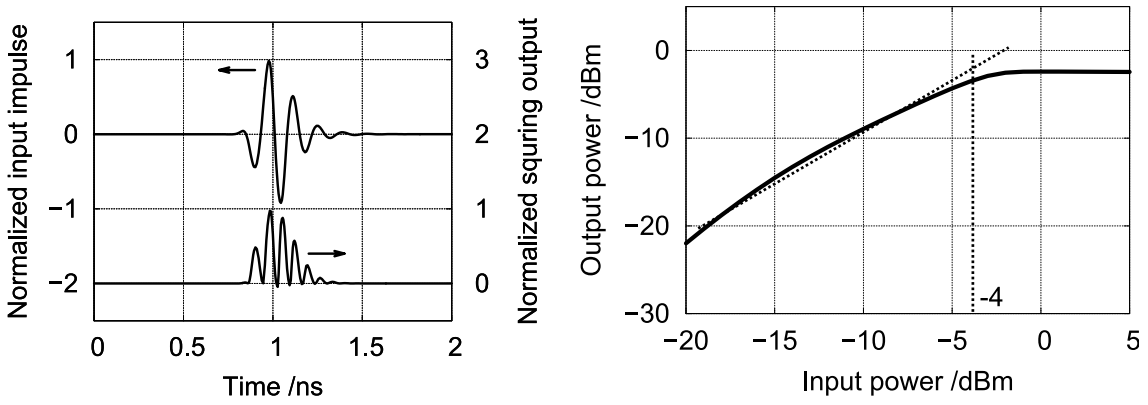

Fig. 4.28: Simulated results of (a) the normalized time-domain output of the squaring circuit and the input UWB impulse and (b) the output power of the energy detection circuit at DC versus input power at 7 GHz.

The output signal of the squaring circuit passes a differential emitter-coupled buffer. The load resistors (R_1,R_2) of the Gilbert cell, together with shunt capacitors (C_1,C_2) of the output buffer form low-pass filters with 1 GHz 3-dB bandwidth. They are required for the detection of the envelope of the squared signal. The simulation result in Fig. 4.28 (b) indicates the linearity of the energy detection circuit. In this simulation, the differential DC output power is recorded versus the input power of a 7 GHz sinusoidal signal. The simulated input 1 dB compression point is -4 dBm. The energy detection circuit has a total DC power consumption of 73 mW, where 42 mW is shared with the LNA.

4.4.2 Fully Monolithic Energy Detection Receiver

The microphotograph of the fabricated energy detection receiver IC is depicted in Fig. 4.29. The compact design has a total chip area of 0.61 x 0.43 mm^2 including all

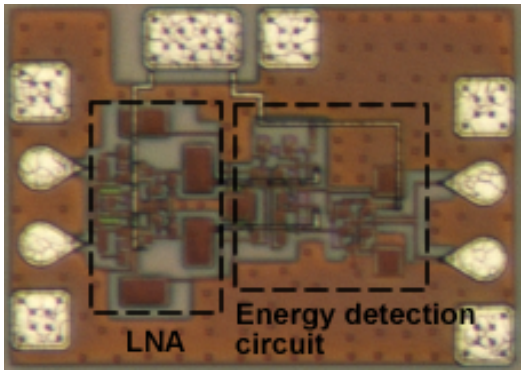

Fig. 4.29: Chip micrograph of the differential energy detection receiver IC. This design has an overall area of 0.26 mm^2.

bond pads. As can be seen from the figure, the receiver layout has a highly symmetric structure, which ensures that the energy detection receiver has the balancing advantages of the differential configuration.

The time domain performance of the receiver IC was characterized on wafer. The experiment set-up can be seen in Fig. 4.30. The impulse generator depicted in Fig.

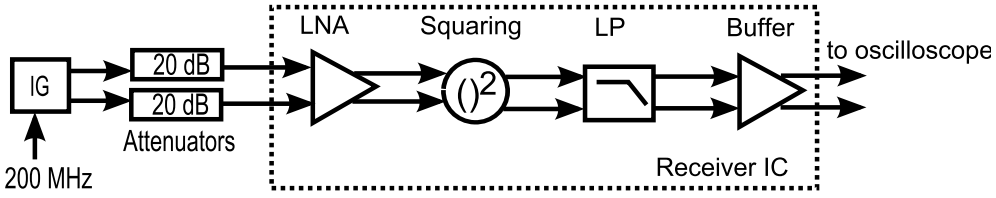

Fig. 4.30: Experiment set-up for characterizing the energy detection receiver IC in time domain.

3.9 was used to generated input UWB waveforms for the energy detection receiver. Here, the impulse generator circuit was operated at an output impulse repetition

rate of 200 MHz. The generated impulses directly from the impulse generator can be seen in Fig. 4.31 (a). Two 20-dB attenuators were inserted between the impulse generator and the receiver IC. A real time oscilloscope recorded the output transient signal from the receiver. The measured receiver output signal is illustrated in Fig. 4.31 (b). It shows that the input UWB impulses are clearly detected by the energy

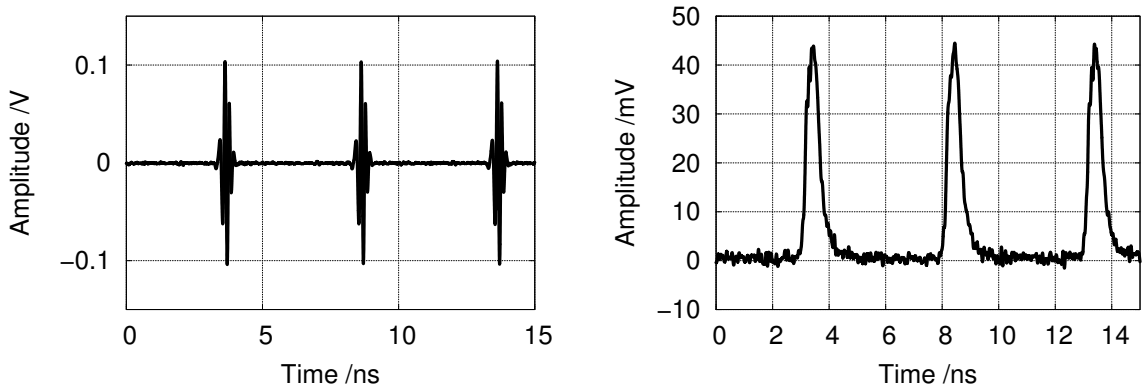

Fig. 4.31: Measured time-domain (a) input UWB impulse sequence and (b) output from the energy detection receiver IC.

detection receiver. The sensitivity of the receiver IC is characterized by measuring the MDS, as discussed in Sec. 4.3.2. Here, the measured differential output DC voltages versus different input power levels can be seen in Fig. 4.32. The measured RMS noise voltage amplitude with an IF bandwidth of 100 kHz approximately equals to 12.5 $\pm$ 1.8 μV. As can be seen, the MDS of the energy detection based receiver IC is approximated to -71 $\pm$ 1 dBm with a 100 kHz IF bandwidth.

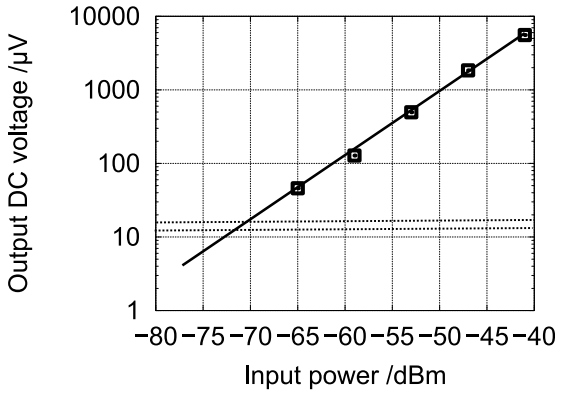

Fig. 4.32: The measured differential output DC voltages versus applied input power. The MDS of the energy detection receiver is worse than that of the correlation receiver.

4.4.3 System Validation: Communications

Similar to the packaging approach for the correlation detection receiver, the energy detection receiver IC is mounted on a 0.81 mm thick Rogers RO4003C substrate, which also carries the dipole feed antenna structures, and is wire-bonded to microstrip transmission lines feeding the antenna, as shown in Fig. 4.33.

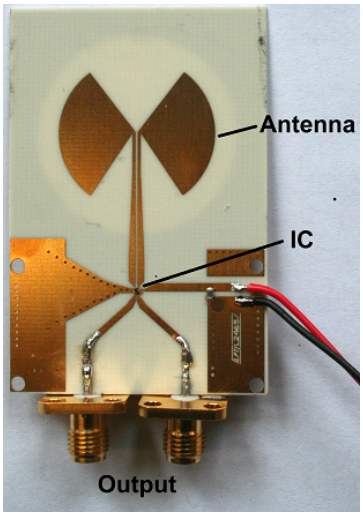

Fig. 4.33: Photo of the packaged energy detection based receiver.

OOK communication

To test the energy detection receiver, a 50 Mbit/s return-to-zero on-off-keying (RZ-OOK) modulated impulse train was generated with the UWB transmitter depicted in Fig. 3.15. The transmitter and receiver were placed at a distance of 20 cm. Fig. 4.34(a) illustrates the input RZ data pattern to the transmitter, and the detected output

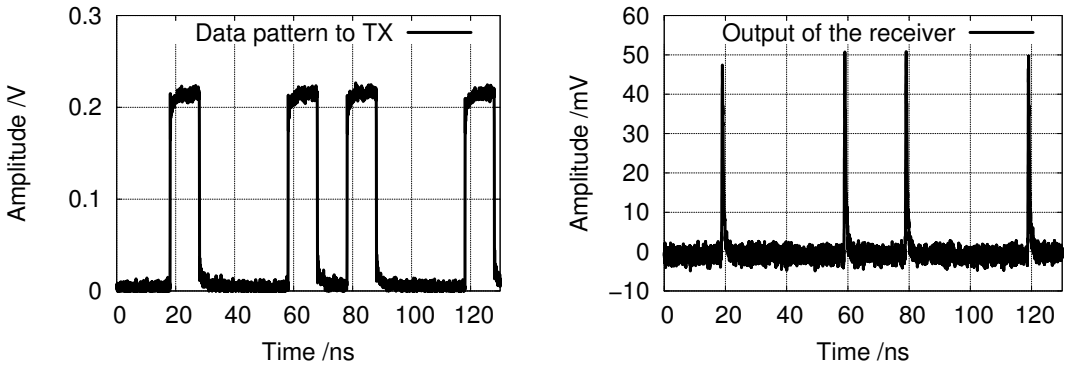

Fig. 4.34: OOK transmission experiment at 50 Mbit/s over a distance of 20 cm. (a) shows the signal at the input to the transmitter and (b) shows the detected signal at the output of the receiver.

waveform from the receiver is plotted in Fig. 4.34(b). As can be seen, the output waveform shows a peak amplitude of 50 mV.

To demonstrate that the realized system is suitable for high-speed communications, the system was tested with a 700 Mbit/s RZ-OOK data pattern applied to the UWB transmitter. The input data pattern is shown in Fig. 4.35(a). The corresponding

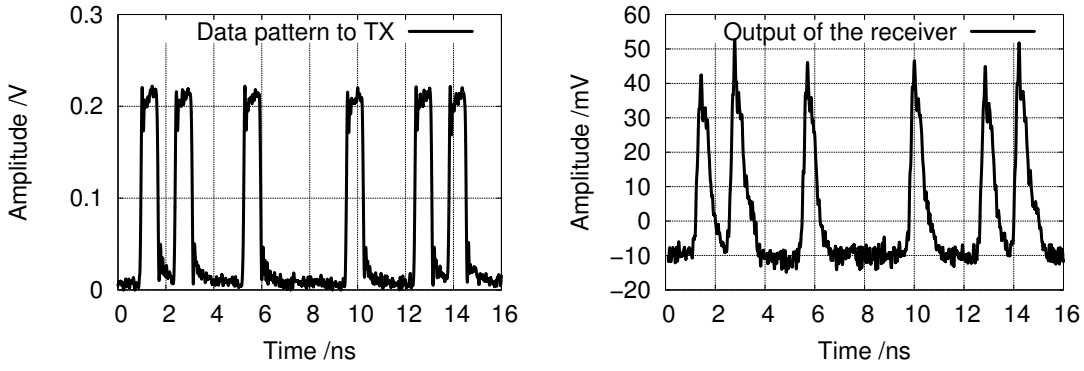

(a) (b)

Fig. 4.35: The measured results of (a) the input data sequence to the transmitter and (b) the output signal of the receiver.

detected impulse envelope at the output of the receiver is presented in Fig. 4.35(b), with a peak amplitude of 50 mV. These two experiments clearly verify that this simple transmitter/receiver combination can be used for OOK high speed communication over a short distance.

FM communication

System implementations dedicated for FM application over IR-UWB have been reported. E.g., [77] presents a frequency modulated sinusoidal signal to trigger an impulse generator, which correspondingly generates a position-varying impulse sequence. On the receiving side, a diode-based rectifier converts the UWB impulses to low frequency signals, then a low-pass filter is used to filter out the FM information. [27] proposes an FM IR-UWB demonstrator based on the frontend circuits described in [77] to perform wireless transmission. The demonstrator uses a commercially available FM test transmitter [78] to generate the clock signal for the impulse generator and a commercial FM radio [79] to recover the final information. The FM centre frequency f_c = 100 MHz, and the FM derivation δf_c = 60 kHz.

The realized energy detection receiver in this work can be well embedded into the demonstrator discussed in [27]. Fig. 4.36 illustrates the differential demonstrator system. As can be seen, the audio signal from the music player is fed into the FM test transmitter (FM modulator), whose output is connected to the input clock port of the UWB transmitter. The FM modulated UWB impulse sequence is detected by the differential energy detection receiver. One output port of the receiver frontend is terminated with a 50 Ω resistor and the other output port is fed into a passive low-pass filter with a cut-off frequency of 150 MHz, which is followed by the commercial

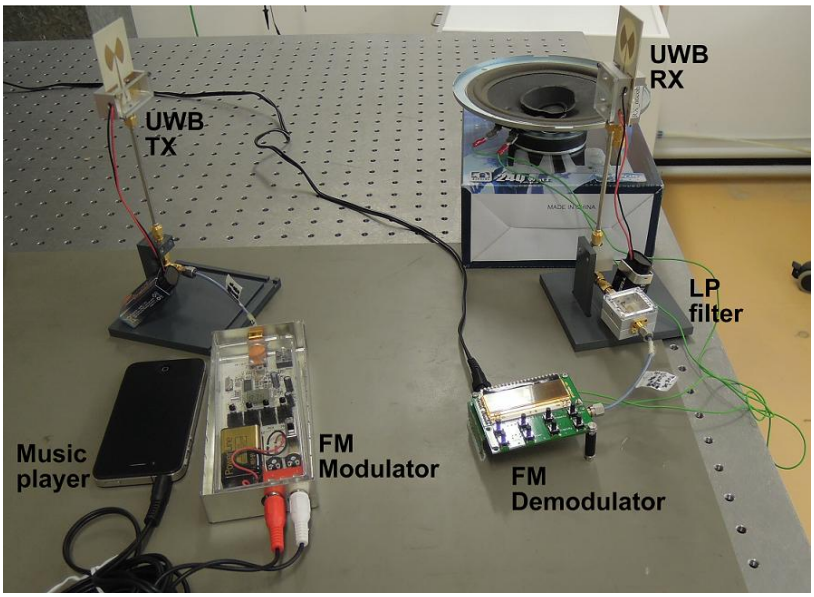

Fig. 4.36: Photograph of the IR-UWB system demonstrator for FM communication.

FM radio performing demodulation of the recovered FM signal. The recovered audio signal is then fed into a loudspeaker. Experimental results show that the maximum communication distance is around 5 m.

Chapter 5

IR-UWB Radar system with a Differential Frontend

This chapter presents a compact IR-UWB radar sensor based on the previously described differential ICs. The proposed radar system utilizes the correlation detection approach. The applications of the sensor system mainly focus on target movement detection, accurate surface estimation and precise localizations.

5.1 System Concept

As shown in Sec. 4.3.2, the designed correlation detection receiver is demonstrated to have the ability of precisely tracking a periodic movement of a metal plate. In this chapter, a differential radar system using the previously described ICs is built to detect the absolute distance from a measuring target, as illustrated in Fig. 5.1. When the target is moving, the radar system can also track this movement.

Different from the system described in Sec. 4.3.2, a direct-digital-synthesizer (DDS) clock generator is employed here to generate two synchronized clocks with a frequency difference of Δf (100 Hz) and Δf itself. The commercial DDS clock generator AD9959 is in the form of an evaluation-board [80]. There are four output channels sharing a common synchronization reference, while the frequency and phase of each channel can be adjusted separately. The minimum adjustable frequency step size is about 0.116 Hz and the minimum phase step size is approximately 0.019 degree. The DDS board frequencies and phases are set by a custom computer program based on LabWindows. To obtain a pure sinusoidal signal by highly suppressing harmonic spurs, a Helix bandpass filter is employed in this system. This filter has an insertion loss of 0.9 dB at centre frequency of 200 MHz, and the 3-dB bandwidth is 6 MHz. Combined with the bandpass filter, the DDS board output signal shows a spurious-free dynamic range (SFDR) of 70 dBc. A detailed description of the filter can be seen in [27].

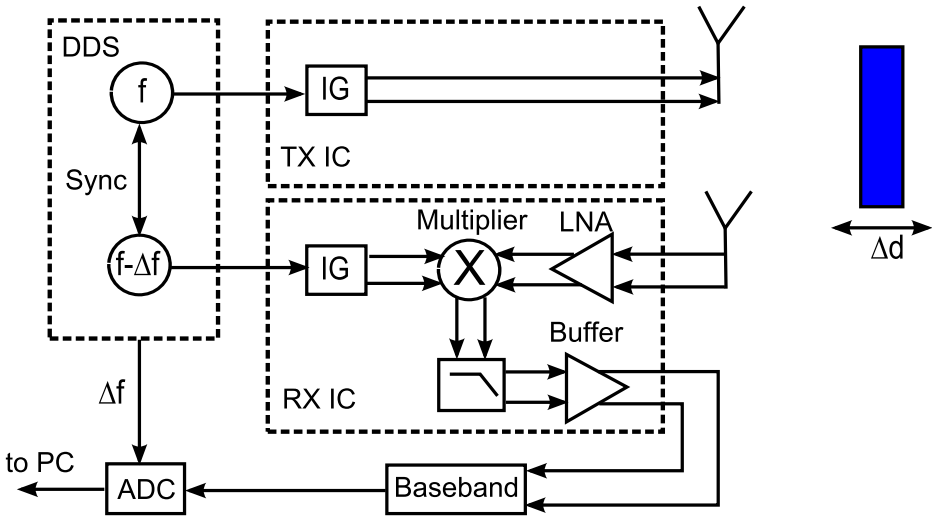

Fig. 5.1: Block diagram of the differential UWB radar system, the measuring target is placed in front of the radar.

The generated two clock signals are used for the UWB transmitter and the template impulse generator on the correlation receiver, respectively. The frequency offset Δf is set to generate a periodically varying time delay between the transmitter and receiver, as mentioned in Sec. 4.3.2. Correspondingly, the cross-correlation function is computed by the correlation receiver. The baseband circuit is realized by an active low-pass filter (f_c = 25 KHz), which performs further filtering and differential to single-ended conversion. The output of the low-pass filter is fed to a dual-channel USB oscilloscope in data logger mode [81], executing the data acquisition and analog to digital conversion, while the frequency offset Δf directly from the DDS board is brought to the other channel. The USB oscilloscope samples data with a 30 μs sampling time and transfers the data to a computer. A C-based programming software is employed to execute the post-processing of the measurement data [27].

The applied transmitter clock signal has a frequency (f_{TX}) of 200 MHz, and Δf equals 100 Hz. So, the repetition rate of the transmitted UWB impulses is equivalent to 200 MHz. Under this configuration, the maximum observation frequency f_{max} can be calculated as

$$f_{max} = \frac{\Delta f}{2} = 50\,Hz \tag{5.1}$$

As can be seen from Eq. 5.1, f_{max} has a value of 50 Hz, which is far sufficient for breath rate detection. Another important parameter, the minimal motion-tracking resolution d_{min} can be written as

$$d_{min} = \frac{c_0 T_s \Delta f}{2 f_{TX}} \tag{5.2}$$

where T_s is the sampling time determined by the data logger oscilloscope. With T_s = 30 μs, d_{min} has a value of 0.56 mm under the described settings. It is worth to

mention that the d_{min} is derived only from sampling considerations and does not take the impulse width into account.

Fig. 5.2 illustrates the measured correlation sweeps and the Δf signal, when the measuring target is stationary. As can be seen, the periodic cross-correlation sweeps have a repetition rate of Δf. A peak-tracking method is employed to estimate the target

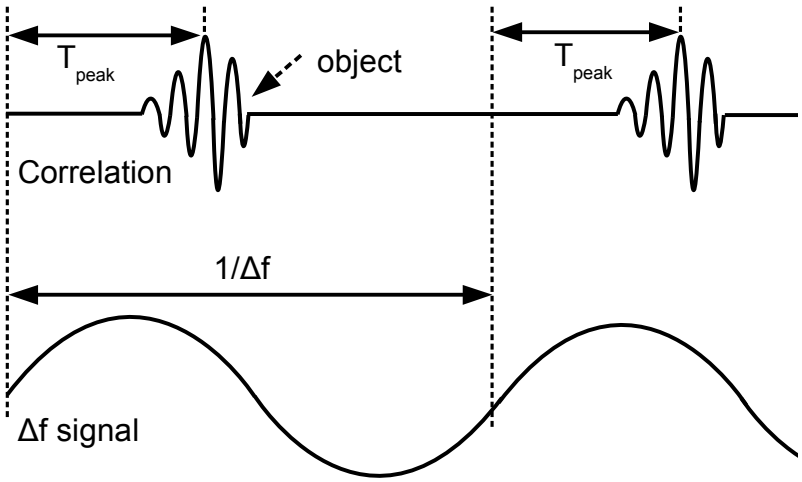

Fig. 5.2: The relationship between the cross-correlation function and the Δf signal.

position. This measurement principle is discussed at great length in [27]. Through detecting of the maximum peak point of the correlation signal, the time instance T_{Peak} corresponding to the target position can be obtained, as shown in Fig. 5.2. Then the distance between the radar sensor and the metal plate can be calculated as

$$d_{target} = \frac{c_0}{2f_{TX}} \cdot T_{Peak} \cdot \Delta f \tag{5.3}$$

When the measuring target is moving, T_{Peak} becomes time-dependent and corresponds to the target movement. This time-varying T_{Peak} can be simply recorded through tracking the maximum peak point of the correlation sweep. As analysed in Eq. 5.1, the maximum observation frequency of the movement equals 50 Hz with the described set-up.

5.2 UWB Radar System

In this section, the implementation of the differential UWB radar sensor is presented. The realized radar sensor is tested in several scenarios to demonstrate the abilities of metal movement tracking, vital sign detection and 3D localization.

5.2.1 Radar Implementation

Based on the system concept shown in Fig. 5.1, the UWB radar sensor has been implemented, as illustrated in Fig. 5.3. For a compact design, the impulse generator IC depicted in Fig. 3.9 is mounted on the transmitter antenna substrate. At the receiver side, both the correlation detection receiver IC and the baseband active low-pass filter are placed on the receiver antenna substrate. Commercial DC voltage regulators are employed on both PCB boards to supply all the circuits from one 9 V battery.

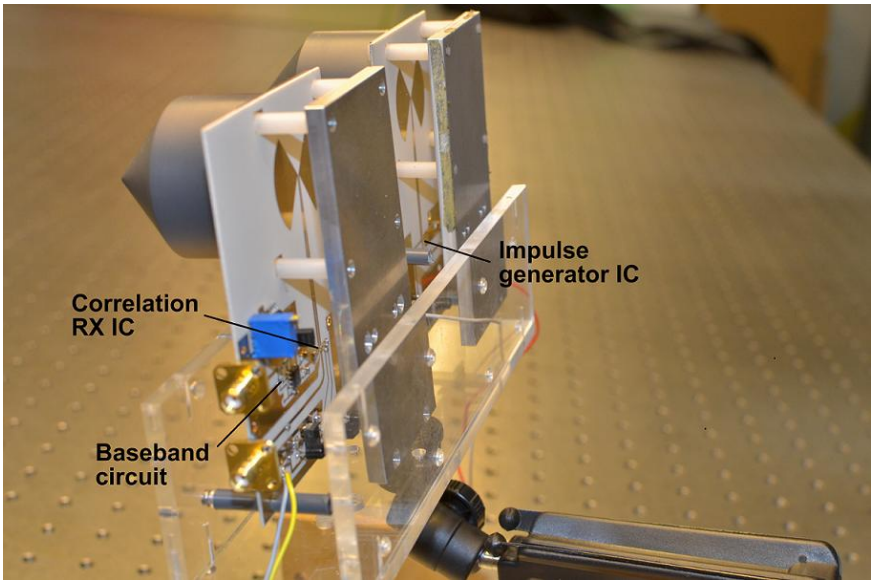

Fig. 5.3: The photograph of the compact differential UWB radar system. The ICs are placed chip-on-board on the antenna substrate for a compact design.

Different from the antennas depicted in Fig. 3.15 and Fig. 4.20, dielectric rod antennas fed by a planar structure are employed here due to their directional property. The rod antenna is reported in [82], however, it is briefly explained here for clarity. In principle, this antenna is the combination of the planar UWB antenna as shown in Fig. 3.15 with a circular dielectric rod. The planar antenna is used as a feed for the rod antenna. Meanwhile, a metal reflector is placed at a specified distance behind the planar feed element to achieve an unidirectional radiation pattern, which makes the antenna especially suitable for radar applications. This distance equals $\lambda/4$ at 5.35 GHz, which can result in an optimized average gain over the complete UWB range [82]. Fig. 5.4 (a) illustrates the detailed sketch of this antenna, where the rod is rendered transparent to indicate the planar antenna. Fig. 5.4 (b) plots the measured radiation pattern in H-plane. As can be seen, a small beam width is achieved. The fabricated antenna shows a measured return loss better than 10 dB from 3.5 to 11.8 GHz, which is far sufficient for UWB applications. It achieves a flat gain with a mean value of 8.7 dBi in the complete FCC allocated frequency range. The baseband circuit is realized by an active low-pass filter based on commercial operational amplifiers, whose schematic has been plotted in Fig. 4.22. As mentioned before, the designed

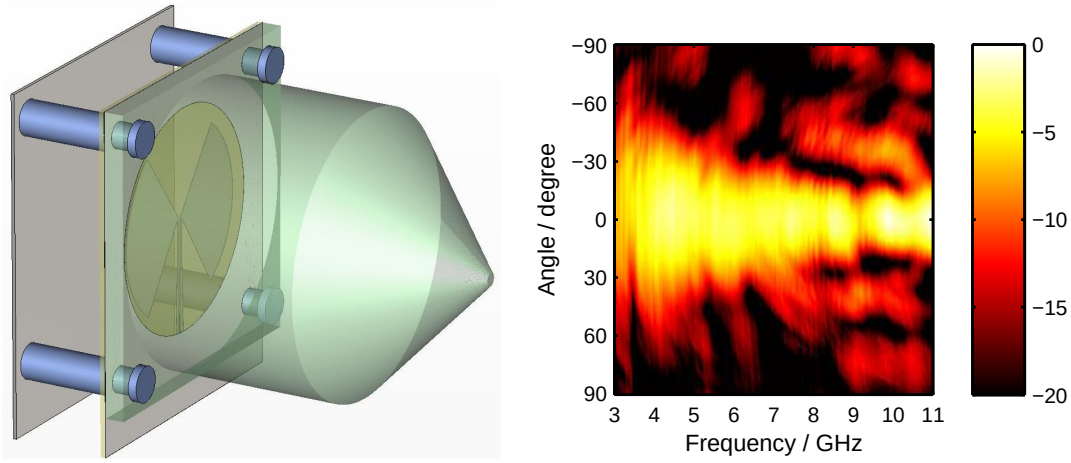

(a) (b)

Fig. 5.4: (a) The sketch and (b) the measured radiation pattern of the realized UWB antenna.

active filter provides a low-pass property for further filtering and a strong baseband amplification.

Fig. 5.5 shows the front-view pictures of the fabricated transmitter and correlation receiver. An extremely compact design is achieved through placing the ICs and the active low-pass filter on the antenna boards.

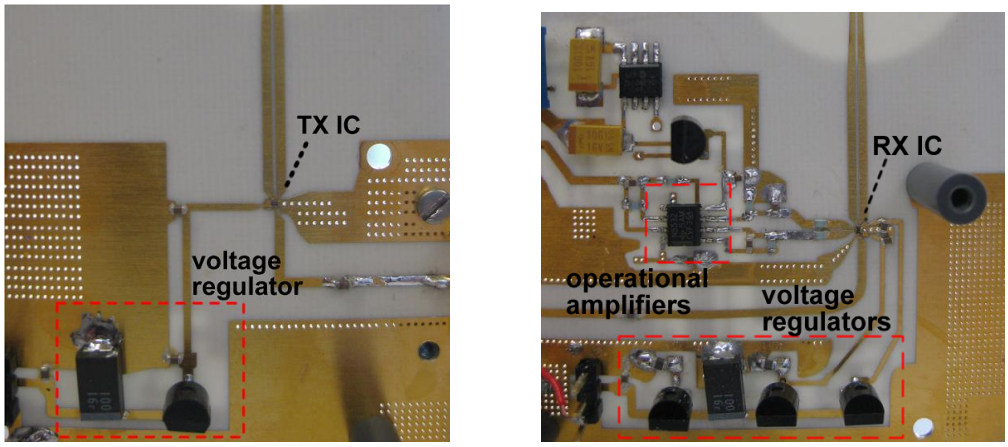

(a) (b)

Fig. 5.5: Front-side view of (a) the transmitter and (b) the complete receiver with RF frontend IC and the baseband circuitry. Both the impulse generator and the receiver IC are mounted on the antenna substrates and wire-bonded to external micro-strip transmission lines.

5.2.2 Tracking the Movement of a Metal Plate

In this subsection, the ability of the realized UWB radar for tracking a moving metal plate is demonstrated. The metal plate which is mounted on a sledge driven by an eccentric disk is placed in front of the UWB radar sensor, as illustrated in Fig. 5.6.

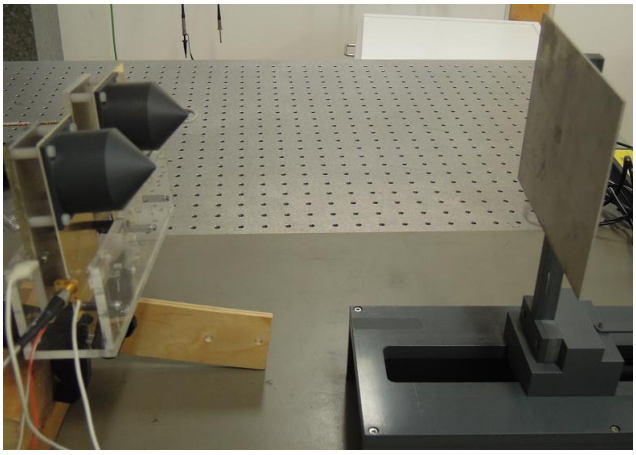

Fig. 5.6: Photograph of the UWB radar measurement platform for tracking the movement of a metal plate.

In the first measurement, the stationary metal plate was placed at a distance of 15 cm in front of the sensor. To verify the movement tracking ability, the metal plate was periodically moved back and forth with an amplitude of 1.5 mm, correspondingly generating a sinusoidal deviation. The measured time domain result is given in Fig. 5.7 (a). It shows that both the absolute distance and the movement deviation are clearly detected. Fig. 5.7 (b) illustrates the calculated spectrum information from the time-domain measurement result. The highest point is clearly visible and indicates

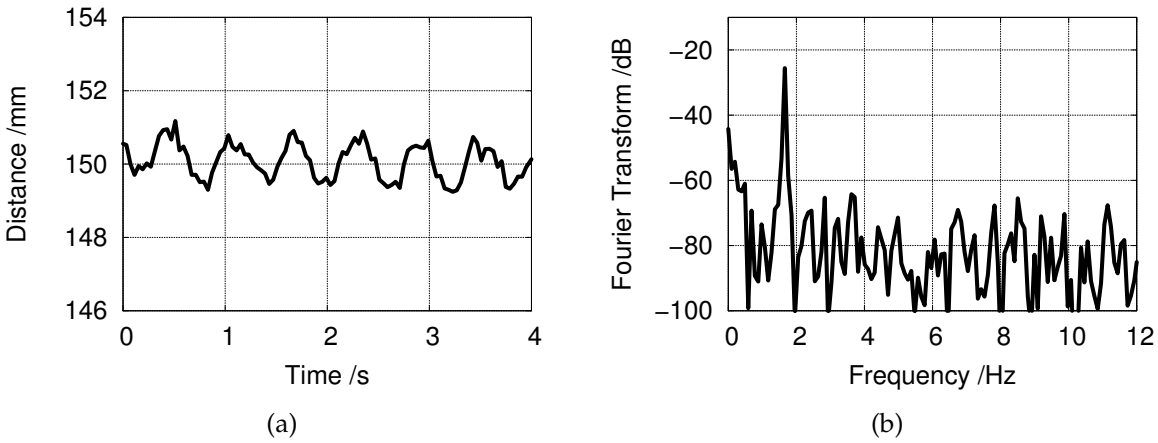

Fig. 5.7: Measured results of a moving metal plate in front of the UWB radar with a mean distance of 15 cm in (a) time and (b) frequency domain.

that the periodic motion frequency of the metal plate equals 1.7 Hz.

Then the distance between the metal plate and the sensor is increased to 30 cm. Fig. 5.8 depicts the measured results in both time and frequency domains. It can be seen

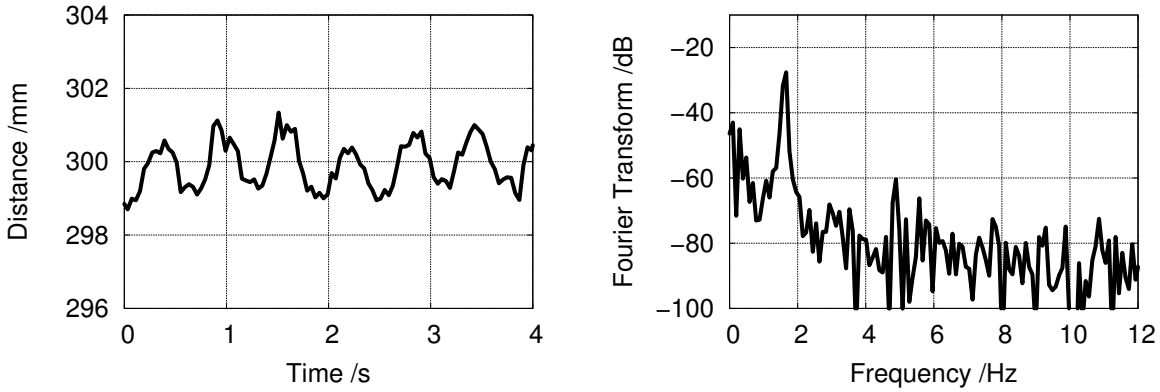

(a) (b)

Fig. 5.8: Measured results in (a) time and (b) frequency domain. The metal plate is placed at a mean distance of 30 cm from the UWB radar sensor with a movement deviation of 2 mm.

that the metal plate moves with a deviation of 2 mm and a rotating speed of 1.7 Hz. The experiments show that this compact short-range UWB radar successfully tracks the metal plate's movement.

5.2.3 Breath Rate Detection

The IR-UWB approach has been considered as an interesting candidate for medical applications, such as respiratory rate monitoring [83] and biomedical imaging [84]. The low radiated power is harmless to human bodies. Furthermore, the short time-domain impulses enable high range resolution and real time localization in dynamic environments.

The realized differential UWB radar sensor in this thesis can be well used for breath rate monitoring. To demonstrate this functionality, an adult male with pronounced tachypnea stood around 18 cm from the radar sensor. The recorded time-domain data can be found in Fig.5.9 (a). The result shows that the breathing pattern is clearly detected and the breathing amplitude is around 5 mm. The time domain data is Fourier transformed to frequency domain and depicted in Fig.5.9 (b). It indicates that the respiration rate of this tested person is around 35/min.

5.2.4 3D Localization

IR-UWB technology is a great candidate for precise localization applications. Various UWB systems for localizations have been reported, e.g., [85] proposes a UWB system

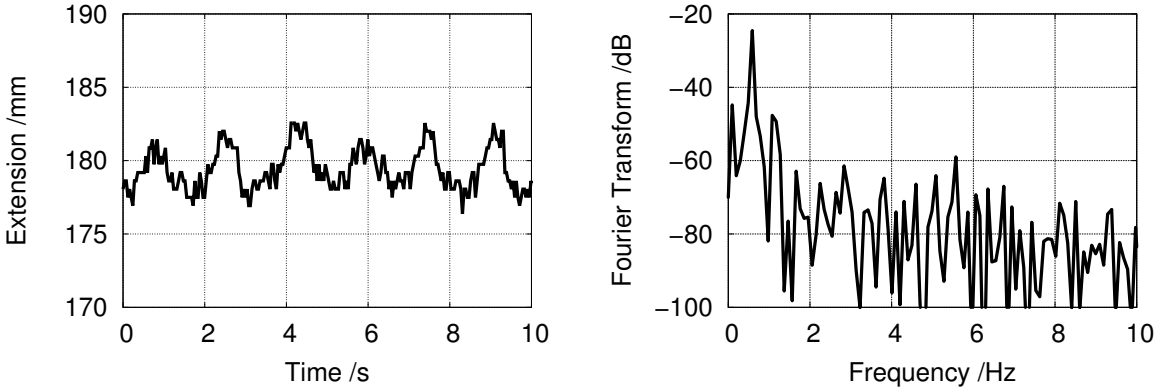

Fig. 5.9: Measured results of vital signs of a male test person standing in front of the UWB radar sensor in (a) time and (b) frequency domain.

for indoor localizations based on the TDoA technique. Energy detection receivers are employed to localize the tag position in this system. Another realized application employs UWB wireless sensor networks for localizing underground mines, as discussed in [86]. In this thesis, a precise localization approach of a transmitter placed inside the human body is proposed. The potential application of the proposed system could be the tracking of catheters equipped with active UWB beacon transmitters.

The UWB localization system in this work combines the differential radar sensor with the active UWB beacon transmitter presented in Sec. 3.6, in other words, the radar sensor is utilized to find the position of the beacon transmitter. As previously mentioned, the UWB beacon transmitter includes a power amplifier to achieve high output voltage swing to partly compensate the strong loss in the human tissue. The localization approach is proposed by Michael Mirbach and discussed in detail in [87], it is briefly repeated here for clarity.

Consider that the UWB beacon transmitter is placed into a tissue mimicking liquid, the approach for locating the beacon transmitter can be divided into the following three steps:

1. The beacon transmitter is switched off in this step. The UWB radar sensor is scanned along both x and y-axes to measure the distances from known antenna positions to the boundary surface points. Using a surface estimation algorithm which will be discussed in Sec. 5.2.4.1, a smooth boundary surface model can be obtained.

2. Next, the beacon transmitter inside the liquid is switched on. The radar sensor is operating in the receiving mode by turning off its transmitter. The generated impulses from the beacon transmitter are detected by the radar sensor which performs as a UWB receiver. The information of time-of-arrival (ToA) is ac-

quired. The radar sensor is scanned at different positions to record different ToA values.

3. Based on the recorded data and a proposed localization algorithm, the transmitter position is detected.

The localization algorithm deals with the estimated boundary surface model and the measured ToA of the localization signal at every measurement point. It is worth to mention that the wave propagation velocity in the medium is different from that in air, because of the permittivity difference. Correspondingly, refraction similar to geometrical optics happens at the boundary. In this sense, the boundary surface model is extremely critical. The following subsection discusses a boundary surface estimation method.

5.2.4.1 Target Boundary Estimation

UWB impulses are strongly reflected at the air-to-body interface because the relative permittivity of the human tissue is between 30 and 50 in the FCC allocated UWB frequency range. This property makes IR-UWB suitable for boundary surface estimation.

In this subsection, the described UWB radar sensor is investigated for target surface estimation without knowing any information about the boundary surface structure. The estimation algorithm is based on trilateration and published in [88]. The principle is briefly repeated in this thesis for clarity. Compared with other estimation algorithms, such as the Seabed algorithm [89] and the Envelope of Spheres algorithm [90], the trilateration approach has the great advantage of simple implementation.

If a target is placed in front of the previously described UWB bistatic radar, a set of measured data can be obtained through measuring at different antenna positions. Trilateration method identifies the intersection of ellipsoids corresponding to the distances measured by the UWB radar, with assuming that the radar sensor looks towards the same scattering centre at two neighbouring positions. Fig. 5.10 shows the cross section of a measured ellipsoid, where the transmitter and receiver antennas have a space of s under this bistatic configuration. Through measuring the time of flight, the value of r_1+r_2 can be obtained. Correspondingly, the ellipsoid radii (a_1 and b_1) in this measurement can be derived as

$$a_1 = \frac{r_1 + r_2}{2} \tag{5.4}$$

and

$$b_1 = \sqrt{a_1^2 - (\frac{s}{2})^2} \tag{5.5}$$

In y-direction, the radius is also equal to b_1 because of the rotation-symmetric property with respect to the x-axis. Then another measurement can be performed with

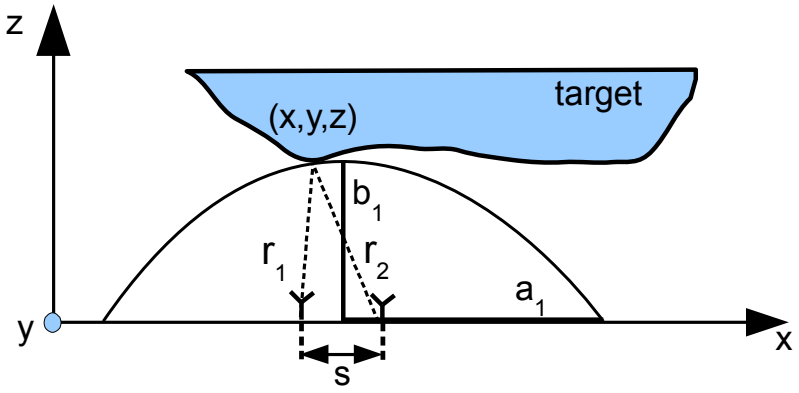

Fig. 5.10: Cross section of one measured ellipsoid with the transmit antenna and receive antenna placed with a distance of s.

moving the bistatic radar along x-axis with a step of d_x. The corresponding ellipsoid radii can be calculated as a_2 and b_2. In a third measurement, the radar is moved along y-axis with a step of d_y, and the corresponding ellipsoid radii are a_3 and b_3. Based on the assumption that the antennas are looking at the same scattering centre with the above three measurements, the following equations can be obtained

$$\frac{x^2}{a_1^2} + \frac{y^2}{b_1^2} + \frac{z^2}{b_1^2} = 1 \tag{5.6}$$

$$\frac{(x-d_x)^2}{a_1^2} + \frac{y^2}{b_1^2} + \frac{z^2}{b_1^2} = 1 \tag{5.7}$$

$$\frac{x^2}{a_1^2} + \frac{(y-d_y)^2}{b_1^2} + \frac{z^2}{b_1^2} = 1 \tag{5.8}$$

By solving these three equations, the target coordinates (x,y,z) as shown Fig. 5.10 can be given as

$$\begin{aligned} x &= \frac{d_x^2 b_2^2 + b_1^2 a_2^2 - b_2^2 a_2^2}{2 d_x^2 b_2^2} \qquad if \;\; a_1^2 b_2^2 = a_2^2 b_1^2 \\ x &= \frac{-2 d b_2^2 a_1^2 + a_1^2 a_2^2 \sqrt{X}}{2(a_2^2 b_1^2 - a_1^2 b_2^2)} \qquad if \;\; a_1^2 b_2^2 \neq a_2^2 b_1^2 \end{aligned} \tag{5.9}$$

with

$$X = \frac{2 d_x^2 b_2^4}{a_2^2} - 4\left(\frac{a_2^2 b_1^2 - a_1^2 b_2^2}{a_1^2 a_2^2}\right)\left(b_2^2 - b_1^2 - \frac{d_x^2 b_2^2}{a_2^2}\right) \tag{5.10}$$

and

$$y = -\frac{1}{2 d_y}\left[b_3^2 - b_1^2 - d_y^2 + x^2\left(\frac{a_3^2 b_1^2 - a_1^2 b_3^2}{a_1^2 a_3^2}\right)\right] \tag{5.11}$$

and

$$z = \sqrt{b_1^2 - y^2 - \frac{b_1^2 x^2}{a_1^2}} \tag{5.12}$$

These calculated coordinates refer to the radar position depicted in Fig. 5.10. Then, the position of the next target surface point can be estimated by three further measurements with changing radar positions. Finally, the target surface model can be obtained by linearly scanning the radar along both the x- and y-axes.

For verifying the proposed algorithm, two experiments were carried out using the realized UWB bistatic radar sensor. In the first experiment, the measurement target is a container filled with a sugar solution whose properties are similar to those of human tissue, as depicted in Fig. 5.11 (a). The container was placed in front of the UWB radar with a distance of 18 cm. The purpose of this measurement was to identify the

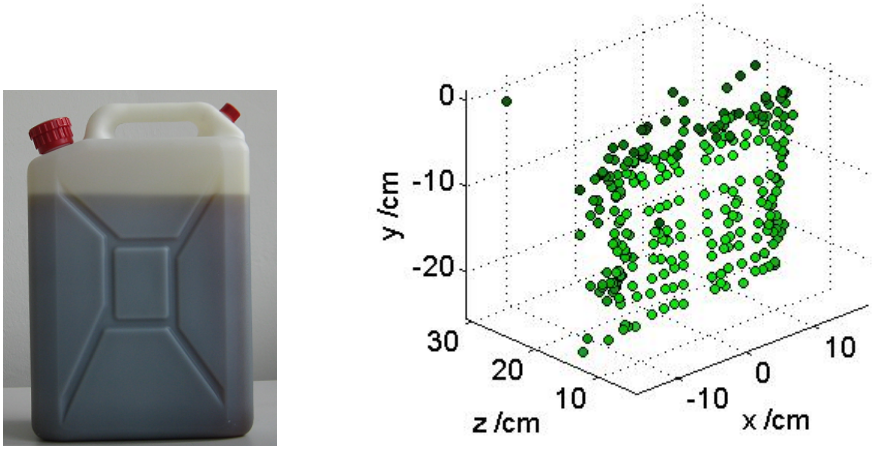

(a) (b)

Fig. 5.11: (a) Photograph of the liquid container and (b) the measured cloud of estimated surface points.

planar surface structure. The measurement was performed by moving the radar up and down in 2 cm steps along both the x- and y-axis and by rotating the container in 5 degree steps. A cloud of estimated surface points representing the surface of the lower part of the container are illustrated in Fig. 5.11 (b). It can be seen that the planar surface structure of the container is successfully determined.

Another 3D surface measurement based on the trilateration algorithm was performed by detecting the surface of a male torso, which has a more complex surface structure compared to the liquid container. As can be seen in Fig. 5.12, a plastic dummy of a male torso with a hight of 60 cm was selected as the measurement target. The surface of the dummy was covered with highly conductive copper laque to enhance the reflectivity. The male torso was placed in front of the radar sensor with a distance of 30 cm. The scanning of the target surface was done by shifting the bistatic radar up

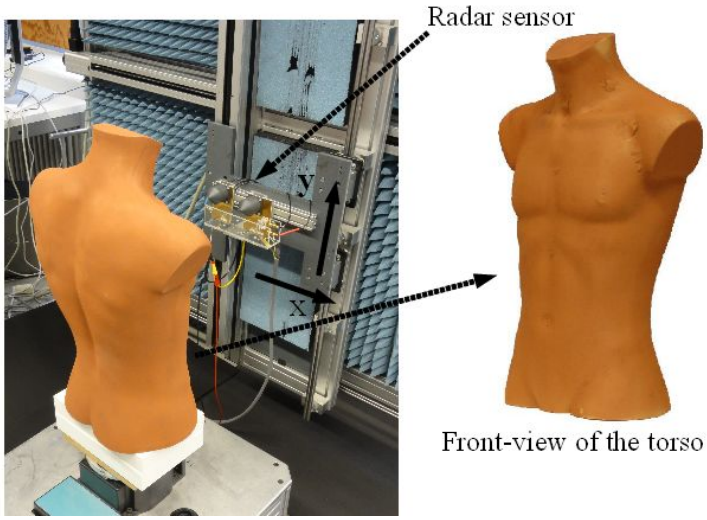

Fig. 5.12: Photograph of the measurement set-up for detecting the surface of a male torso.

and down in 2 cm steps along both the x- and y-axis and by rotating the container in 5 degree steps.

Fig. 5.13 illustrates the measurement results, which clearly indicate the distance from the radar sensor to the male torso and the target surface structure. These two exper-

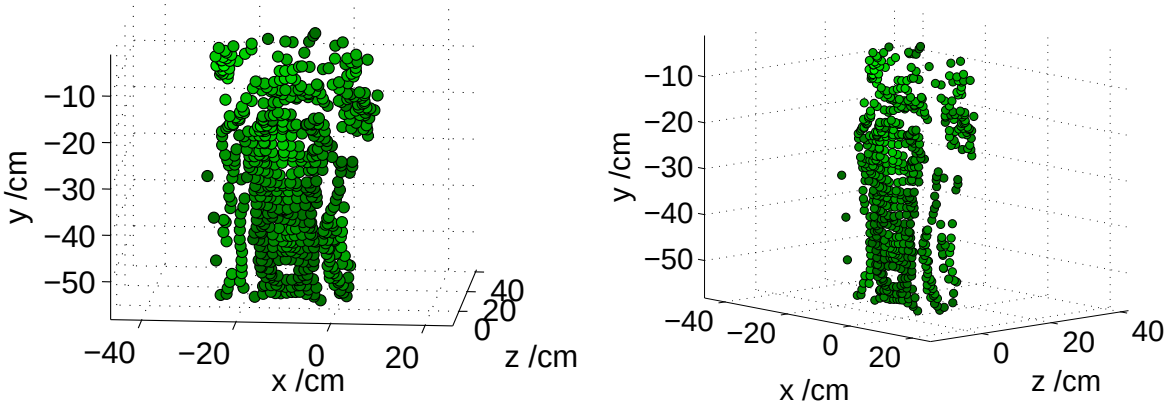

Fig. 5.13: (a) Front and (b) right-side view of estimated surface points using the proposed trilateration-based imaging algorithm for the surface measurement of the human torso dummy.

iments successfully prove that the trilateration-based imaging algorithm works well with the realized radar sensor hardware. Detailed discussion about the error distance for this algorithm can be found in [88].

5.2.4.2 3D Localization Experiment

As previously discussed, the beacon transmitter is switched on after obtaining the surface boundary. The impulses generated by the beacon transmitter in the medium are sent to the radar sensor in the air. However, this transmission can be treated reversely because the wave propagation is reciprocal. Assuming that the UWB impulses are originated from receiving antenna positions and sent into the medium, the intersection of wavefronts inside of the medium corresponds to the transmitter position. The virtual wavefront is transmitted at each receiver position with a delay corresponding to respective measured ToA. So, the localization algorithm is required to figure out the intersection point of the wavefronts, which makes the analysis simpler. Detailed discussion on the algorithm can be found in [87].

The realized UWB radar sensor is employed to verify the aforementioned localization algorithm. The measurement set-up is illustrated in Fig. 5.14. The UWB beacon

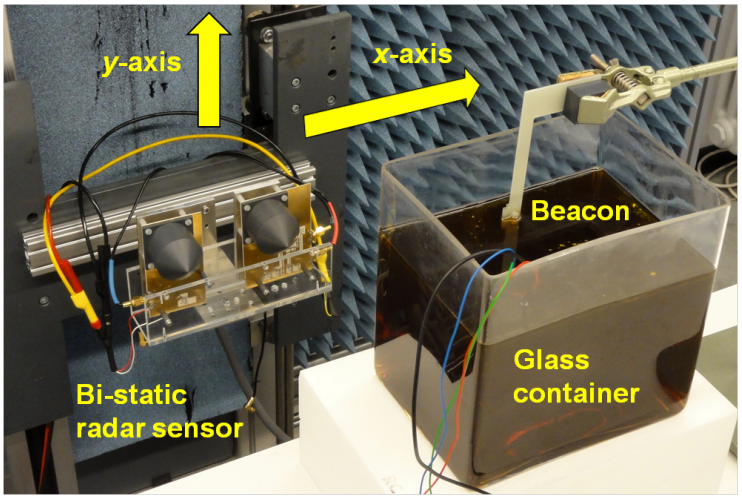

Fig. 5.14: Photograph of the 3D localization measurement set-up with a beacon transmitter placed in a rectangular liquid container.

transmitter described in Sec. 3.6.4 is immersed in human tissue mimicking liquid HSL 5800 which is filled in a rectangular glass container. The radar is placed in front of the container with a distance of 22 cm. At the first step, the estimation of the container surface is performed based on the algorithm discussed in Sec. 5.2.4.1. The active beacon transmitter is powered off during this measurement. The radar sensor is moved in 1 cm steps along the x- and y-axes at position of z = 0. The distances from the radar position to the surface points can be detected. The estimated point cloud is depicted in Fig. 5.15. As can be seen, interpolation of these points leads to an estimated smooth container surface. It is served for estimating the refracted wavefronts. Then, the UWB transmitter placed in the container is switched on. The radar sensor operates in receiving mode with its transmitter powered off. The measurement is performed by scanning the radar sensor in 2 cm steps along the x- and y-axes and recording corresponding ToA_n. Fig. 5.16 (a) illustrates the output correlation signal from the radar sensor at one measurement position. As can be seen, the original

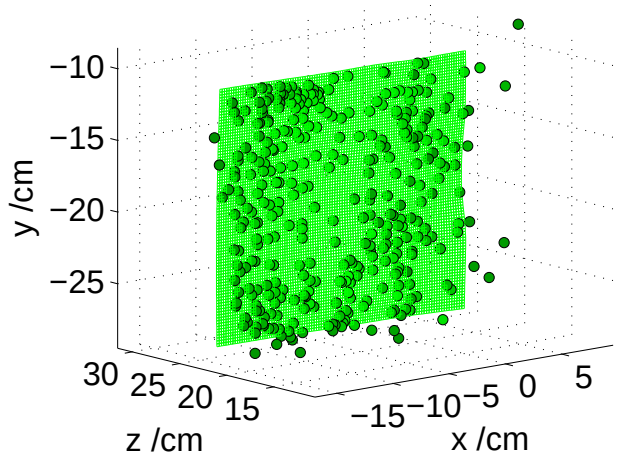

Fig. 5.15: Estimated surface points using the trilateration-based imaging algorithm. A smooth 2D surface shape can be interpolated.

measurement has a very low SNR mainly due to the extremely high attenuation of the human tissue mimicking liquid HSL 5800. However, the result is sufficient to in-

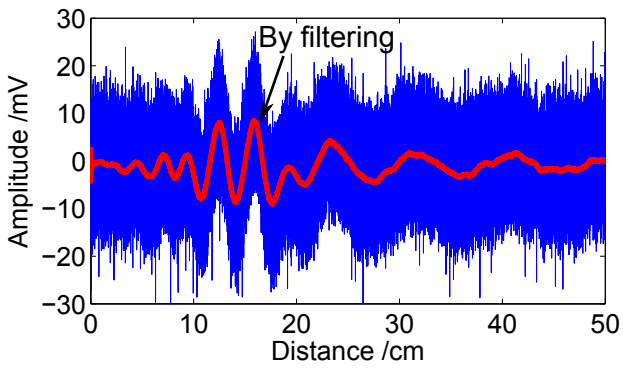

(a)

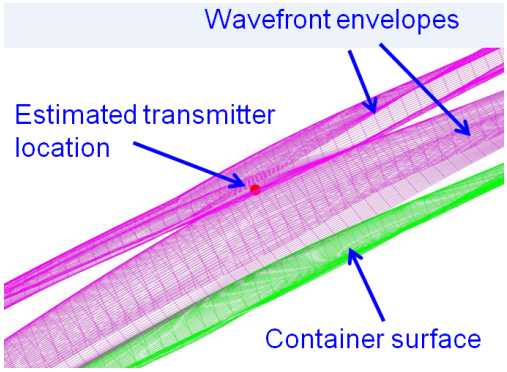

(b)

Fig. 5.16: (a) Received output correlation signal from the receiver of the radar sensor and (b) the constructed wavefronts using the information of measured ToAs and the estimated surface model.

dicate that the impulses sent from the beacon transmitter are detected. With knowing ToAs and the boundary surface, the refracted 3D wavefronts can be easily obtained by superposition of spheres, as illustrated in Fig. 5.16 (b). Finally, the transmitter postion can be estimated through using wavefront intersections. Fig. 5.17 depicts a top view and a side view of the estimated localization results of the beacon transmitter which is placed behind the container surface. The result clearly indicates that the beacon is placed 1.7 cm away from container surface and the estimated position is (x, y, z)=(-6 cm, -21 cm, 22 cm). The comparison of the estimated transmitter position to the manually measured beacon coordinates is also shown in Fig. 5.17. As can be seen,

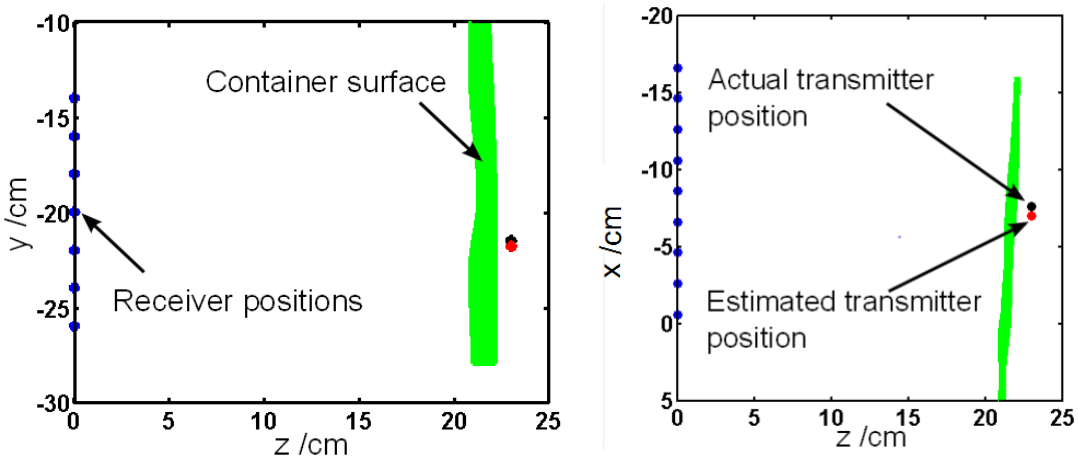

(a) (b)

Fig. 5.17: Measured results in the (a) top and (b) side view. The comparison of the estimated position to the manually measured coordinates shows a good agreement.

there is a good agreement between the estimated and manually measured positions. Only a small derivation of 0.6 cm is generated in the x-direction.

Chapter 6

Monostatic Radar Frontend

The previously described UWB radar set is based on a bistatic configuration which requires separate transmitter and receiver antennas. To reduce the overall system complexity, the radar architecture is migrated to a novel monostatic approach, which would significantly reduce the overall radar size due to the elimination of one UWB antenna.

Monostatic IR-UWB radar systems have been considered for a long time [91]. However, few monolithic implementations have been reported so far. Transceiver IC implementations for UWB radar application have been proposed in [92] and [93], but separate antennas are employed. The primary challenge for the monostatic UWB approach is that the switching between transmitting and receiving paths has to be very fast, because 1 ns switching time corresponds to a 30 cm travel distance for the UWB impulses in air. Furthermore, the losses of the wideband switch may significantly increase the receiver noise figure. In this thesis, a novel monostatic front approach is proposed to avoid using high speed UWB switches. The concept is mainly based on a merged impulse generator/LNA module with sleep modes. Controlled by proper signal sequencing, a monostatic radar frontend can be realized.

Fig. 6.1 depicts the block diagram of the proposed UWB monostatic radar system. In this thesis, the impulse generator/LNA module is designed, fabricated and characterized. As can be seen in Fig. 6.1, the input ports of the fully differential LNA are directly connected with the output ports of the buffer amplifier following the UWB impulse generator. An external logic circuit generates a voltage pulse train, which ensures that the LNA bias is disabled prior to and during the UWB impulse emission. It is worth to mention that the proposed logic circuit doubles the clock, this will be discussed in detail in Sec. 6.1. A frequency divider with a division ratio of 2 is used to make sure that the logic circuit output has the same frequency as the transmit clock signal. The low amplitude of the UWB impulses has no risk of damage to the disabled LNA. After the impulses have been transmitted, the LNA bias is immediately recovered. So the reflected signal can be well detected. The recovering time of the LNA directly decides the minimum operating distance of the radar, it should be designed as small as possible. The external logic circuit impulse generator/LNA

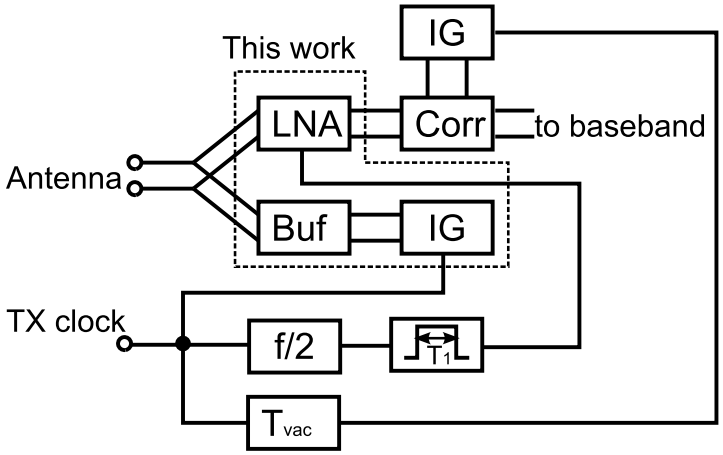

Fig. 6.1: Block diagram of the proposed monostatic UWB radar. The merged impulse generator/LNA module is introduced to avoid the need of a complex UWB transmit/receive switch.

module will be discussed in detail in the following sections.

6.1 The Logic Circuit

The external logic circuit is presented in this subsection. The circuit block diagram is illustrated in Fig. 6.2. It consists of two inverters and one XOR gate. All these three elements are commercially available. The clock signal is split into two branches, one is fed to the inverters and the other one is connected to one input port of the XOR gate. The two inverters make that V_1 is delayed by T_{delay} with respect to V_2. The width of the output voltage pulse from the XOR gate is determined by the value of T_{delay}.

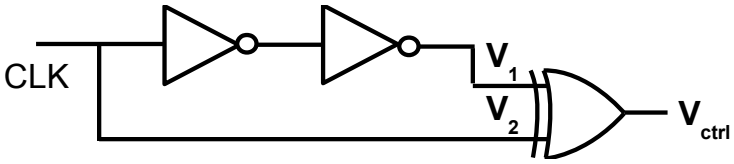

Fig. 6.2: The block diagram of the external logic circuit. The inverters and the XOR gate are commercially available.

For further explanation, the timing diagram of this circuit is plotted in Fig. 6.3. For simplicity, the input clock signal is in the form of a square wave with a duty cycle of 50 percent and a period of T_{CLK}. As can be seen, a delay with a value of T_{delay} between V_1 and V_2 is introduced by the two converters. This time-domain misalignment correspondingly introduces a voltage pulse train at the output of the XOR gate. The width of the voltage pulse T_1 can be calculated as

$$T_1 = T_{ctrl} - T_{delay} \tag{6.1}$$

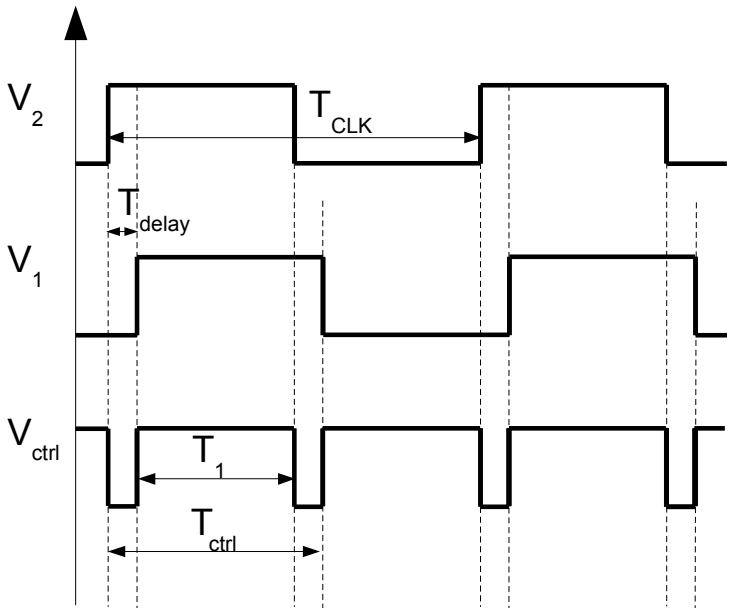

Fig. 6.3: The timing diagram of the logic circuit.

where T_{ctrl} is the period of the output pulse train and can be expressed as

$$T_{ctrl} = \frac{T_{CLK}}{2} \tag{6.2}$$

So a voltage pulse train with a pulse width of T_1 is generated by this logic circuit. The repetition rate of this pulse train is twice the input clock frequency. As shown in Fig. 6.2, a frequency divider with a division ratio of 2 is placed in front of the logic circuit to ensure that the V_{ctrl} has the same frequency as the transmitter clock signal.

Fig. 6.4 shows the measured result of the output voltage waveform with feeding a 40 MHz sinusoidal signal. The voltage amplitude is around 3 V, which is required

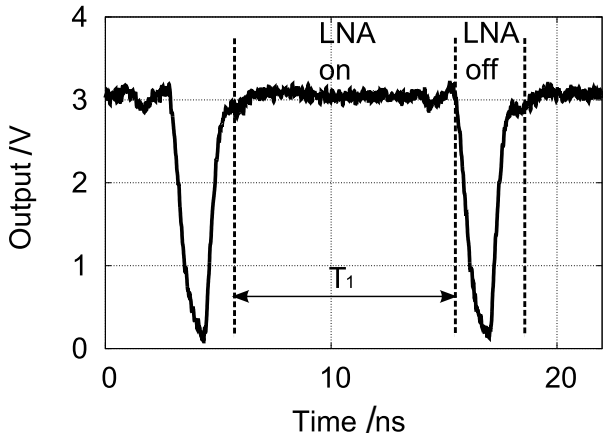

Fig. 6.4: Measured result of the output voltage pulse from the logic circuit. It is employed to briefly switch off the LNA

by the bandgap reference. When controlled by this signal, the LNA bias is briefly switched off to allow the emission of the UWB impulses, as illustrated in Fig. 6.4.

6.2 The Differential LNA with Sleep Mode

The schematic of the differential LNA core together with a bandgap reference circuit can be seen in Fig. 6.5. The bandgap reference is implemented to provide a stable supply voltage (V_{ref}), which supplies the LNA core through current mirrors. The control signal (V_{ctrl}) for the bandgap reference is generated by the external logic circuit described in Sec. 6.1 and introduces the sleep mode operation to the LNA.

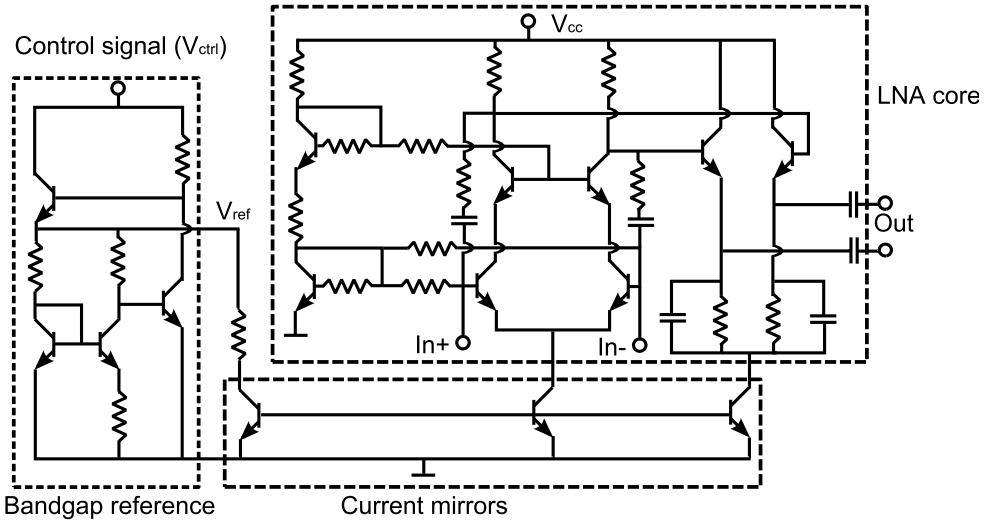

Fig. 6.5: Complete schematic of the UWB LNA with sleep mode. Detailed circuit parameters can be found in Appendix A.8.

When V_{ctrl} = 0, V_{ref} equals 0 and the LNA is switched off. When V_{ctrl} = 3 V, V_{ref} becomes around 1.1 V and the LNA is turned on. Fig. 6.6 (a) shows the simulated dependence of V_{ref} on the control voltage V_{ctrl} at room temperature. It can be seen that V_{ref} varies only slightly when V_{ctrl} changes from 2.5 to 5 V. This property largely decreases the amplitude requirement of the control signal V_{ctrl}. Furthermore, the bandgap reference ensures that V_{ref} is almost independent on the ambient temperature. The simulated result of V_{ref} versus temperature is given in Fig. 6.6 (b). The simulated temperature is swept from -40 to 60 Celsius. This simulation considers temperature dependence of the transistors and the passive components. As illustrated in Fig. 6.6 (b), the output voltage V_{ref} depends weakly on temperature, it changes only around 10 percent over the complete simulated temperature range from -40 to 60 °C.

As previously discussed, the LNA bias is disabled during the impulse emission. So, the isolation of the disabled LNA is another important parameter, it should be high enough to prevent the leakage from influencing the following correlator. Simulation shows that the disabled LNA has an isolation larger than 40 dB in the complete UWB

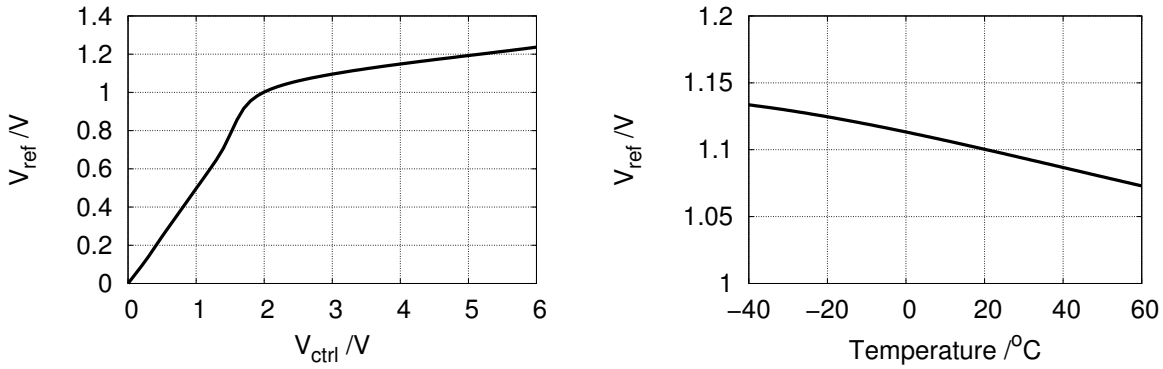

(a) (b)

Fig. 6.6: Simulated results of the bandgap reference output voltage as functions of (a) V_{ctrl} and (b) temperature.

frequency range. Another important issue is the minimum operating distance. To make this distance as short as possible, the LNA should quickly wake up after the bias is recovered. In this design, the base voltage potentials of the transistors in the cascode stages are always kept at a suitable level, this is extremely helpful for a fast recovery. Simulated results show that the LNA returns to full gain within 1 ns. Correspondingly, the minimum working distance of this proposed monostatic radar is around 15 cm.

It is worth to mention that the buffer following the impulse generator presents an impedance $Z_{TX,off}$ to the LNA. This added parasitic is included during the design of the LNA. Simulations indicate that the LNA noise figure and gain are sensitive to the $Z_{TX,off}$. However, with suitable selection of the transistor size and bias, acceptable performance can be achieved. Fig. 6.7 shows the photo of the fabricated impulse generator/LNA module. It has an overall area of 0.50 mm^2 including bond pads.

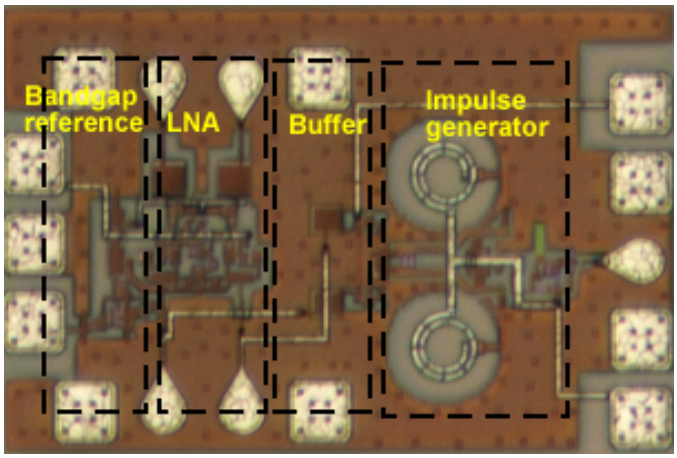

Fig. 6.7: Chip photo of the realized monostatic radar frontend.

To characterize the performance of the LNA, the input port of the bandgap reference is biased with a 3 V DC voltage supply. Two passive UWB baluns are used for the S-parameter measurement. Fig. 6.8 shows the measured matching performance of the realized circuit. As can be seen, the measured return loss is better than 6 dB at

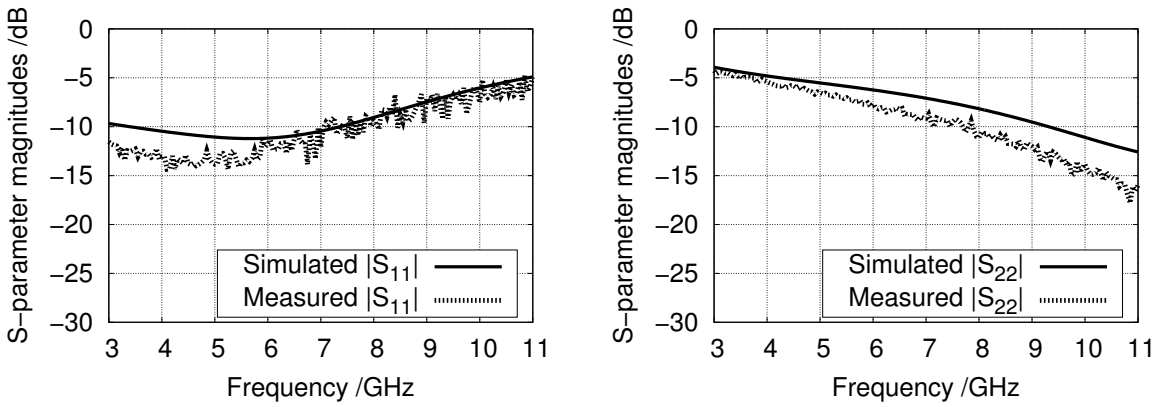

Fig. 6.8: Comparison of the measured and simulated (a) input matching and (b) output matching of the differential LNA with sleep mode.

the input, and better than 5 dB at the output in the complete UWB range from 3.1 to 10.6 GHz. The LNA shows a measured maximum gain of 18 dB with a 2.2 dB variation in the complete FCC allocated range, as shown in Fig. 6.9 (a). The extracted

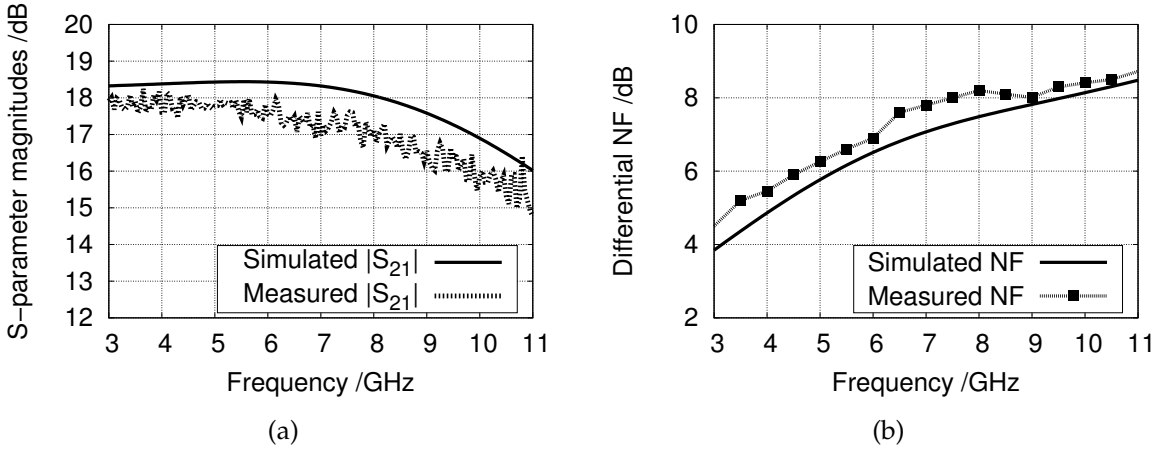

Fig. 6.9: The results of (a) gain and (b) noise figure of the differential LNA, with applying a constant 3 V voltage supply as the input of the bandgap reference.

differential noise figure based on single-end measurements can be seen in Fig. 6.9 (b). The extraction method has been discussed in Sec. 4.2.2. The result varies from 4.5 to 8.7 dB in the FCC allocated frequency range, it shows a worse performance compared to the result depicted Fig. 4.9 (a). This is mainly due to the influence of the buffer stage in the transmitting path.

6.3 The Impulse Generator and the Buffer Stage

The complete schematic of the impulse generator together with a buffer stage is plotted in Fig. 6.10. The implementation of the impulse generator circuit is similar to the approach discussed in Sec. 3.3. 2. The two emitter follower buffers are placed

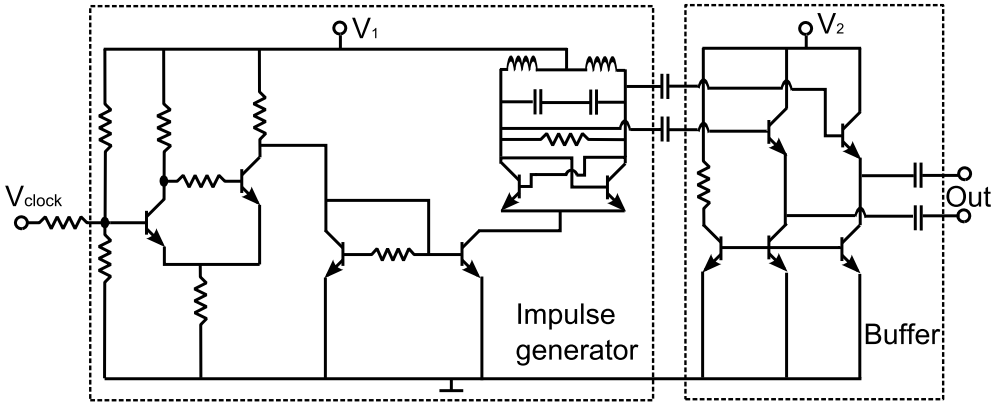

Fig. 6.10: The circuit schematic of the impulse generator and the buffer stage. The buffer stage is inserted to reduce the influence on the differential LNA in the receiving path.

to avoid the strong influence of the LC oscillator on the LNA. The buffers are totally symmetrical by placing identical transistors in the two branches. Simulation shows that the pulse generator copes well with the impedance from the disabled LNA.

Fig. 6.11 (a) shows the measured output time domain waveform with the LNA disabled. In this experiment, the impulse generator circuit was fed by an 80 MHz sinu-

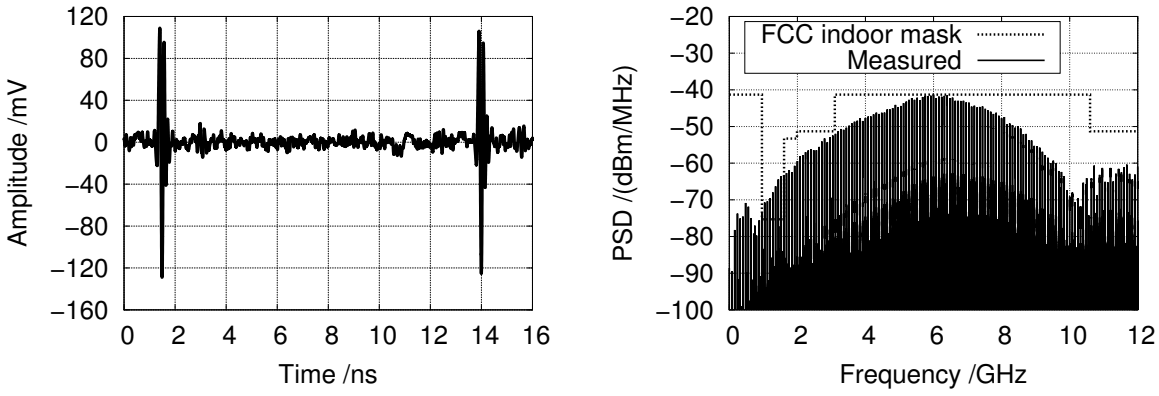

Fig. 6.11: Measurement results of the generated 80 MHz UWB impulse train in (a) time and (b) frequency domain.

soidal signal. The total power consumption at this situation is 15 mW from a 1.5 V

supply voltage. As can be seen in Fig. 6.11 (a), the measured UWB impulses have a peak-peak amplitude of 220 mV and a FWHM of the envelope of 0.4 ns. The spectrum of the measured impulse train is illustrated in Fig. 6.11 (b). It shows a 10 dB bandwidth of 5.1 GHz from 3.3-8.4 GHz with the centre frequency located at 6 GHz. The result indicates that the measured output spectrum complies well with the FCC mask for indoor UWB systems.

6.4 System Measurement

The merged impulse generator/LNA IC as shown in Fig. 6.7 was characterized in time domain. The experimental set-up can be seen in Fig. 6.12 (a). The antenna ter-

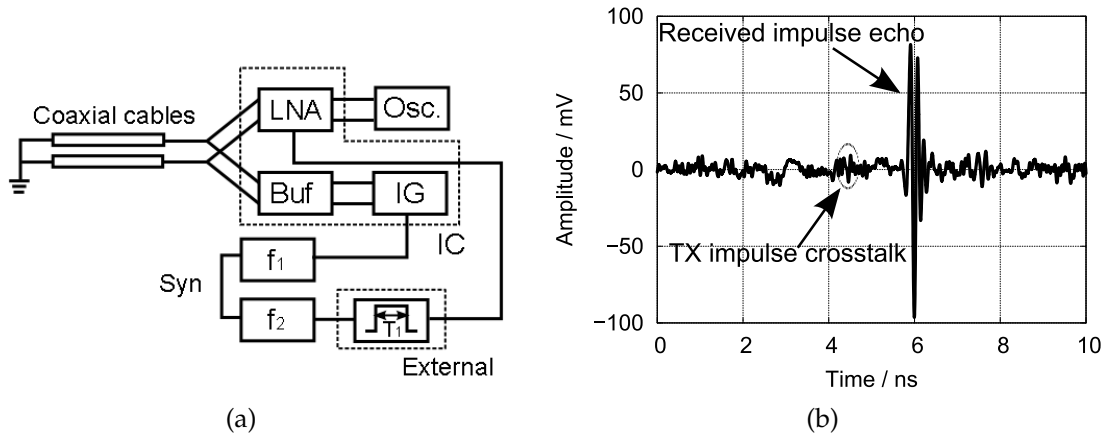

Fig. 6.12: (a) Measurement set-up and (b) the recorded waveform at the output of the LNA.

minals were connected to two short coaxial cables, and each of them fed into a 10 dB attenuator shorted at the far end. An approximately 1 ns delay was generated by the coaxial cables and the attenuators, this corresponds to a distance of 15 cm in air. Two synchronized signal sources were used to supply the clock signals for the impulse generator and the external logic circuit. The phase difference was manually adjusted to ensure that the LNA bias is disabled during the impulse generation. A real time oscilloscope with a 13 GHz bandwidth recorded the measured time-domain waveforms at the output of the LNA. Fig. 6.12 (b) depicts the recorded signal waveform. The received impulse echo can be clearly detected. Due to a high isolation of the disabled LNA, the crosstalk from the transmitted impulse is barely visible and will not influence the further processing. The significant common-mode transients due to the bias switching are completely invisible because of the completely balanced setup. It is worth to mention that this concept only works for differential configuration since it suppresses the common mode transient upon bias switching. This experiment proves that the realized frontend IC can be well used for monostatic radar applications.

Chapter 7

Conclusion

In this thesis, a differential chipset using an inexpensive Si/SiGe HBT technology for IR-UWB applications has been realized. The key components including UWB impulse generators, LNA, correlator and energy detection circuit were designed and characterized. The presented IR-UWB systems can be used for precise radar and high-speed communications.

A quenched-oscillation approach is adopted for highly stable impulse generation. The realized impulse generator utilizes a Schmitt trigger for clock shaping, which incorporates with a current spike circuit to shortly switch on a cross-coupled LC oscillator. The generated impulses with an envelope width of 0.3 ns FWHM have a spectrum well fitting the FCC regulatory mask. The output impulse repetition rate equals the input clock frequency and reaches the GHz range. This impulse generator can be used for OOK and PPM schemes. Through slight modifications, the impulse generator has been successfully extended to include tunability to different spectral allocations in the USA, Europe and Japan as well as a BPM function.

Both a correlation type receiver and an energy detection receiver have been implemented. Key component for both receiver types is a fully differential LNA. The realized LNA with negative feedback shows a maximum gain of 19.9 dB with a variation of 1.8 dB and a worst-case noise figure of 2.9 dB over the 3.1-10.6 GHz range. This completely inductor-less design features 15 ps group delay variation across the FCC UWB range and an extremely small chip size of 0.14 mm^2.

The presented monolithic correlation receiver combines a UWB LNA, a four-quadrant true multiplier, a template impulse generator, low pass filters and a differential buffer on a single chip. The receiver IC occupies a small area of 0.50 mm^2 and consumes a total DC power of 130 mW with the template impulse generator operating with 200 MHz clock signal. The receiver IC shows an excellent correlation detection performance and a minimum discernible signal level of -90.6 dBm with a 100 KHz IF bandwidth.

The fully integrated energy detection IC is realized, with a DC power consumption of 108 mW and a small chip area of 0.26 mm^2. A squaring circuit based on a Gilbert-cell

is used to collect the energy of the received impulses. Based on the energy detection receiver, short-distance data transmission with a speed of 700 Mbit/s using OOK modulation scheme has been demonstrated.

A bistatic radar utilizing the impulse generator IC and the correlation type receiver IC is realized. Two dielectric rod antennas fed by a planar structure are employed. Compact design has been achieved through placing the ICs on the antenna substrates. The realized radar system has been proved to have a motion tracking capability in mm range. In terms of medial applications, measurements such as breathing pattern detection, target surface estimation and sub-surface 3-D localization have been performed.

To further reduce the size of the radar system, a monostatic radar concept is proposed. A rapid turn-around impulse generator/LNA module IC has been successfully demonstrated. The module IC is the first reported monostatic radar frontend circuit at the time of writing. The implementation of complete monostatic radar system can be an interesting task for future work.

In conclusion, the realized differential IR-UWB chipset is promising for precise radar sensing and high-speed transmissions. In the future, correlation type receivers with self clock recovery might be developed in order to increase the transmission distance in data communication applications.

Bibliography

[1] H.F. Harmuth, *Transmission of Information by Orthogonal Functions*, First Edition, Springer, NewYork, 1969.

[2] J. D. Taylor, *Introduction to Ultra Wideband Radar Systems*, Boca Raton, FL: CRC, 1995.

[3] Federal Communications Commission, "Revision of Part 15 of the Commission's Rule Regarding Ultra-wideband Transmission Systems", *Report and Order in ET Docket No. 98-153*, adopted 14 Feb. 2002, released 15 July 2002.

[4] M. Z. Win and R. A. Scholtz, "On the robustness of ultra-wide bandwidth signals in dense multipath environments", *IEEE Commun. Lett.*, vol. 2, No. 2, pp. 51 - 53, 1998.

[5] T.W. Hertel, "Cable-current effects of miniature UWB antennas", *IEEE Int. Antenna and Prop. Symp.*, Vol. 3A, pp. 524-527, 2005

[6] A. Schüppen, J. Berntgen, P. Maier, M. Tortschanoff, W. Kraus and M. Averweg, "An 80 GHz SiGe production technology", *III-V Review*, vol. 14, pp. 42-46, August 2001.

[7] ECC within the European Conference of Postal and Telecommunications Administrations (CEPT), "Commission Decision of 21 February 2007: On allowing the use of the radio spectrum for equipment using UWB technology in a harmonized manner in the community," EC, Official Journal of the European Union L 55/33 Std., Feb. 2007.

[8] AWF3/14, "Technical Conditions on UWB Radio Systems in Japan", MIC, Japan, 2006.

[9] A. Batra et al., "Multi-band OFDM Physical Layer Proposal", IEEE 802.15-03/268r5, Nov. 2006.

[10] ECMA International, "Standard ECMA-368: High Rate Ultra Wideband PHY and MAC Standard", WiMedia Alliance, Standard, December 2008.

[11] B. Razavi, T. Aytur, C. Lam, F. Yang, K. Li, R. Yan, H. Kang, C. Hsu and C. Lee, "A UWB CMOS Transceiver"; *IEEE J. Solid-State Circuits*, vol. 40, No. 12, pp. 2555 - 2562, Dec. 2005

[12] T. Aytur, H. Kang, R. Mahadevappa, M. Altintas, S. ten Brink, T. Diep, C. Hsu, F. Shi, F. Yang, C. Lee, R. Yan and B. Razavi, "A Fully Integrated UWB PHY in 0.13 μm CMOS"; *IEEE Int. Solid-State Circuits Conf. Dig. Tech. Papers,* San Francisco, CA, 11-15 Feb. 2006, pp. 418 - 419.

[13] R. J. Fontana, "Recent system applications of short-pulse ultra-wideband (UWB) technology," *IEEE Trans. Microw. Theory Tech.*, vol. 52, no. 9, pp. 2087-2104, Sep. 2004.

[14] Y. Wang, A. M. Niknejad, V. Gaudet and K. Iniewski, "A CMOS IR-UWB transceiver design for contact-less chip testing applications", *IEEE Trans. Circuits Syst. II, Express Briefs*, vol. 55, pp. 334-338, Apr. 2008.

[15] R. Gharpurey and P. Kinget Eds., *Ultra-wideband Circuits, Transceivers and Systems*, Springer, 2008.

[16] A. Khaleghi, R. Santiago and I. Balasingham, "Ultra-wideband pulse-based data communications for medical implants", *IET Communications*, Vol. 4, no. 15, pp. 1889-1897, Oct. 2010.

[17] J. Xia, C. Law, Y. Zhou and K. Koh, "3-5 GHz UWB Impulse Radio Transmitter and Receiver MMIC Optimized for Long Range Precision Wireless Sensor Networks", *IEEE Trans. Microw. Theory Tech.*, Vol. 58, no. 12, pp. 4040-4051, Dec. 2010.

[18] Z. Zou, D. Mendoza, P. Wang, Q. Zhou, J. Mao, F. Jonsson, H. Tenhunen and L. Zheng, "A Low-Power and Flexible Energy Detection IR-UWB Receiver for RFID and Wireless Sensor Networks", *IEEE Trans. Circuits Syst. I, Reg. Papers*, Vol. 58, NO. 7, pp. 1470-1482, Jul. 2011.

[19] S. Solda, M. Caruso, A. Bevilacqua, A. Gerosa, D. Vogrig and A. Neviani, "A 5 Mb/s UWB-IR Transceiver Front-End for Wireless Sensor Networks in 0.13 m CMOS", *IEEE J. Solid-State Circuits*, Vol. 46, no. 7, pp. 1636-1647, Jul. 2011.

[20] Y. Zhou, C. Law and J. Xia, "Ultra Low-Power RFID Tag with Precision Localization using IR-UWB", *Proc. IEEE MTT-S Int. Microw. Symp.*, Baltimore, MD, 5-10 June 2011, pp. 1-4.

[21] C. Zhang, M. Kuhn, B. Merkl, A. Fathy and M. Mahfouz, "Real-Time Noncoherent UWB Positioning Radar With Millimeter Range Accuracy: Theory and Experiment", *IEEE Trans. Microw. Theory Tech.*, Vol. 58, no. 1, pp. 9-20, Jan. 2010.

[22] G. Fischer, O. Klymenko and D. Martynenko,"Time-of-Arrival measurement extension to a non-coherent impulse radio UWB transceiver", *Proc. 5th Workshop on Positioning, Navigation and Communication*, 22-27 Mar. 2008, pp. 265-270.

[23] H. Luecken, C. Steiner and A. Wittneben, "ML timing estimation for generalized UWB-IR energy detection receivers", *IEEE Int. Conf. on UWB*, 9-11 Sep. 2009, pp. 829-833.

[24] J. Xu, M. Ma and C. Law, "Position Estimation Using UWB TDOA Measurements", *IEEE Int. Conf. on UWB*, 24-27 Sep. 2006, pp. 605-610.

[25] J. Li and T. Talty, "Channel characterization for ultra-wideband intra-vehicle sensor networks", *Proc. Military Commun. Conf.*, 2006, pp. 1-5.

[26] V. Mehta and M. Zarki, "An Ultra Wide Band (UWB) based sensor network for civil infrastructure health monitoring", *Proc. 1st Eur. Workshop Wireless Sensor Netw.*, Berlin, Germany, Jan. 19-24, 2004.

[27] B. Schleicher, "Impulse-Radio Ultra-Wideband Systems for Vital-Sign Monitoring and Short-Range Communications"; Ph.D. thesis, Inst. of Electron Devices and Circuits, University of Ulm, Ulm, Germany, 2011.

[28] M. Guardiola, L. Jofre and J. Romeu, "3D UWB tomography for medical imaging applications", *Proc. IEEE Antennas and Propagation Society Int. Symp.*, 11-17 July 2010, pp. 1-4.

[29] J. Dederer, B. Schleicher, F. De Andrade Tabarani Santos, A. Trasser and H. Schumacher, "FCC compliant 3.1-10.6 GHz UWB Pulse Radar using Correlation Detection", *Proc. IEEE MTT-S Int. Microw. Symp.*, Honolulu, HI, 3-8 June 2007, pp. 1471-1474.

[30] X. Wang, S. Fan, H. Tang, L. Lin, J. Liu, Q. Fang, H. Zhao, A. Wang, L. Yang and B. Zhao, "A Whole-Chip ESD-Protected 0.14-pJ/p-mV 3.1-10.6 GHz Impulse-Radio UWB Transmitter in 0.18μm CMOS"; *IEEE Trans. Microw. Theory Tech.*, Vol. 59, no. 4, pp.1109 - 1116, Apr. 2011.

[31] M. Demirkan and R. Spencer, "A 1.8G pulses/s UWB Transmitter in 90nm CMOS"; *IEEE Int. Solid-State Circuits Conf. Dig. Tech. Papers,* San Francisco, CA, 3-7 Feb. 2008, pp. 116 - 117.

[32] M. Crepaldi, L. Chen, K. Dronson, J. Fernandes and P. Kinget, "An Ultra-Low-Power Interference-Robust IR-UWB Transceiver Chipset Using Self-Synchronizing OOK Modulation"; *IEEE Int. Solid-State Circuits Conf. Dig. Tech. Papers,* San Francisco, CA, 7-11 Feb. 2010, pp. 226 - 227.

[33] S. Diao, Y. Zheng and C. Heng, "A CMOS Ultra Low Power and High Efficiency UWB-IR Transmitter for WPAN Applications", *IEEE Trans. Circuits Syst. II, EXP. Briefs*, vol. 56, Issue 3, pp. 200-204, 2009.

[34] D. Barras, F. Ellinger, H. Jaekel and W. Hirt, "Low-Power Ultra-Wideband Wavelets Generator With Fast Start-Up Circuit"; *IEEE Trans. Microw. Theory Tech.*, Vol. 54, no. 5, pp.2138 - 2145, May 2006.

[35] Y. Zheng, K. Wong, M. Asaru, S. Dan, W. Zhao, Y. The, P. Andrew, F. Lin, W. Yeoh and R. Singh, "A 0.18μm CMOS Dual-Band UWB Transceiver"; *IEEE Int. Solid-State Circuits Conf. Dig. Tech. Papers,* San Francisco, CA, 11-15 Feb. 2007, pp. 114 - 115.

[36] J. Vignarelli and C. Dehollain, "A Discrete-Components Impulse-Radio Ultrawide-Band (IR-UWB) Transmitter"; *IEEE Trans. Microw. Theory Tech.*, Vol. 59, no. 4, pp.1141 - 1146, Apr. 2011.

[37] Y. Zhu, J. Zuegel, J. Marciante and H. Wu, "Distributed Waveform Generator: A New Circuit Technique for Ultra-Wideband Pulse Generation, Shaping and Modulation", *IEEE J. Solid-State Circuits*, Vol. 44, no. 3, pp. 808-823, Mar. 2009.

[38] H. Sheng, P. Orlik, A. Haimovich, L. Cimini and J. Zhang, "On the spectral and power requirements for ultra-wideband transmission", *IEEE Int. Conf. on Communications*, Anchorage, AL, Vol. 1, pp. 738 - 742, Mar. 2003.

[39] D. Lin, A. Trasser and H. Schumacher, "Si/SiGe HBT differential impulse generator for high-speed UWB applications", *Electronic Letters*, Vol.46, Issue. 26, pp. 1634-1635, 2010.

[40] D. Lin, B. Schleicher, A. Trasser and H. Schumacher, "Si/SiGe HBT UWB impulse generator tunable to FCC, ECC and Japanese spectral masks", *IEEE Radio and Wireless Symp.*, Phoenix, AZ, 16-19 Jan. 2011, pp. 66-69.

[41] D. Lin, A. Trasser and H. Schumacher, "A Low-Power SiGe Impulse Radio-UWB Transmitter with Biphase Modulation Function", *Proc. IEEE MTT-S Int. Microw. Symp.*, Montreal, Canada, 17-22 Jun. 2012, pp. 1-3.

[42] F. Nekoogar, "Ultra-Wideband Communications-Fundamentals and Applications", Upper Saddle River, NJ: Prentice Hall, 2005

[43] M.L. Welborn, "System Consideration for UltraWideband Wireless Networks", *IEEE Int. Radio Wireless Conf.*, pp. 5-8, 2001.

[44] J. van der Tang, D. Kasperkovitz and A. van Roermund, "High-Frequency Oscillator Design for Integrated Transceivers", *Boston, MA: Kluwer Academic Publisher*, 2003, pp. 31-33.

[45] J. A. Sanders, F. Verhulst and J. Murdock, "Averaging Methods in Nonlinear Dynamical Systems", *Applied Mathematical Sciences*, vol. 59, 2nd ed., Springer, 2007, pp. 21-43.

[46] M. Ghavami, L. B. Michael and R. Kohno, "Ultra Wideband Signals and Systems in Communication Engineering", *John Wiley and Sons, Ltd* 2nd ed., 2007, pp. 25-40.

[47] N. Deparis, A. Siligarisy, P. Vincent and N. Rolland, "A 2 pJ/bit pulsed ILO UWB transmitter at 60 GHz in 65-nm CMOS-SOI", *IEEE Int. Ultra-Wideband Conf.*, 9-11 Sep. 2009, pp. 113-117.

[48] M. Leib, M. Frei and W. Menzel, "A novel ultra-wideband circular slot antenna excited with a dipole element", *IEEE Int. Ultra-Wideband Conf.*, 9-11 Sept. 2009, pp. 386 - 390.

[49] H. Hautmann, A. Schneider, T. Pinkau, F. Peltz and H. Feussner, "Electromagnetic Ca-theter Navigation During Bronchoscopy", *Chest*, 2005, pp. 382 - 387.

[50] D.R. Elgort, E. Wong, C. Hillenbrand, F. Wacker, J. Lewin and J. Duerk, "Real-Time Catheter Tracking and Adaptive Imaging", *J. of Magnetic Resonance Imaging.*, vol. 18, 2003, pp. 621-626.

[51] H. Rapp, A. Folge and T. Grau, "Ultrasound-Guided Epidural Catheter Insertion in Children", *Anesth Analg.*, vol. 101, 2005, pp. 333-339.

[52] C. Lu, A. Pham and M. Shaw, "A CMOS Power Amplifier for Full-Band UWB Transmitters", *IEEE RFIC Symp.,* 11-13 June, 2006, pp. 397-400.

[53] S. A. Z. Murad, R. Pokharel, A.I.A. Galal, R. Sapawi, H. Kanaya and K. Yoshida, "An Excellent Gain Flatness 3.0-7.0 GHz CMOS PA for UWB Applications", *IEEE Microw. Wireless Compon. Lett.,* vol. 20, no. 9, pp. 510-512, Sep. 2010.

[54] H. Schumacher, *Monolithic Microwave ICs in High Speed Communication Systems*, Lecture Script, University of Ulm, 2008.

[55] J. Dederer, "Si/SiGe HBT ICs for Impulse Ultra-Wideband Communications and Sensing"; Ph.D. thesis, Inst. of Electron Devices and Circuits, University of Ulm, Ulm, Germany, 2009.

[56] M. Mirbach, "Lokalisierng ultrabreitbandiger Transmitter in hochpermittiven Medien"; Ph.D. thesis, Inst. of Microwave Technique, University of Ulm, Ulm, Germany, 2014.

[57] S. Gabriel, R. Lau and C. Gabriel, "The Dielectric Properties of Biological Tissues: II. Measurements in the Frequency Range 10 Hz to 20 GHz," *Phys. Med. Biol.*, 41:2251, 1996.

[58] Schmid and Partner Engineering AG (Speag), Zuerich, "Maintenance of tissue simulating liquids," 2007.

[59] M. Leib, M. Frei, D. Sailer and W. Menzel, "Design and characterization of a UWB slot antenna optimized for radiation in human tissue"; *IEEE Int. Ultra-Wideband Conf.*, 9-11 Sep. 2009, pp. 159-163.

[60] J. Ryckaert, J. Ryckaert, M. Badaroglu, V. Heyn, G. Van der Plas, P. Nuzzo, A. Baschirotto, S. Amico, C. Desset, H. Suys, M. Libois, B. Van Poucke, P. Wambacq and B. Gyselinckx, "A 16 mA UWB 3 to 5 GHz 20 Mpulses/s Quadrature Analog Correlation Receiver in 0.18 μ CMOS", *IEEE Int. Solid-State Circuits Conf. Dig. Tech. Papers,* San Francisco, CA, 6-9 Feb. 2006, pp. 368 - 369.

[61] G. Durisi and S. Benedetto, "Performance of coherent and noncoherent receivers for UWB communications", *IEEE Int. Conf. on Communications,* 20-24 June 2004, pp. 3429 - 3433.

[62] J. H. Reed, Ed., *An Introduction to Ultra Wideband Communication Systems*, Prentice Hall International, 2005.

[63] S. Tiuraniemi, L. Stoica, A. Rabbachin and I. Oppermann, "Front-End Receiver for Low Power, Low Complexity Non-Coherent UWB Communications System", *IEEE Int. Ultra-Wideband Conf.*, 5-8 Sept. 2005, pp. 339 - 343.

[64] A. Rabbachin, T. Quek, P. Pinto, I. Oppermann and M.Z. Win, "Non-Coherent UWB Communication in the Presence of Multiple Narrowband Interferers"; *IEEE Trans. Wireless Communications*, Vol. 9, no. 11, pp.3365 - 3379, Nov. 2010.

[65] M. J. Kuhn, M. Mahfouz, C. Zhang, B. Merkl and A. Fathy, "A System-Level Simulation Framework for UWB Localization"; *IEEE Trans. Microw. Theory Tech.*, Vol. 58, no. 12, pp.3527 - 3537, Dec. 2010.

[66] F. Zhang and P.R. Kinget, "Low-power programmable gain CMOS distributed LNA", *IEEE J. Solid-State Circuits*, Vol. 41, no. 6, pp. 1333-1343, June 2006.

[67] Y. Yu, Y. E. Chen and D. Heo, "A 0.6-V Low Power UWB CMOS LNA", *IEEE Microw. Wireless Compon. Lett.*, vol. 17, no. 8, pp. 616-618, Aug. 2007.

[68] M. Tsai, K. Lin and H. Wang, "A 5.4 mW LNA using 0.35 μm SiGe BiCMOS technology for 3.1-10.6 GHz UWB wireless receivers,", *IEEE Radio Freq. Integrated Circuits Symp. Dig.*, pp. 335-338, June 12-14, 2005.

[69] M. Battista, J. Gaubert, M. Egels, S. Bourdel and H. Barthelemy,, "High-voltage-gain CMOS LNA for 6-8.5 GHz UWB receivers"; *IEEE Trans. Microw. Theory Tech.*, vol. 55, no. 8, pp. 713-717, Aug. 2008.

[70] J. Dederer, S. Chartier, T. Feger, U. Spitzberg, A. Trasser and H. Schumacher, "Highly Compact 3.1 - 10.6 GHz UWB LNA in SiGe HBT Technology", *10th European Conf. Wireless Tech.*,pp. 247-250, 8-10 Oct. 2007.

[71] Y. Lin, S. Hsu, J. Jin and C. Chan, "A 3.1-10.6 GHz ultra-wideband CMOS low noise amplifier with current-reused technique", *IEEE Microw. Wireless Compon. Lett.*, vol. 17, no. 3, pp. 232-234, Mar. 2007.

[72] M. Reiha and J. R. Long, "A 1.2 V Reactive-Feedback 3.1-10.6 GHz Low-Noise Amplifier in 0.13 μm CMOS",*IEEE J. Solid-State Circuits*, Vol. 42, no. 5, pp. 1023-1033, May 2007.

[73] S. Prasad, H. Schumacher and A. Gopinath, *High-Speed Electronics and Optoelectronics: Devices and Circuits*, Cambridge University Press, 2009.

[74] H. Schumacher, U. Erben and W. Duerr, "SiGe Heterojunction Bipolar Transistors - The Noise Perspective" *Solid-State Electronics*, Vol. 41 , no. 10, pp. 1485 - 1492, 1997.

[75] L. Belostotski and J.Haslett, “A technique for differential noise figure measurement with a noise figure analyzer,” *IEEE Microwave Magazine*, pp. 158-161, 2009.

[76] J. Huettner, R. Gierlich, A. Ziroff and R. Weigel, “A low cost Ultra-Wide-Band Pulse Radar in a guided wave gauging application ,” *European Radar Conference*, pp. 101-104, Oct. 2009

[77] B. Schleicher, H. Ghaleb, A. Trasser and H. Schumacher, “FM over Impulse Radio UWB", *IEEE Int. Conf. on UWB*, 9-11 Sep. 2009, pp. 200-204.

[78] ELV Elektronik GmbH, *Mobiler Stereo-UKW-Pruefsender (Datasheet)*, 2009.

[79] ELV Elektronik GmbH, *Mini Stereo-RDS-Radio-Modul (Datasheet)*, 2009.

[80] Analog Devices Inc., *AD9959/PCB - Evaluation board for 4-channel 500 MSPS DDS with 10-Bit DACs (Datasheet)*, Oct. 2005.

[81] Meilhaus Electronic GmbH, *MEphisto Scope 1: Command-Interpreter*, Jan. 2010.

[82] M. Leib, A. Vollmer and W. Menzel, “An Ultra-Wideband Dielectric Rod Antenna Fed by a Planar Circular Slot", *IEEE Trans. Microw. Theory Tech.*, vol. 59, no. 4, pp. 1082-1089, Apr. 2011.

[83] D. Zito, D. Pepe, M. Mincica and F. Zito, “A 90nm CMOS SoC UWB Pulse Radar for Respiratory Rate Monitoring”, *IEEE Int. Solid-State Circuits Conf. Dig. Tech. Papers,* San Francisco, CA, 20-21 Feb. 2011, pp. 40 - 41.

[84] A.E.C. Tan, “UWB radar transceiver and measurement for medical imaging”, *IEEE Int. Workshop Biomedical Circuits and Systems*, 1-3 Dec. 2004, pp. 9 - 12.

[85] S. Krishnan, P. Sharma, Z. Guoping and O. Woon, “A UWB based localization system for indoor robot navigation", *IEEE Int. Conf. on UWB*, 24-26 Sept. 2007, pp. 77-82.

[86] A. Chehri, P. Fortier and P. M. Tardif, “UWB-Based Sensor Networks for Localization in Mining Environments", *Ad Hoc Net.*, vol. 7, no. 5, 2009, pp. 987-1000.

[87] M. Mirbach and W. Menzel, “Time of Arrival Based Localization of UWB Transmitters Buried in Lossy Dielectric Media", *IEEE Int. Conf. on UWB*, 17-20 Sep. 2012, pp. 328-232.

[88] M. Mirbach and W. Menzel, “A Simple Surface Estimation Algorithm for UWB Pulse Radars Based on Trilateration", *IEEE Int. Conf. on UWB*, 14-16 Sep. 2011, pp. 273-277.

[89] T. Sakamoto, “A fast algorithm for 3-dimensional imaging with UWB pulse radar systems", *IEICE Trans. on Communication*, vol. E90- B, no. 3, pp. 636-644, 2007.

[90] S. Kidera, T. Sakamoto and T. Sato, “High-resolution 3-d imaging algorithm with an envelope of modified spheres for UWB through-wall radars", *IEEE Trans. on Antennas and Propagation*, vol. 57, no. 11, pp. 3520-3529, 2009.

[91] A. Cacciatori, L. Colalongo and Z.M.K. Vajna, “On the design of ultra wideband FCC compliant integrated radars", *Research in Microelectronics and Electronics*, Sep. 2006, pp. 469-472.

[92] S. Lee, S. Kong, C.-Y. Kim and S. Hong, “A Low-power K-band CMOS UWB Radar Transceiver IC for Short Range Detection", *IEEE Radio Freq. Integrated Circuits Symp. Dig.*, June 2012, pp. 503-506.

[93] X. Wang, A. Dinh, D. Teng, L. Chen, S. Ko, Y. Shi, J. Basran and V. Bello-Hass, “Impulse Based Range-Gated UWB Wireless Transceiver IC in 90 nm CMOS for Medical Sensing Applications and Communications", *IEEE Int. Conf. on UWB*, Sep. 2009, pp. 194-200.

Appendix A

Circuit parameters

A.1 Differential Impulse Generator for the FCC Mask

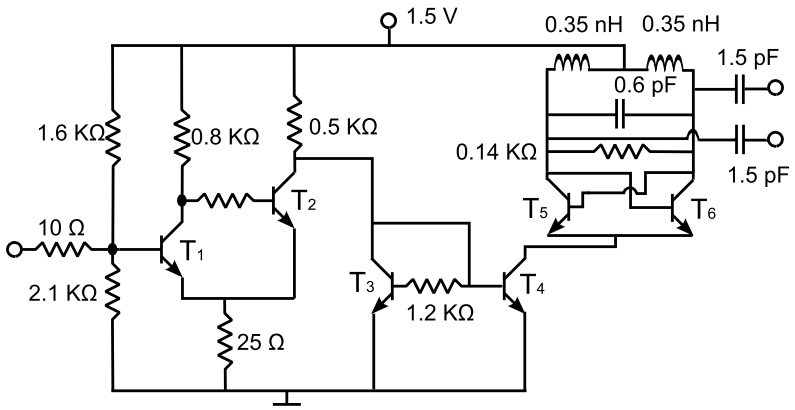

Fig. A.1: Full schematic of the differential impulse generator for the FCC mask. T_1, T_2,: 0.5 x 5 μm^2, T_3: 0.5 x 20 μm^2, T_4: 0.5 x 6 μm^2, T_5: 0.5 x 25 μm^2, T_6: 0.5 x 10 μm^2.

A.2 Differential Tunable Impulse Generator

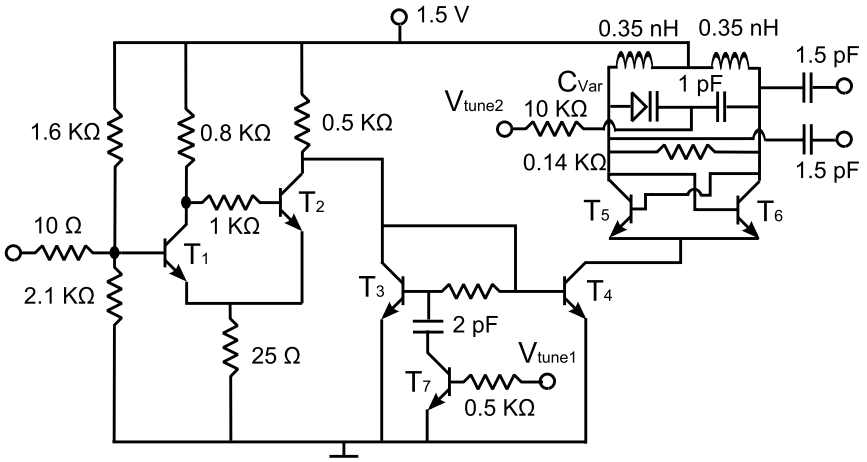

Fig. A.2: Full schematic of the differential tunable impulse generator. T_1, T_2,: 0.5 x 5 μm^2, T_3: 0.5 x 20 μm^2, T_4: 0.5 x 5 μm^2, T_5: 0.5 x 10 μm^2, T_6: 0.5 x 30 μm^2.

A.3 Differential Impulse Generator with BPM Function

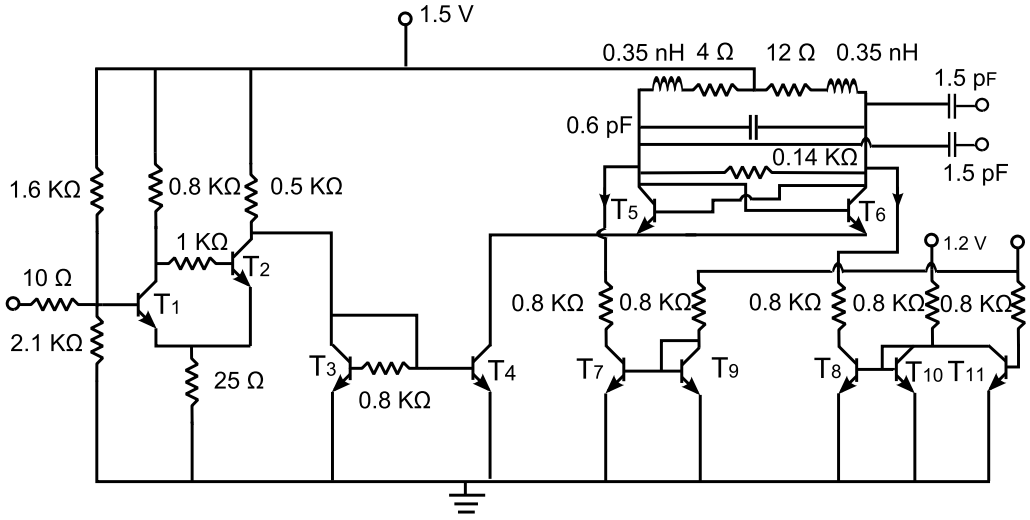

Fig. A.3: Full schematic of the differential impulse generator with BPM function. T_1, T_2,: 0.5 x 5 μm^2, T_3: 0.5 x 20 μm^2, T_4: 0.5 x 7 μm^2, T_5 - T_7, T_8: 0.5 x 15 μm^2, T_9 - T_{11}: 0.5 x 5 μm^2.

A.4 UWB Beacon Transmitter

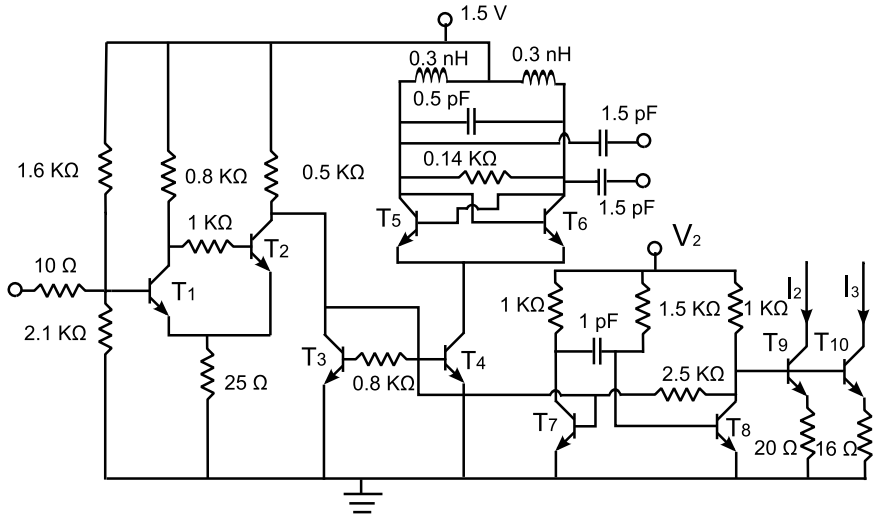

(a)

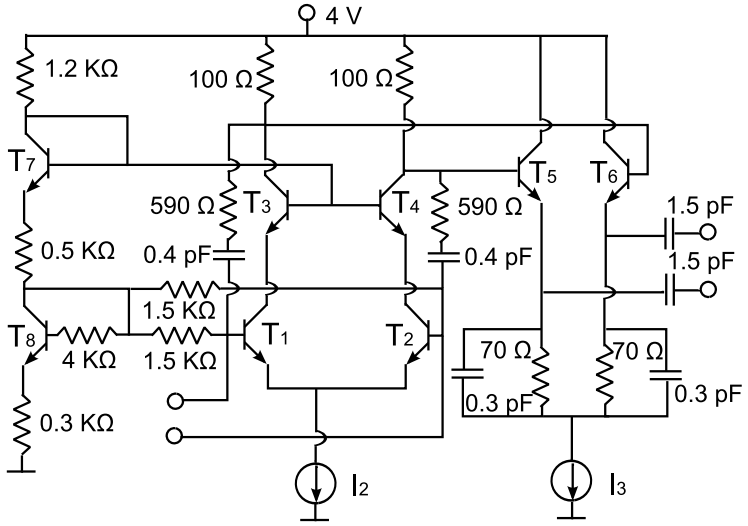

(b)

Fig. A.4: (a) Full schematic of the impulse generation and monoflop circuit. T_1, T_2,: 0.5 x 5 μm^2, T_3: 0.5 x 30 μm^2, T_4: 0.5 x 5 μm^2, T_5,: 0.5 x 10 μm^2, T_6: 0.5 x 20 μm^2, T_7, T_8: 0.5 x 5 μm^2, T_9, T_{10}: 0.5 x 30 x 2 μm^2, non-SIC and (b) the differential UWB power amplifier. T_1 - T_4: 0.5 x 30 μm^2, T_5, T_6: 0.5 x 30 μm^2, T_7, T_8: 0.5 x 5 μm^2..

A.5 Differential LNA

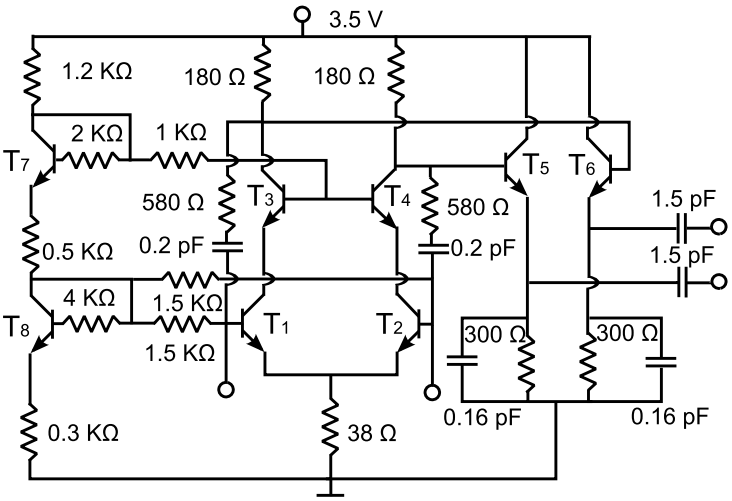

Fig. A.5: Full schematic of the differential UWB LNA. T_1 - T_4: 0.5 x 25 μm^2, T_5, T_6: 0.5 x 6 μm^2, T_7, T_8: 0.5 x 5 μm^2.

A.6 Multiplier-based Correlator

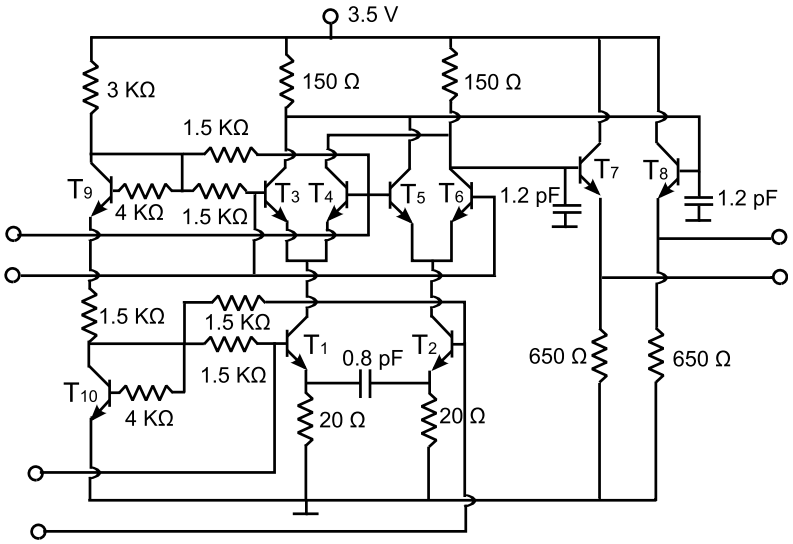

Fig. A.6: Full schematic of the correlator circuit. T_1 - T_8: 0.5 x 10 μm^2, T_9, T_{10}: 0.5 x 5 μm^2.

A.7 Energy Detection Circuit

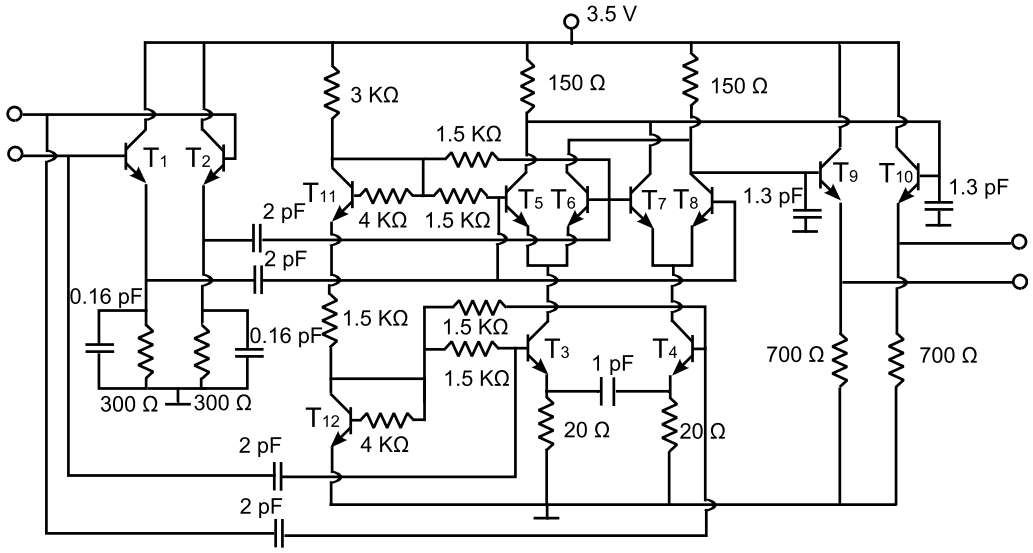

Fig. A.7: Full schematic of the energy detection circuit. T_1, T_2,: 0.5 x 6 μm^2, T_3 - T_{10}: 0.5 x 10 μm^2, T_{11}, T_{12}: 0.5 x 5 μm^2.

A.8 Impulse Generator/LNA Module

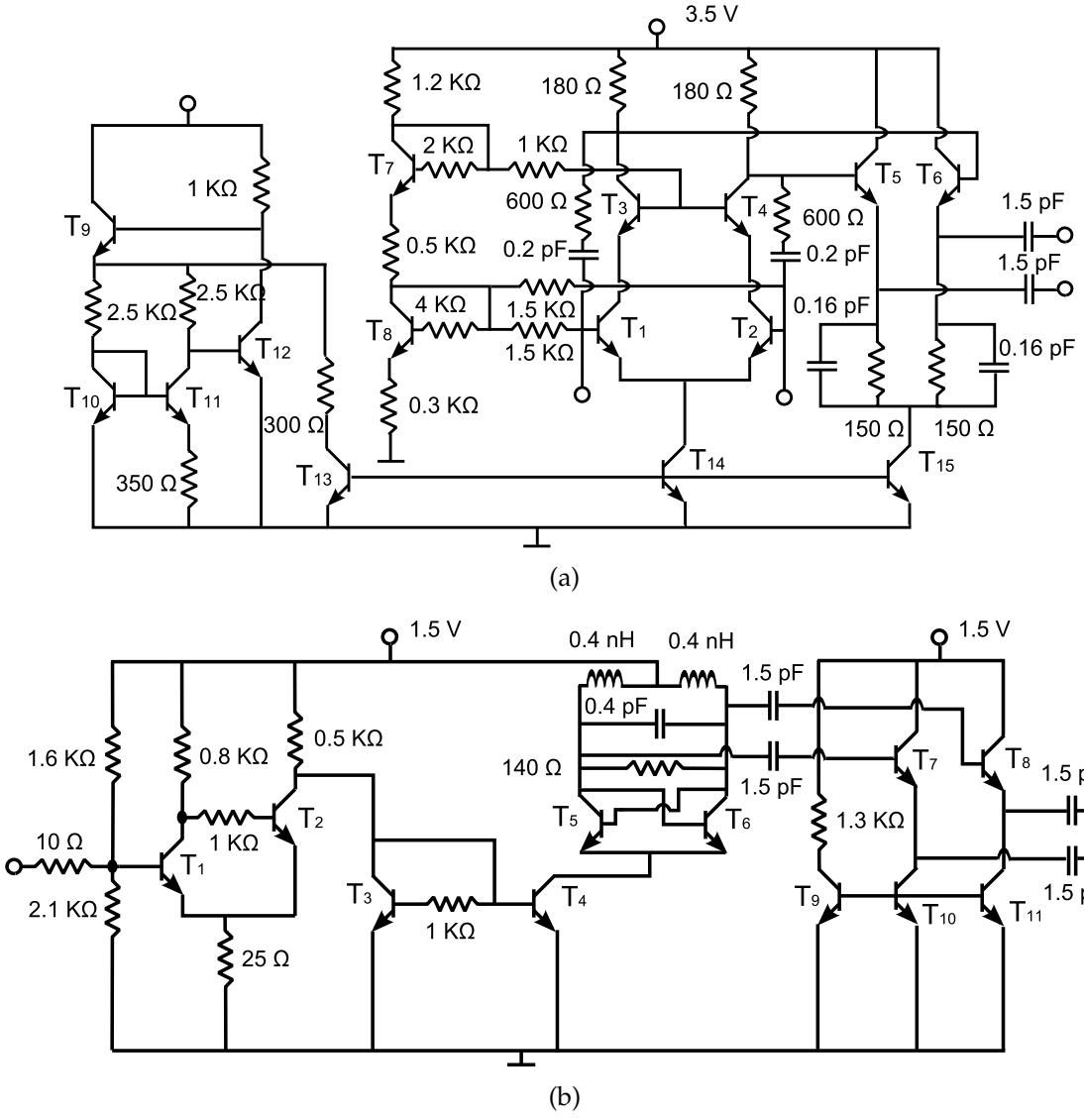

Fig. A.8: (a) Full schematic of the differential LNA with sleep mode. T_1 - T_4: 0.5 x 30 μm^2, T_5, T_6: 0.5 x 6 μm^2, T_7, T_{13}: 0.5 x 5 μm^2, T_{14}: 0.5 x 25 x 2 μm^2 non-SIC, T_{15}: 0.5 x 30 x 2 μm^2 non-SIC, and (b) the impulse generator together with a buffer stage. T_1, T_2,: 0.5 x 5 μm^2, T_3: 0.5 x 20 μm^2, T_4: 0.5 x 6 μm^2, T_5: 0.5 x 20 μm^2, T_6: 0.5 x 10 μm^2. T_7, T_8: 0.5 x 10 μm^2, T_9: 0.5 x 5 μm^2, T_{10}, T_{11}: 0.5 x 15 μm^2

Appendix B

List of Acronyms and Symbols

Acronyms

AWGN	Additive white Gaussian noise
Balun	Single-ended to differential converter
BG	Band group
BPM	Biphase modulation
CCF	Cross-correlation function
DAA	Detect and avoid
DDS	Direct-digital-synthesizer
ECC	Electronic Communications Committee
EIRP	Effective isotropic radiated power
EM	Electromagnetic
FCC	Federal Communications Commission
FM	Frequency modulation
FOM	Figure of merit
FWHM	Full width at half maximum
GPS	Global Positioning System
GSG	Ground-signal-ground
GSM	Global System for Mobile Communications
GSSG	Ground-signal-signal-ground
HBT	Heterojunction bipolar transistor
IF	Intermediate frequency
IR	Impulse-radio

LDC	Low duty cycle
LNA	Low noise amplifier
MB	Multi-band
MDS	Minimum discernible signal
MIC	Ministry of Internal Affairs and Communications
MRI	Magnetic resonance imaging
OFDM	Orthogonal frequency division multiplexing
OOK	On-off keying
PA	Power amplifier
PAM	Pulse amplitude modulation
PPM	Pulse position modulation
PSD	Power spectral density
RFID	Radio-frequency identification
RX	Receiver
RZ-OOK	Return-to-zero on-off-keying
SFDR	Spurious-free dynamic range
TDoA	Time-difference-of-arrival
TFC	Time-frequency code
ToA	Time-of-arrival
TX	Transmitter
UWB	Ultra-wideband
WPAN	Wireless personal area network
WSN	Wireless sensor networks

Symbols

C_{BE}	Base-emitter capacitance
d_{max}	Maximum sensing distance
d_{min}	Minimal motion-tracking resolution
ε_r	Relative permittivity
f_c	Corner frequency
f_{max}	Maximum observation frequency
F_{min}	Minimum noise figure
F_{avg}	Average noise figure
Γ_S	Source reflection coefficient
$\Gamma_{S,opt}$	Noise-optimum source reflection coefficient
g_m	Transconductance
G_{max}	Maximum gain
ω	Angular frequency
P_{diss}	Dissipated power
P_i	Ray length
Q	Quality factor
R_f	Feedback resistance
R_G	Source impedance
r_n	Normalized equivalent noise resistance
R_n	Equivalent noise resistance
σ	Standard deviation of a Gaussian bell shape
τ	Time shift
T_P	Frame period
Z_0	Reference impedance

Appendix C

Publications

• **D. Lin**, B. Schleicher, A. Trasser and H. Schumacher, "A highly compact SiGe HBT differential LNA for 3.1-10.6 GHz ultra-wideband applications", *IEEE Int. Conf. on Ultra-Wideband*, Nanjing, China, 20-23 Sep. 2010, pp. 205-208.

• **D. Lin**, B. Schleicher, A. Trasser and H. Schumacher, "A SiGe HBT Low-Power Pulse Generator for Impulse Radio Ultra-wide Band Applications", *IEEE Int. Conf. on Ultra-Wideband*, Nanjing, China, 20-23 Sep. 2010, pp. 1-4.

• **D. Lin**, A. Trasser and H. Schumacher, "Si/SiGe HBT differential impulse generator for high-speed UWB applications", *Electronic Letters*, Vol.46, Issue. 26, pp. 1634-1635, Nov. 2010.

• **D. Lin**, B. Schleicher, A. Trasser and H. Schumacher, "Si/SiGe HBT UWB impulse generator tunable to FCC, ECC and Japanese spectral masks", *IEEE Radio and Wireless Symp.*, Phoenix, AZ, 16-19 Jan. 2011, pp. 66-69.

• **D. Lin**, A. Trasser and H. Schumacher, "Low Power, Fully Differential SiGe IR-UWB Transmitter and Correlation Receiver ICs", *IEEE Radio Freq. Integrated Circuits Symp. Dig.*, Baltimore, MD, 5-7 Jun. 2011, pp. 101-104.

• **D. Lin**, A. Trasser and H. Schumacher, "A Fully Differential IR-UWB Front-end for Noncoherent Communication and Localization", *IEEE Int. Conf. on Ultra-Wideband*, Bologna, Italy, 14-16 Sep. 2011, pp. 116-120.

• **D. Lin**, A. Trasser and H. Schumacher, "A Low-Power SiGe Impulse Radio-UWB

Transmitter with Biphase Modulation Function", *Proc. IEEE MTT-S Int. Microw. Symp.*, Montreal, Canada, 17-22 Jun. 2012, pp. 1-3.

• T. Thiasiriphet, M. Leib, **D. Lin**, B. Schleicher, J. Lindner, W. Menzel and H. Schumacher, "Investigations on a Comb Filter Approach for IR-UWB Systems", *FREQUENZ*, Vol.63, No. 9-10, Sep. 2009, pp. 179-182.

• U. Schmid, **D. Lin** and W. Menzel, "A Novel Dual Polarization Antenna Array Fed by a Dual Mode Non-Radiative Dielectric Waveguide", *Proc. IEEE MTT-S Int. Microw. Symp.*, Montreal, Canada, 17-22 Jun. 2012, pp. 1-3.

• H. Schumacher, **D. Lin** and A. Trasser, "Frontend ICs for Impulse Radio Sensing and Communications", *IEEE Int. Conf. on Ultra-Wideband*, invited paper, Syracuse, NY, 17-20 Sep. 2012, pp. 21-25.

Curriculum Vitae

Name:	Dayang Lin
Date of Birth:	November 03, 1984
Place of Birth:	Tengzhou, China
Sep. 1991 - Jul. 1996	Preliminary School Shangsi Xiaoxue, Tengzhou, China
Sep. 1996 - Jul. 1999	Middle School Yucai Middle School, Tengzhou, China
Sep. 1999 - Jul. 2002	High School Tengzhou No. 1 High School, Tengzhou, China
Sep. 2002 - Feb. 2006	Bachelor Studies of Electronic Information Engineering Shandong University, Jinan, China Bachelor of Engineer Degree
Mar. 2006 - Apr. 2008	Master Studies of Communication Technology Ulm University, Ulm, Germany Master of Science Degree
May 2008 - Sep. 2013	Research Associate Inst. of Electron Devices and Circuits Ulm University, Ulm, Germany
Oct. 2013 - Present	RF Design Engineer NXP Semiconductors, Hamburg, Germany